POLITECNICO DI TORINO

Master degree in Nanotechnologies for ICTs

Master Thesis

Fighting cancer relapse with remote activation of smart and targeted nanoconstructs

Supervisor:
Prof. Valentina Alice Cauda

Candidate:
Giulia Tamboia

April 2022

Abstract

One of the major concerns that arises after the overt tumor regression in a patient is the cancer recurrence. The work of this Master thesis takes part in the European project XtraUS, aimed at developing targeted, non-immunogenic, stimuli-responsive nanoconstructs in combination with an extracorporeal bloodstream set-up to eliminate circulating tumor cells (CTCs), responsible for cancer relapse and metastasis spreading.

As an initial analysis, the research relies on the effect of the external stimulation on nanoconstructs. For this purpose, an ultrasound stimulation is used together with ZnO nanoparticles, able to enhance the acoustic cavitation phenomenon by introducing a higher amount of gas bubbles in liquids. Thanks to the sinusoidal behavior of the acoustic field, the microbubbles are forced to oscillate, alternating expansion and contraction phases, which may end up in the collapse of gas bubbles. This process is accompanied by a huge release of energy, in terms of temperature and pressure, generating toxic species (Reactive Oxygen Species - ROS), capable to kill CTCs in the blood stream.

Two different techniques are exploited to detect the production and concentration of toxic species; the first one is based on the sonochemiluminescence (SCL) of Luminol solutions, which provides a more qualitative but faster analysis. In fact, Luminol molecules, activated with the presence of an oxidant as hydrogen peroxide (H_2O_2) and hydroxide ions (OH^-), are able to emit blue visible light as they chemically react with ROS, allowing their detection merely via a photocamera, in a dark environment. Differently, the second technique relies on the Electron Paramagnetic Resonance Spectroscopy (EPR), based on the interaction between a magnetic field produced by the EPR equipment and the unpaired electrons associated to ROS. As a consequence, this last technique offers a more quantitative and reliable analysis on the concentration of toxic species. Proceeding with these methods, it is possible to investigate the limiting conditions in which ultrasound frequency and power combined with nanoparticles are cytotoxic for cancer cells, without damaging the healthy ones.

Upon finding this range of effectiveness, the project is carried on testing the behavior of mere ZnO nanoparticles or functionalized with amino groups, analyzing also their effect on living cancer cells. Furthermore, in order to investigate their behavior in a dynamic condition, the design of a specific cartridge, along with its fabrication, is performed. Therefore, by using a peristaltic pump, it is

possible to simulate a situation closer to the real one: the blood stream.

Finally, the experimental results are supported and compared to both laminar fluid flow and acoustic pressure simulations performed with COMSOL Multiphysics, providing a better understanding of the physics behind the fluid circulation in the cartridge and sound waves propagation, highlighting their correlation with different channels geometries.

Since this Master thesis is inserted in the XtraUS European project, it aims at developing the findings previously achieved on the same work, and, at the same time, at exploring new possible paths to lay the foundations for the evolution of the research.

Contents

List of Figures

List of Tables

Chapter 1

Introduction

1.1 The XtraUS project and purpose of the thesis work

Nowadays, cancer is the second leading cause of death worldwide, accounting for 19.3 million of new cases in 2020, with almost 10 million of deaths [1],[2]. Nonetheless, the pandemic situation due to the widespread of COVID-19 has contributed to delays in diagnosis and treatments for nonurgent surgeries and procedures, as cancer screening [3]. Even if the specific impact of these restrictions remains unknown for different countries, in general the reduced access to care has hindered the cancer prevention, expecting to cause delayed cancer detection, an increase in advanced-stage diagnoses and cancer mortality in some cases.

A large contribution to cancer deaths comes from systemic disease, a particular condition generated when the cells of a primary tumor spread over the whole body of a patient and affect different organs and tissues, generating secondary tumors, namely metastases. As reported in the study of Dillekås et al. [4], carried on using data of the Norwegian Cancer Registry, the 66.7% of cancer deaths due to solid tumors are caused by metastases. However, on the basis of clinical experiences, this number appears to be lower than the expected one, as it is strictly affected by the accuracy in reporting data: for example, it seems that the metachronous metastases (metastases discovered in a later moment) are underreported.

As a consequence, the metastatic cells responsible for the generation of metastases, divided in circulating tumor cells in the bloodstream (CTCs) and disseminated tumor cells (DTCs) in the bone marrow, are involved in an extensive research.
The XtraUS project, funded from the European Research Council, is aligned with this

perspective, whose main purpose is the prevention of cancer relapse and recurrence in patients considered already healed from their primary tumor. In fact, the minimal residual disease (MRD), left after a curative treatment, can be the cause of recurrence, in particular because of CTCs presence. However, due to their very poor amount in the blood stream, the detection of CTCs is challenging for traditional laboratory tests and an innovative treatment is required. It involves an extracorporeal circulation set-up coupled with the introduction in the blood of definite nanoconstructs, able to respond to an external stimulus, specifically targeted and non-immunogenic. The combination of these two aspects allows for a personalized treatment, improving both the efficacy and safety, while minimizing the possible damage to healthy cells.

This Master Thesis work is inserted in the XtraUS project as a continuation and development of previous studies and researches.
The dissertation starts with an initial overview on CTCs and the different techniques used for the extracorporeal circulation and then, it concentrates on two wide topics: the first one focuses on the impact of nanoparticles in the production of Reactive Oxygen Species (ROS), which are particular toxic molecules whose presence leads to cancer cells death. The analysis is performed by comparing a control with a nanoparticles-enriched solutions under different sonication conditions, in terms of time and ultrasound power. The amount of produced ROS is measured using two different detection mechanisms: at first, Luminol sonochemiluminescence is employed for a fast span over a wide range of possible US power and time combinations, providing a more qualitative analysis. Then, the most relevant conditions are tested using the Electron Paramagnetic Resonance (EPR) Spectroscopy, a slower but more precise technique, allowing for quantitative results. The solutions inserted in a single well of a 24 well-plate are examined and the final ROS production for all the different cases is validated comparing it with cells viability experiments. The results of the different sonication conditions obtained in laboratory are also supported by COMSOL simulations of the acoustic pressure wave inside the two types of wells.
Therefore, the main aim of this first part is to find the most effective and safe range of working mechanism, in which sonication power and time conditions combined with nanoparticles are able to provide a proper damage to cancer cells without affecting the healthy ones.

On the other hand, the second part of the Thesis relies on the design of a cartridge prototype, that represents the starting point of a series of simulations and studies whose aim is to obtain a final cartridge, inserted in the extracorporeal circulation circuit where the blood treatment will occur. According to this setup, the basic idea is to let the blood, properly enriched with nanoparticles, flow inside the channels of the cartridge positioned in contact with an US transducer.

For this reason, during the design procedure, a considerable attention needs to be paid to the fluidic and acoustic requirements that the cartridge shall meet: the fluid has to be described by a laminar flow with an almost uniform velocity to prevent blood pooling and turbulence, responsible for a degradation of healthy cells; at the same time, the cartridge material should have specific acoustic characteristics to perform an effective sonication.
An initial project of the cartridge is 3D printed using the material PEGDA to analyse its resistance to US and its fluidic properties. After several laboratory experiments involving both a peristaltic pump and an US transducer, the need of a new cartridge providing a less turbulent flow was clear. Therefore, different projects are studied by performing simulations on COMSOL Multiphysics regarding both the fluid flow and the acoustic behavior.

1.2 Tumor metastasis and CTCs

1.2.1 The invasion-metastasis cascade and the role of CTCs

Metastases originates from a succession of several cell-biological processes, called the invasion-metastasis cascade, which involves the dispersion of cancer cells through the blood stream or the lymphatic system, allowing them to reach different and distant organs from the primary tumor site. This systemic nature represents the main challenge for its treatment, as well as also the resistance of disseminated cancer cells to the therapeutic agents. Therefore, surgical resection used for the cure of well confined primary tumors is not effective in the presence of already established metastases.
As described in the review article of Valastyan et al. [5],the invasion-metastasis cascade is divided in several biological events (Figure 1.1):

1. Local invasion of the surrounding tumor site through the extracellular matrix (ECM) and stromal cells
2. Intravasation into the lumina of blood vessels
3. Survival during the transport in the blood stream
4. Arrest of CTCs in distant organs
5. Extravasion into the parenchyma of organs distant from the primary tumor site
6. Survival in the new microenvironments to form micrometastases
7. Proliferation and generation of macroscopic, detectable metastasis, termed as metastatic colonization

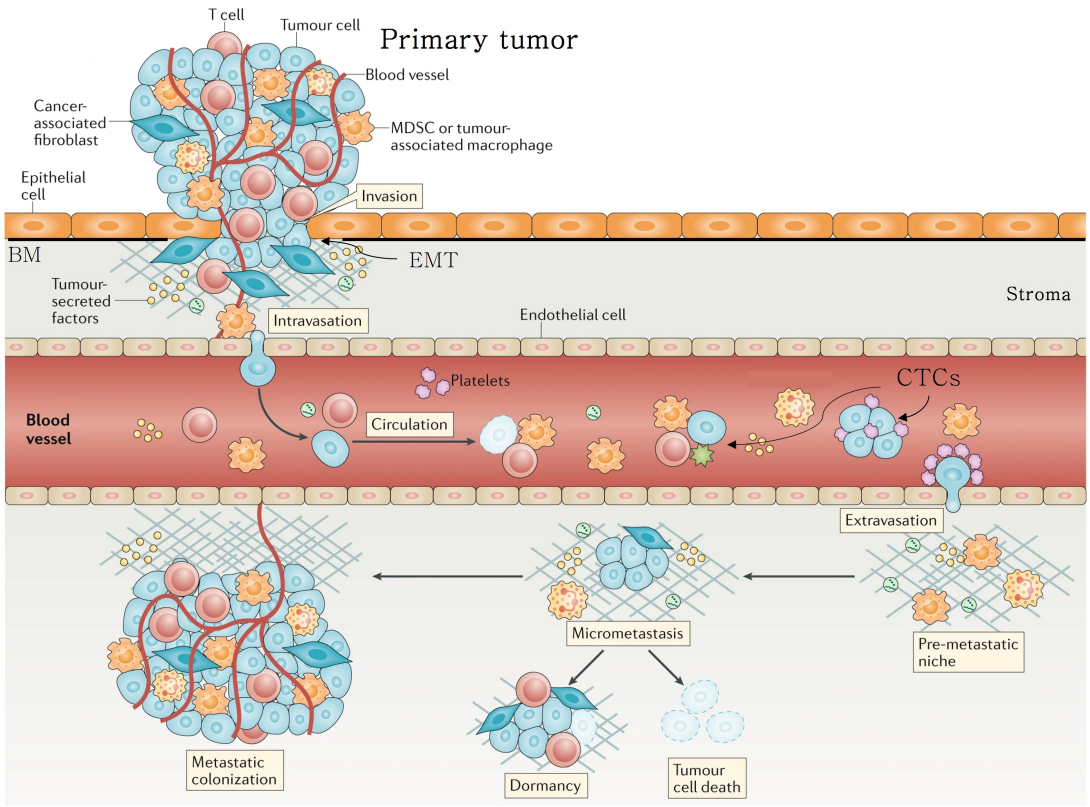

Figure 1.1: Invasion-metastasis cascade scheme [6].

1. Local invasion

In the local invasion process, the cancer cells starts to leave the confined site of the primary tumor, expanding into the surrounding stroma and reaching the parenchyma of nearby tissues. However, they need to overcome the basement membrane (BM), a specialized ECM which plays both an important structural role in the organization of the epithelial cells, separating the epithelial from the stromal components, and also a crucial functional role in the signal transduction with cancer cells, leading to alterations in cell proliferation, survival and invasiveness.

The specifically organized tissue architecture of the epithelium constitute an effective barrier to the expansion of the primary tumor, forcing it to use different invasion schemes strictly dipendent on the particular microenvironmental conditions. These strategies can involve cohesive multicellular units, whose process is called *collective invasion*, or individual tumor cells invasion programs, such as the *mesenchymal invasion*.

In order to overcome the perfectly arranged epithelial tissue, whose cells are tightly connected thanks to E-cadherin-mediated junctions, tumor cells undergoes a biological process

termed epithelial-mesenchymal transition (EMT). EMT is responsible for the degradation of epithelial cells connection, the dissociation of individual cells from the epithelial cell sheets and the transformation of cube-shaped epithelial cells into spindle-shaped mesenchymal cells [7], responsible for an increase in invasiveness and migration properties.
After the degradation of the BM, cancer cells enters the stroma, composed of an increasing number of tumor-associated cells depending on the progression stage of the tumor itself; this phenomenon leads to the formation of an inflamed stroma, which contributes to enhance the aggressive behaviors of cancer cells generating a self-amplifying positive-feedeback loop.

2. Intravasation

After the invasion of the surrounding stroma and the proceeding of the tumor growth, cancer cells can arrive close to lymphatic or blood vessels and, thanks to their ability to cross the pericyte and endothelial cell barriers, that corresponds to the walls of microvessels, they can enter inside the lymphatic system or the blood stream: this process is called Intravasation. Its mechanism is also facilitated by the particular structural characteristics of the new blood vessels generated by the tumor in the local microenvironment, called neangiogenesis. The weak interactions between endhotelial cells and the absence of a large pericyte coverage of the tumor-associated neovasculature are the basis for a leaky and porous configuration, which promotes the access of cancer cells during the intravasation stage.

3. Survival in the circulation - CTCs

As soon as the cancer cells are able to enter within the lamina of blood vessels, they are disseminated on the whole body through the venous and arterial circulation. Since circulating tumor cells represents the vehicles for the formation of secondary tumors, they can be described also as 'metastatic intermediates'. Even if primary tumors can release millions of cells into the circulation, most of them rapidly dies, and by 24h, less than 1% survives. For example, a $1cm$ tumor, composed of almost 1×10^9 cells, can release 1×10^6 cells into the circulation daily. However, metastases are produced from less than 0.1% of the initial released cancer cells [8].
The reason behind the large mortality of CTCs before reaching distant organs is related to the variety of stresses they need to withstand during the hematogeneous circulation, in particular the stresses imposed by matrix detachment, the damages caused by hemodynamic shear forces and the destruction from the innate immune system. When cancer epithelial cells enters within the circulation, they are subjected to anoikis, a form of apoptosis due to the detachment and consequent loss of anchorage to the extracellular matrix. However, since cancer cells are characterized by large dimensions, $20 - 30$ μm, while the lumina

diameter of capillaries is around 8 μm, there is a high probability for CTCs to remain trapped not long after the intravasation stage. This allows CTCs to extravasate before the anoikis mechanism occurs. At the same time, CTCs are able to shield themselves from the shear forces and survive to the innate immune detection by forming interactions with blood platelets, called microemboli, enhancing the possibility to reach distant sites from the primary tumor.

4. Arrest of CTCs in distant organs

Since clinicians noted that specific cancer types tends to form metastases preferentially in defined target organs, the arrest of CTCs at distant organ sites can be described as the combination of both passive and active processes.
Passive CTCs arrest occurs at particular capillaries sites due to their restricted diameter or tortuous layout which hinders the further circulation of CTCs. Hence, they are not able to reach blood vessels whose entrance depends on very thin capillaries. However, some CTCs are able to overcome this passive trapping thanks to their unusual plasticity properties, allowing them to reach more distant sites.
On the other hand, the active process relies on the ability of CTCs to establish ligand-receptor interactions with the walls of the microvasculature, binding preferentially to tissues which favour their trapping.

5. Extravasation

After the arrest in a distant site from the primary tumor, CTCs can generate an intraluminal microcolony within a blood vessel, whose growth may cause a breach on its walls, provoking a direct contact with the tissue parenchyma. Otherwise, cancer cells start to penetrate the endothelial and pericyte layers during their migration from the vessel lumina to the stromal microenvironment, following the opposite steps of the intravasation process, called extravasation. Nevertheless, the main difference between the penetration stages of these two last mechanisms relies on the nature of microvessels and tissues that, being distant from the primary tumor site, can be highly functional with a reduced intrinsic permeability.
Hence, the specific microenvironment surrounding the CTCs plays a major role in the extravasation process and metastasis formation; as an example, the bones and liver, which are composed of highly permeable fenestrated sinusoids even in their normal state, facilitates the penetration of carcinoma cells, while pulmonary microvessels, covered by endothelial cells able to form an impermeable barrier, hinder extravasation.
In order to overcome these barriers of tissues having intrinsic low permeability, primary tumors have the ability to secrete agents capable to perturb the specific distant microenvironments enhancing the tissues permeability to favour the penetration.

6. Micrometastasis formation

As stated before, also the micrometastasis formation considerably depends on the surrounding microenvironment, which can greatly differ from the original one at the primary tumor site. Following the studies of Psaila et al. [9], the issues arising from an incompatible microenvironment are solved by the primary tumor establishing a 'premetastatic niche', which is the final result of a complex mechanism that prepares distant microenvironment sites to the settling of CTCs and growth of secondary tumors. It has been observed that the bone marrow derived haematopoietic cells, which express the vascular endothelial growth factor (Vegf), with pro-angiogenic (formation of tumor-associated new blood vessels) and anti-apoptotic (preventing the tumor cells death) functions, localize to the specific premetastatic site even before the arrival of CTCs. The collaboration between this accumulation of myeloid cells, together with endothelial and stromal cells, residing in the tissue parenchyma, provide an effective platform for the expression of specific chemokine ligands (promote tumor cell homing and engraftment), growth factors and matrix-degradation enzymes preparing the premetastatic site to be properly receptive. As tumor cells are captured, their specific interactions with the molecular species of the 'metastatic niche' play a crucial role in the survival, growth and proliferation of tumor cells.

7. Metastatic colonization

Once the CTCs settles in a foreign microenvironment and survive during the process, different cell-biological mechanisms can happen preventing the proliferation and formation of large macroscopic metastases. Indeed, the majority of disseminated tumor cells may remain quiescent, in a dormancy-like state, due to the presence of an incompatible surrounding microenvironment which hinders their growth, or also they can generate microcolonies whose dimension doesn't change, having no net gain or loss in the overall cell number. In this last case, the micrometastases are able to proliferate with a continuous rate but their development is blocked by an high probability of apoptosis, thus maintaining constant the cell number. Some studies have proposed that the the reason behind this phenomenon relies on the inability of disseminated tumor cells to trigger the neangiogenesis mechanism [10]. The explanation of tumors proliferation failure has been articulated more than 120 years ago by Stephen Paget [11] with his 'seed and soil' hypothesis, that perfectly matches the more recent theory of the 'premetastatic niche'. His assumption was based on the observation of metastases formation at preferential distant organ sites depending on the nature of the primary tumor: the development of metastases occurs at those sites ('soils') that allows the survival and growth of tumor cells ('seeds'). Some microenvironment sites can

be more or less suitable for the proliferation of specific disseminated tumor cells. This study has highlighted the complexity of the whole invasion-metastasis cascade process, able to produce various distinct adaptive programs for metastases generation and proliferation, depending not only on the primary tumor tissue characteristics but also on the nature of the organ site where the metastasis occurs.
However, a small minority of tumor cells complete the whole invasion-metastasis cascade mechanism, overcoming the survival and proliferation issues in the foreign microenvironment site, with the final formation of detectable, macroscopic secondary tumors.

1.2.2 Nanomaterials for the detection and therapeutic targeting of CTCs

Since in the invasion-metastasis cascade, circulating tumor cells play a crucial role in metastases dissemination, they are the subject of an intensive research which focuses on their isolation, characterization, neutralization or direct killing.
While the CTCs characterization enables the monitoring of 'in progress' therapeutic treatments, their isolation and subsequent laboratory analysis allows for the examination of tumor progression and potentially for early tumor detection. In fact, for some tumors has been demonstrated the presence of CTCs in the blood circulation also in the case of small primary tumors, still at their early stages of growth (e.g. breast cancer), [12].
Nevertheless, all these analysis are intrinsically difficult due to the particular properties of CTCs. The first challenge relies on their extremely low concentration, around one CTC in 1mL of blood, surrounded by millions of white blood cells and billions of red blood cells. A second issue is based on their heterogeneous population with different molecular characteristics, lacking a unique identifiable marker. Therefore, techniques having an high specificity, ability of simultaneous detection and handling of few cells are required.
As described in the work of Z. Zhang and M. King [13], the studies and development of nanoscale materials as liposomes, polymeric nanomaterials, magnetic nanoparticles, gold nanopraticles, quantum dots and graphene have shown their consistency with the strict requirements needed for CTCs analysis. Actually, the high specificity is assured by properly functionalizing the nanomaterials surface with CTC-targeting ligands (biomarkers), able to bind to the specific CTCs counterpart. Hence, by adding different biomarkers on the nanomaterials surface, all the associated CTCs can be potentially captured, overcoming the problem of heterogeneous CTCs population. In Table 1.1 are presented the main characteristics of the different nanomaterials, anticipating their description in the following sections.

Nanomaterials	Pros	Cons
Liposomes	Biocompatibility, long blood circulation time	Low stability
Polymeric nanomaterials	Biocompatibility and biodegradability, ease for chemical modification	Low stability
Magnetic NPs	Biocaompatibility, magnetic separation	Magnetic aggregation
Gold NPs	High stability, laser-controlled simultaneous detection and ablation	Non-biodegradability
Quantum dots	Quantitative detection with high sensitivity	Toxicity
Graphene/Graphene oxides	Ultra high specific surface area for multiplex functionalization	Non-specific cellular internalization

Table 1.1: Comparison between the different nanomaterials [13].

Liposomes

Thanks to the particular structure of liposomes, they have been soon recognized as potential drug delivery systems by taking advantage of their ability to encapsulate small molecules drugs and genes. The basic components of liposomes are phospholipids, which assemble in spherical shells when introduced in aqueous solutions, generating a final thermodynamically stable vesicle, composed of at least one lipid bilayer. The aqueous core together with the presence of lipid bilayers allows for the encapsulation of both hydrophilic and lipophilic molecules. This configuration provides the prevention of drugs degradation during their storage, the reduction of toxicity to healthy tissue and the possibility to perform an active targeting by decorating the outer surface with specific antibodies and ligands.
According to the studies of Z. Zhang and M. King [13], liposomes can be effectively used to target and neutralize CTCs in the circulation and reduce the probability of metastases formation. They employed the tumor necrosis factor (TNF) apoptosis-inducing ligand (TRAIL), a cancer therapeutic able to selectively induce apoptosis in a variety of tumor cells, sparing most of normal cells. Therefore, the liposomes surface was functionalized with TRAIL and with an adhesion receptor, E-selectin (ES), which can selectively recognize and target the majority of leukocytes. After their intravenous administration, they bind to the target leukocytes, converting them into 'hunter of CTCs' thanks to the expression of TRAIL moieties on leukocytes surface (Figure 1.2).

The effectiveness of leukocytes functionalized with ES/TRAIL liposomes is demonstrated experimentally by treating human blood in a cone end-plate viscometer, with the addition of a fluorescent label to the liposomes surfaces. The significant decrease of the cancer cells viability in blood is supposed to be caused by the compressive forces between

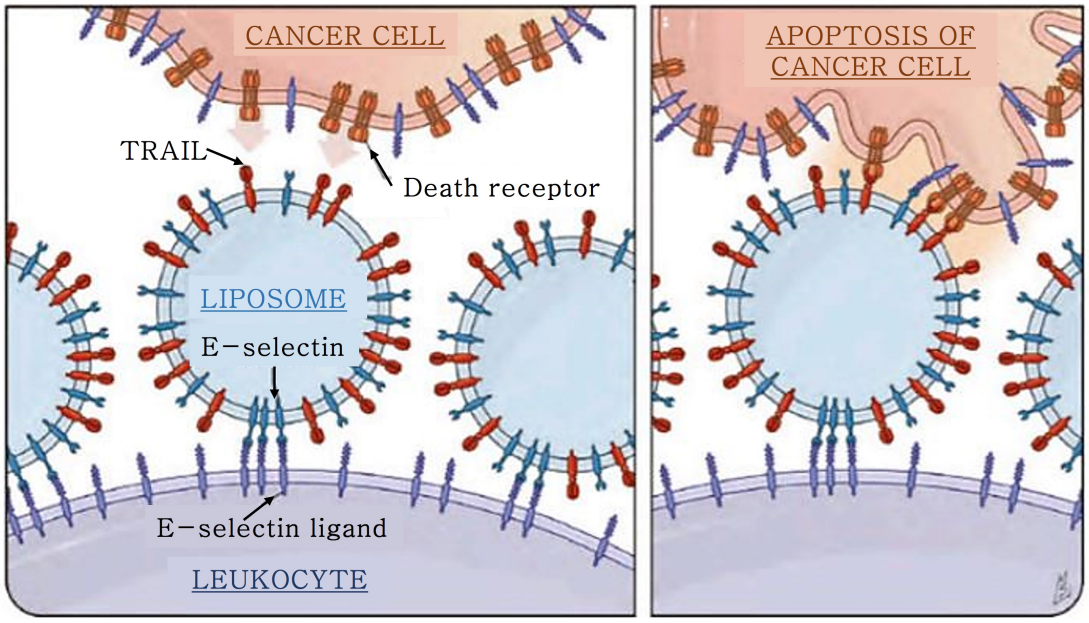

Figure 1.2: Leukocytes surrounded by ES/TRAIL liposomes inducing apoptosis in cancer cells [13].

CTCs and leukocytes during the flow in the bloodstream, which favour the approaching of TRAIL to the cancer cell death receptors to induce apoptosis. Essentially, CTCs become surrounded by the circulating leukocytes, thanks to both adhesion receptors and TRAIL ligands, as soon as cancer cells are released into the blood stream.

Polymeric nanomaterials

Since the 1970s, polymeric nanomaterials are employed as drug delivery systems because of their biocompatibility, biodegradability and their tunable chemical and physical properties by controlling the synthesis process. Their final structure is obtained through the self-assembly of linear block copolymers in aqueous solution, generating nanoscale core-shell particles, called 'micelles', composed of an hydrophobic core and an hydrophilic shell. Hydrophobic drugs can be inserted in the core while hydrophilic ones can be loaded through electrostatic attraction or chemical conjugation. Following recent researches which focus on the study of stimuli-responsive polymers, the drugs loaded in the micelles can be released by applying an external stimuli, such as light, pH, temperature and mechanical stress.
However, most polymers used for CTCs capture are incorporated in microfluidic devices, without forming micelles; there are only few studies which employ free micelles. Alternatively, other polymers are used for CTCs capture, such as the dendrimers, characterized by

a highly branched structure which arranges in a spherical nanoscale configuration. Thanks to the high density of functional groups on their surface, the dendrimers are exploited to improve the selectivity and sensitivity of CTCs capture devices, by conujugating the dendrimers to a CTC detection platform. In the experiment of Myung et al. [14], dendrimers are first bound to a glass substrate platform using PEG (Polyethylene glycol) linkers, and then incubated with anti-EpCAM (EpCAM - epithelial cell adhesion molecule, a marker expressed on the surface of some CTCs), providing the proper functionalization for the capture of CTCs.

Magnetic nanomaterials

Magnetic nanomaterials, involving single dispersed nanoparticles (MNPs) or also clusters of MNPs embedded in a organic or inorganic matrix, are mainly employed in the isolation of CTCs from the circulation. The main advantage of this class of nanomaterials is the possibility to move them and control their position by applying an external magnetic field. MNPs are usually made of iron oxide, the most used thanks to its biocompatibility and chemical inertness as well as cobalt ferrite and chromium dioxide. Depending on their size, iron oxide nanoparticles may show a ferromagnetic behavior, which maintain a net magnetization even upon removal of the magnetic field, or a superparamagnetic behavior, without any magnetization in absence of magnetic field. Since ferromagnetic nanoparticles tend to attract each other due to the remaining magnetization and cannot stay permanently dispersed, superparamagnetic ones (SMNPs) are usually employed. Their surface can also be properly coated or functionalized to improve the solubilization and to conjugate ligands and receptors for the selective CTCs targeting.

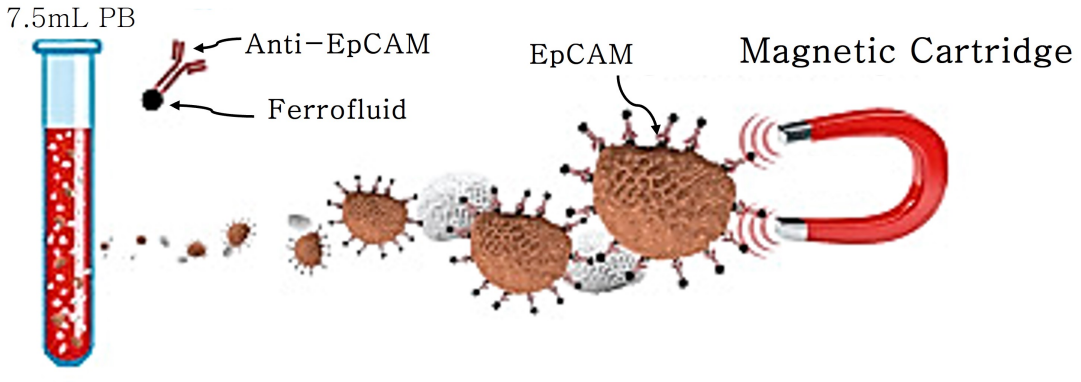

Figure 1.3: CellSearch working mechanism [15]: it can enumerate CTCs in 7.5 mL of peripheral blood (PB).

This working principle is at the basis of CellSearch, the first FDA (Food and Drug Administration) approved instrument for CTC isolation and analysis. It uses magnetic iron oxide beads coated with antibodies against the tumor cell markers EpCAM to bind to the CTCs. Then, the beads are moved by applying a magnetic field and bring with them the captured CTCs, finally removed from the blood sample (Figure 1.3). After that, the cells are labeled with a fluorescent moiety that allows for their enumeration by an automated cell imaging and analysis system.

Gold nanoparticles

The interest in gold nanoparticles resides on one hand, on their biocompatibility and chemical inertness, making them suitable for biomedical applications, and on the other hand, by their enhanced light absorption and scattering processes, useful for CTCs detection. In fact, photoacustic signals or shifts in Surface Plasmon Resonance (SPR) can provide a quantitative analysis of CTCs. SPR is an optical phenomenon generated by light when it interacts with conductive NPs (metal) having dimensions smaller than the incident wavelength. The electric field of incident light excite electrons of the conduction band, resulting in coherent localized plasmon oscillations at a resonant frequency, that depends on the size, shape, composition, dielectric environment and distance between the NPs. These plasmon NPs are also able to convert the incident light into thermal energy, producing heat in the surrounding environment.

There are different methods that exploits gold NPs for the CTCs targeting and detection. In one of them [13], Au NPs are properly functionalized with CTC-specific ligands and are directly injected *in vivo* for the detection and enumeration of CTCs (e.g. gold-plated carbon nanotubes conjugated with folic acid are employed to detect breast cancer cells in the work of Galanzha et al. [16]). The main advantage of this real-time monitoring technique is that it allows to bypass the blood sampling, blood preparation and CTCs isolation steps, required for the majority of CTCs detection techniques. However, in order to be effective, Au NPs should withstand the high shear forces in the blood circulation, not being removed by the immune system and avoid accumulation on some organs.

Alternatively, there are also techniques exploiting the heat generation of Au NPs, as the photoacustic flow cytometry used for the detection and removal of CTCs *in vivo* (e.g. as presented by Galanzha et al. [17], melanoma cells can be labeled by gold nanorods, GNRs). In this mechanism, a laser beam is let through the skin and focused into a vessel; then, the acoustic vibrations produced by the absorption of the radiation from the Au NPs is detected. By further increasing the energy of the laser beam, the plasmonic Au NPs starts

to heat up, leading to the final ablation of CTCs.

Quantum dots

Quantum dots (QDs) are mainly employed in biomedical imaging field, since they are powerful fluorescent imaging agents for *in vitro* applications. In fact, when compared to conventional dyes, QDs result to have better properties such as the larger extinction coefficients and quantum yields, responsible for a brighter emitted light, the resistance to photobleaching, providing a continuous dynamic imaging that can last also hours, and the broader absorption spectra and narrower emission spectra, allowing for a higher sensitivity. The materials used for QDs are usually ZnS, CdS, ZnSe, CdTe or PbSe and their surface can be further coated or functionalized with polymeric ligands to overcome their solubility issue.

Thanks to the stability of the fluorescent emission, QDs are exploited in CTCs detection in *ex vivo* processes, while, due to the production of heavy metal toxicity, QDs are not employed for *in vivo* techniques.
One of their application is based on the use of QDs as fluorescent probes for CTCs detection by functionalizing their surface with specific receptors. Since the ultimate goal is the simultaneous detection of different CTCs, a study has been held on this subject [18]. Three QDs having different sizes, therefore emitting at different wavelength, are decorated with antibodies against EpCAM, epidhermal growth factor receptor (EGFR) and human epidermal growth factor receptor (HER-2), respectively. Then, a mixture of these QDs is used to sort three different breast cancer cell lines. As a final result, the capture efficiency is found to be high, 87.5% as well as the identification accuracy of around 92.4%. Furthermore, the CTCs viability is not influenced by the process, thus improving the subsequent laboratory analysis.

Graphene and graphene oxides

Graphene is characterized by very peculiar physicochemical properties, such as extremely high mechanical strength, intrinsic mobility and electrical conductivity. Moreover, being intrinsically a sheet of graphite, it has a large surface area available to be functionalized on both sides. In fact, graphene is a two-dimensional layer composed of carbon atoms hybridized as sp^2 and arranged in hexagonal shaped structures.
However, many of CTCs capturing and imaging techniques involve the oxidized form of graphene, known as graphene oxide (GO), thanks to its fluorescence quenching property. The presence of hydroxyl and carboxyl groups on its surface allow for the chemical bonds with dye conjugates, while the sp^2 hybridization is responsible for the quenching. As practical example, in the work of Viraka Nellore [19], different types of aptamers are covalently

conjugated to porous graphene oxide membranes with the aim to capture the associated different tumor cells in a simultaneous and selective way, from an infected blood sample. Due to the quenching property of GO, when the dye conjugated aptamers are attached to graphene oxide, the dye fluorescence is completely quenched. Then, as shown in Figure 1.4, when the cancer cells bind to the dye conjugated aptamers, the distance between the dye and graphene oxide increases, therefore enabling the fluorescence.

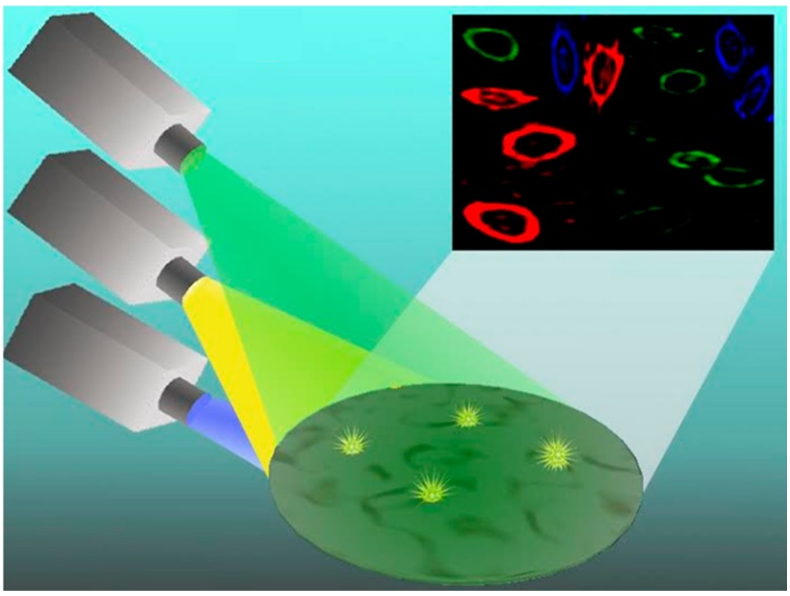

Figure 1.4: Different types of cancer cells detected simultaneously thanks to the dye conjugated aptamers attached to a GO membrane [19].

Chapter 2

First part - Synergistic action of US and NPs

2.1 Introduction

Before starting with the description of the synergistic action of ultrasound waves and stimuli-responsive nanoparticles, an overview of an already established clinical technique, called Extracorporeal photopheresis (ECP), is necessary. In fact, the whole work and study carried out for the thesis dissertation were inspired by ECP mechanism, based on the combination of Photodynamic therapy (PDT), which uses light as external stimulus rather than ultrasounds, and leukapheresis process for the extracorporeal circulation.

2.1.1 PDT - Photodynamic therapy

Photodynamic therapy is a treatment procedure for cancer and non-infectuous deseases, such as vitiligo, macular degeneration and psoriasis, [20], which involves three separately nontoxic components: a photosensitizer (Ps), a light source that emits visible or near-infrared (NIR) light, and molecular oxygen available in the tumor tissue. Their combination induce the generation of Reactive Oxygen Species (ROS), responsible for cell death, mainly through the direct mechanisms of apoptosis or necrosis [21].

PDT working principle relies on the light excitation of the photosensitizer: the photons, coming from the light source and having a specific energy, are absorbed from the Ps molecular compound, promoting its electrons to higher energy levels. As a consequence, Ps passes from a ground state to an excited singlet state (PS_{E_s}) and then, through an intersystem crossing process, which is non-radiative, it relaxes to its triplet excited state

(PS_{E_t}). At this stage, two different mechanisms are possible depending on the interactions with the surrounding environment, as shown in Figure 2.1:

1. In type I reaction, Ps can directly react with several biomolecules, as lipids, proteins and nucleic acids, forming different radicals. At the end of the process, different ROS are generated, such as O_2^- and H_2O_2. In particular, the final production of strongly reactive hydroxyl radicals, OH^-, seems to provide a more effective Photodynamic effect.

2. A type II reaction consists on the reaction between Ps in its triplet excited state with molecular oxygen in the ground state. The majority of Ps undergoes the type II mechanism, with the final generation of singlet oxygen, leading to the oxidation of surrounding biological species.

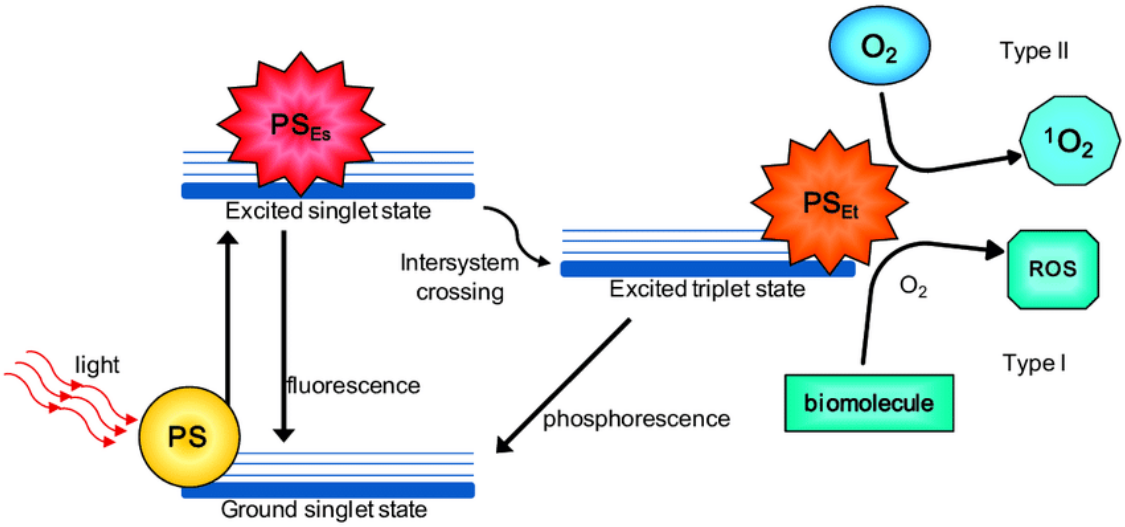

Figure 2.1: PDT mechanism [20].

The two reaction types occur simultaneously and their balance depends on the Ps nature (mainly organic molecules as porphyrins, chlorins and other molecules as chlorophylls), the amount of oxygen available and the affinity of the Ps with the environment. Furthermore, since ROS and singlet oxygen have an high reactivity and quite short half-life, only the biological tissues located close to the site of ROS production are affected by their action, providing an intrinsic localization of the PDT treatment. However, this phenomenon makes impossible the use of PDT for disseminated metastases on the whole body.

The main advantages of the PDT treatment are the lower invasiveness than surgical procedures and fewer side effects than chemotherapy and radiotherapy, it provides the destruction of tumor vasculature other than the tumor itself, it can be repeated several times on the same site and leave no scars after the healing. The positive and negative features of PDT are resumed in Table 2.1 .

Advanatges	**Disadvantages**
Fewer adverse effects	Photosensitivity after treatment
Little invasiveness	Low penetration depth in case of UV radiation
Short treatment time	No cure for disseminated metastases
Usable in outpatient settings	Tissue oxygenation is crucial to the photodynamic effect
Can be applied at the same location several times	Treatment efficacy depends on accurate light delivery to the tumor
Little or no scar after healing	Photosensitizer photobleaching and degradation

Table 2.1: Pros and cons of PDT treatment [20].

On the other hand, some problems affect the PDT; first of all, the photosensitizers are subjected to degradation, photobleaching and, since they disperse everywhere once they are injected into a human body, another issue is the lack of tumor selectivity, so that the light excitation has to be specifically directed on the tumor site (to not irradiate Ps in normal tissues).
Secondly, two major issues of the PDT treatment concerns the penetration depth and efficient delivery of light. In fact, when the light source comes into contact with tissues, it can be absorbed, reflected, transmitted or scattered, and its penetration depth depends on several factors as the photon energy, the absorption coefficient, the polarization, the tissue physiology, the power density and time of treatment. Since photons having short wavelengths, as UV radiation, are the most scattered by tissues, a deeper penetration depth is given by photons having lower energy and longer wavelength, in the range $700 - 1000\ nm$. However, the light with too low energies, $\lambda > 850\ nm$, is not so effective in ROS generation due to thermal effects produced by fast non-radiative transitions. Therefore, in order to reach deeper areas, the most relevant wavelengths are between 650 and 850 nm, in the near-infrared (NIR) range (Figure 2.2), [21].
Since photosensitizers are mainly excited by UV light, only superficial tumors, such as melanomas and cancers of skin can be treated. In order to improve this limitation, the

chemistry of photosensitizers can be modified so to be excitable by NIR light, or alternatively, light fibers can be inserted into the human body to illuminate internal organs and deeper locations.

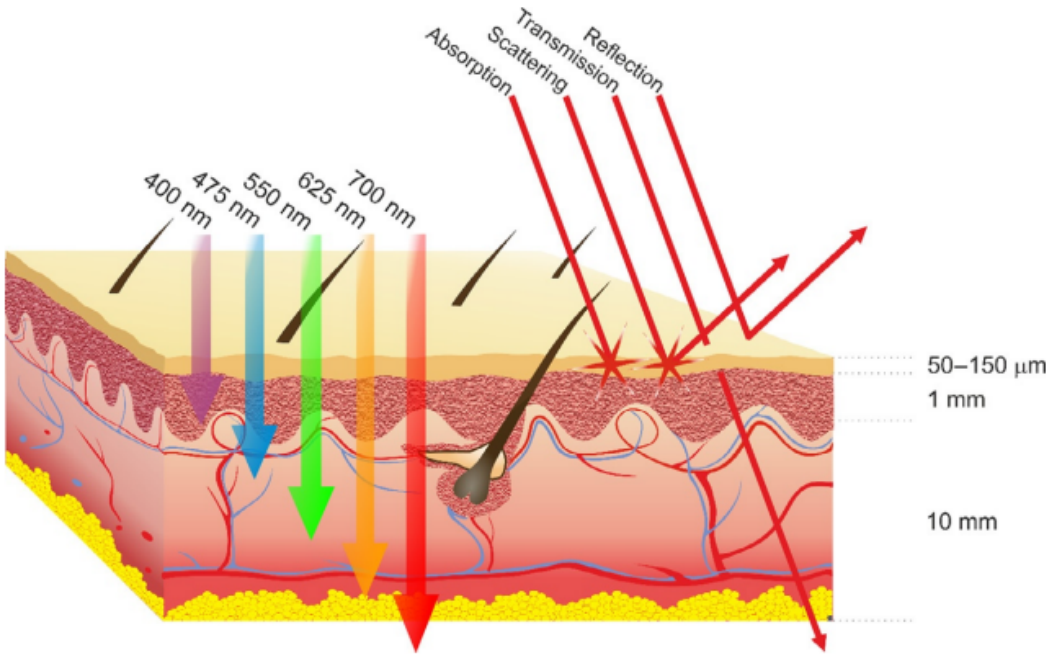

Figure 2.2: Interactions between the incoming light and tissues [21].

Also nanoparticles can be used alone or combined with a photosensitizer to improve the efficacy of PDT. Photo-activable materials are required, able to promote electrons in the conduction band due to irradiation and, therefore, able to produce ROS. These can be carbon based materials (fullerene, graphene, CNT) or also metal oxides, in particular zinc oxide and titanium dioxide.

2.1.2 Extracorporeal photopheresis

As previously mentioned, extracorporeal photopheresis (ECP) is a cell-based immunotherapy [22] that relies on the combination of leukapheresis, a particular type of apheresis procedure responsible for the separation of white blood cells from a blood sample in an extracorporeal circulation set-up, and PDT, employed to treat the already collected leukocytes.

This treatment has been introduced for the first time in 1987 by Edelson et al. [23], presenting a study on patients affected by Sézary syndrome, a leukemic and aggressive form of cutaneous T-cell lymphoma (CTCL) [24], in which cancer cells do not remain confined in the skin but are also released in the blood stream. They employed psoralen, that is a mutagen, a particular chemical agent with the ability to modify permanently the genetic constituents in an organism, such as nucleic acids and DNA, in combination with UVA irradiation ($320 - 400\ nm$), in a technique called PUVA (psoralen+UVA). More specifically, 8-methoxypsoralen (8-MOP) was used as photosensitizer since, thanks to the UVA interaction, it becomes highly reactive and binds to DNA and proteins, leading to the cell death through apoptosis [25].
However, the efficacy of this treatment relies not only on a specific defined process but on several simultaneous effects whose mechanism is not yet completely understood. In particular, the contact of cells with plastics and the tubing system favours the differentiation of monocytes, a particular type of leukocytes, into dendritic cells. After the re-infusion, these cells phagocyte the apoptotic lymphocytes, caused by the PUVA treatment, and begin to present specific antigens on their surface, triggering an immune response against T-cell lymphoma, thus inducing the suppression of growing tumor cells [22], [26], [27].
Another effect arising from this type of treatment is the increased production of hydrogen peroxide and, more in general, of various reactive oxygen species following the irradiation with UVA light. A further enhancement of H_2O_2 is obtained in the cells previously treated with 8-MOP, since CTCL cells are more sensitive to the effects of 8-MOP than healthy lymphocytes. This higher amount of intracellular ROS causes a permanent damage to the cancer cells, resulting in a final cell death [27].

The first ECP device was quickly approved one year later, in 1988, by the United States Food and Drug Administration and it was characterized by a single, fully integrated medical device known as "closed" or "on-line" ECP system (UVAR®, Therakos®). It includes the three different stages of an ECP process, namely the cell separation, the UVA treatment and the re-infusion in the patient, combining them in a unique step thus to minimize the health risks related to infection and contamination as well as improper re-infusion.
This configuration differs from another type of ECP mechanism, called the "open" or "off-line" system, consisting on two different medical devices for each process: a cell separator and a specific equipment for UVA irradiation. However, while the two devices are separately approved, they are not approved together for ECP treatment.

Nowadays, it's more than 30 years that the ECP treatment is employed: it started with the cutaneous T-cell lymphoma (CTCL) and then it was extended also for the treatment of other diseases, such as for sclerosis, dermatitis, after solid organs transplantation and

for the graft-versus-host disease (GVHD) occurring after stem cell transplantation.

Therakos®, CELLEX® Photopheresis System for CTCL treatment

In this section, a specific research on the working mechanism of the already approved medical device for ECP treatment, Therakos®CELLEX® Photopheresis System, is carried on since its operating principle is of great importance for the development of a parallel device based on an extracorporeal circulation set-up combined with sonodynamic therapy rather than photodynamic treatment.

This system is mainly exploited for the cure of the skin manifestations of Cutaneous T-cell Lymphoma, a cancer affecting the immune system, in particular the T lymphocytes. The T cells belong to the white blood cells and plays an important role in the adaptive immune system, a particular branch of the immune system that shows an high specificity towards each particular pathogen the human body encounters. In fact, it is responsible for the elimination of pathogens, the prevention of their growth thanks to specialized cells, among which the T cells play a crucial role and, finally, it creates an immunological memory following the response to a pathogen, so that a faster and enhanced response is obtained in case of future encounters with the same pathogen.
In CTCL, T-cells undergoes a mutation turning into malignant cells, characterized by contorted nuclear contours, that infiltrate in the dermis or epidermis or forming aggregates into the skin. The main manifestions of CTCL include patches and plaques in the early stages, cutaneous tumors, ulcerations and diffused erythroderma as the disease progresses. The European Organisation for Research and Treatment of Cancer (EORTC) classifies Cutaneous Lymphomas with different types of CTCLs, involving mycosis fungoides (MF), considered a milder form of disease in its early stages, and Sézary's syndrome, the aggressive leakemic form that can affect also other organs [26], [28].
However, ECP is used mainly in the case of severe disease and conditions in which other therapies have failed.

The Therakos® CELLEX® Photopheresis System consists in an apparatus for extracorporeal blood circulation in which blood undergoes to several treatment steps, starting from the collection of blood from the patient, the psoralen infusion, the consequent blood treatment under UV light and finishes with the re-infusion of the blood to the patient [29]. By following the blood pathway the whole process can be separated in different stages as shown in Figure 2.3, while the individual components of the device are presented in Figure 2.4.

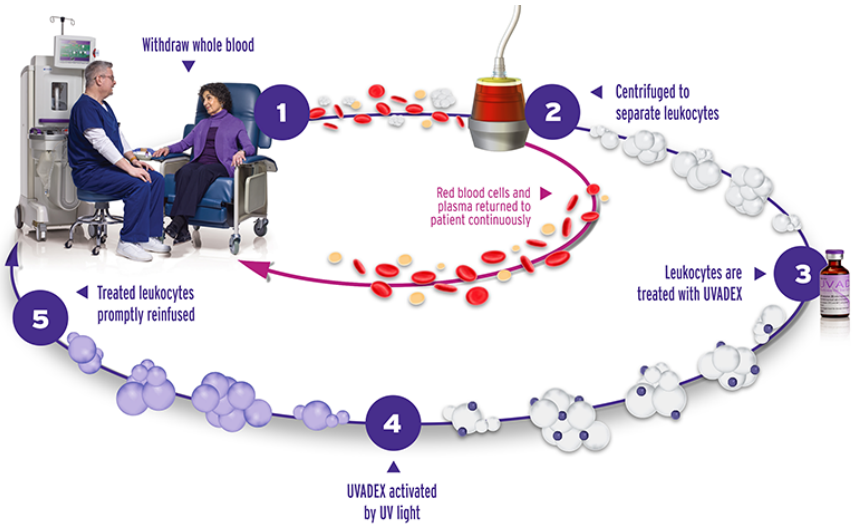

Figure 2.3: Therakos® CELLEX® Photopheresis System working mechanism [29].

Figure 2.4: Therakos® CELLEX® Photopheresis medical device [29].

1. **Collection of blood**. As initial stage, the blood is collected from the patient through a double-needle continuous flow treatment, with the possibility to change to single needle mode if one access fails during the treatment or depending on the patient needs.
   More specifically, to minimize the risk of infection, peripheral venous access is recommended, with the use of a large gauge device for the drawing procedure and a smaller gauge for the returning in the case of double-needle condition.
   The double-needle mode allows for a continuous flow technique, characterized by two access, one for the extraction of blood from the patient and one for the re-infusion, so that simultaneously to the collection of the whole blood, plasma and red blood cells can be returned to the patient. The main advantages of this process consist in the minimization of extracorporeal volume needed (around 280 mL) and the reduction of the overall procedure time (the treatment can last from $1h15$ to $2h50$).
   On the other hand, the single-needle mode is employed when the patient has critical veins and it is characterized by a discontinuous flow in which the plasma and red blood cells are stored in a reservoir bag and intermittently returned to the patient.
   Therefore, in this first step, the whole blood is removed from the patient and sent to the Therakos® CELLEX® photphoresis system.

2. **Separation of blood by centrifugation**. The blood is transferred to a centrifuge, employed to separate the whole blood in its different components: red blood cells (RBC), white blood cells and plasma. The continuous rotation of the centrifuge bowl, with a velocity of 4800 revolutions per minute, allows for their separation and at the same time, it is properly selected in order to prevent blood haemolysis. Since red blood cells have an higher density, they tend to accumulate in the outer area of the centrifuge, while white blood cells, due to their lower density, are collected at the center. In between there is the plasma having an intermediate density. A Bowl Optic Sensor, characterized by a laser beam focused on the centrifuge, is able to detect the RBC/plasma interface and monitors the expansion of the buffy coat (composed by white blood cells). As the separation mechanism proceeds, the RBC and plasma are already removed from the centrifuge and re-infused in the patient, passing from a return bag placed on the right side of the device.
   When the target amount of buffy coat is reached, the collection of white blood cells begins. It occurs by extracting a small amount of additional blood from the patient which displaces the red blood cells upwards, pushing the leukocytes fraction on the top of the centrifuge, providing their collection with low RBC contamination. Then, the buffy coat is directed towards the Fluid Management System, the central part of the device, and passes through an hematocrit sensor which detects the red blood cells concentration. When this concentration overcome the threshold value, it means that

all the buffy coat has been removed from the centrifuge, and the tube is occluded.

3. **Leukocytes treatment with UVADEX.** Then, the buffy coat is collected inside the treatment bag and when the target level is reached, the photoactive substance, UVADEX®, is inserted inside the bag using a syringe. This is a sterile solution containing methoxsalen (8-MOP) with a concentration of 20 µ$/mL$. As previously discussed, when methoxsalen is irradiated with UVA light, it starts to covalently bind with DNA, forming bonds with a single strand of DNA, called monofunctional adducts, as well as also with both the strands of DNA, namely bifunctional adducts. This process leads to the inhibition of DNA synthesis, cell division and epidermal turnover, resulting in the cell death upon photoactivation. Furthermore, methoxsalen is rapidly metabolized in humans, with 95% of the drug excreted through urine after 24h.

4. **The UV treatment and UVADEX® photoactivation.** After the injection of methoxsalen, the buffy coat circulates inside the channels of a photoplate, inserted in between 18 UV lamps which deliver the right amount of light for the photoactivation, approximately around $1.5 - 2$ J/cm^2 of UVA radiation. The time needed for the treatment depends on several factors, such as the concentration of remaining red blood cells inside the buffy coat, leading to a longer photoactivation time with an higher amount of RBC, the volume of the buffy coat itself and the life time of UV lamps. However, the buffy coat flows in the photoplate with definite flow rate of around 100 mL/min.
   An insight on the particular technical project of the cartridge will be discussed in Chapter 3, since it served as an inspiration for the design of the cartridge for the sonodynamic therapy.

5. **Reinfusion of treated buffy coat.** After the buffy coat is completely treated, it is reinfused in the patient by the return line. Then, the apoptotic cells accumulates in the liver, spleen and lymphonodes where they are eliminated.

The whole process can be easily controlled by the operators using a user-friendly interface, consisting in a display monitor through which it is possible to customize the treatment depending on the patient needs. The main features that can be manually changed are the fluid balance limit, A/C ratio, collect/return flow rates, bowl optic threshold value, the whole blood process, and the informations of completed blood prime procedure. It also includes alarms to alert of special operating conditions or arising problems.

To conclude, some additional information should be added: during the entire mechanism, an anticoagulant, Heparin, is employed to prevent blood clotting, while a saline solution

is used before and after the treatment to clean the tubing system and the centrifuge. Furthermore, air detectors, based on digital ultrasonic pulses, are exploited to detect possible air bubbles in the different lines.

2.1.3 SDT - Sonodynamic therapy

At the end of this introductory part, a particular attention is given on the description of the Sonodynamic therapy (SDT) characteristics, that represents the main topic of the whole thesis work.

Sonodynamic therapy is born as an alternative approach for cancer treatment, combining the application of an external, low-intensity ultrasound wave, and molecules, called the sonosensitizers, activated by the sonication process. The major mechanism on which the SDT process relies on is called the acoustic cavitation, a particular event generated by ultrasounds. Even if the Sonodynamic therapy has a working principle similar and parallel to the photodynamic therapy (Figure 2.5), the use of ultrasounds as source of stimulation rather than light, overcomes the main limitation imposed by PDT: the inability of light to penetrate deeper into tissues. In fact, since ultrasounds are not affected by the same mechanisms of scattering, absorption, reflection and transmission of light at the interface with tissues, they provide an higher tissue penetration depth, up to several tens of centimeters with minimal damage to the surrounding normal cells [30].

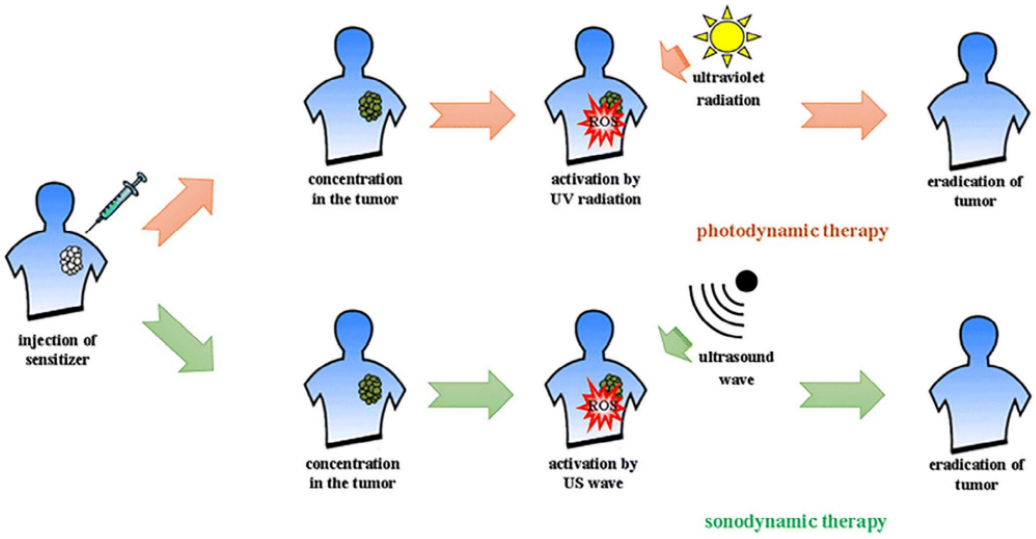

Figure 2.5: Parallelism between SDT and PDT [31].

Ultrasounds

Ultrasounds are sound waves with a periodic vibration frequency higher than that perceived by the human hearing (25 kHz) and propagate into a medium causing an alternation of mechanical rarefaction (R) and compression (C) cycles (Figure 2.6).
Us waves are usually generated by specific devices, composed of a voltage generator, a compensating amplifier and a piezoelectric transducer, able to convert the electrical input into a mechanical displacement. The motion of the upper face of the transducer produces the sound waves that propagates in the surrounding medium.

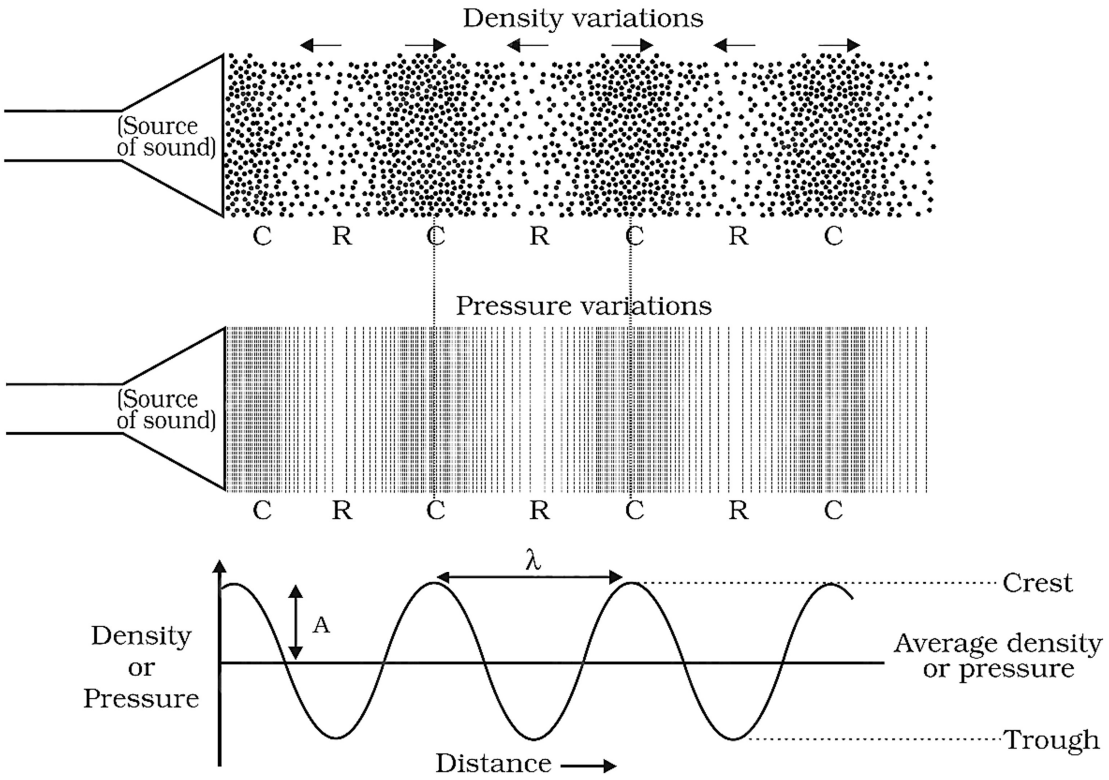

Figure 2.6: Schematic representation of a sound wave.

The sound waves are often described in a simplified way in terms of sinusoidal plane waves, characterized by a certain amplitude, A, that represents the maximum, temporarily displacement of particles in a medium from their original unperturbed positions due to the wave propagation, the wavelength, λ, expressed in metres (m), the frequency, f , measured in Hertz (Hz), and the speed of sound, c, in m/s. The relationship between them is governed by the equation:

$$\lambda = \frac{c}{f} \tag{2.1}$$

In particular, the speed of sound strongly depends on the material through which the sound wave is travelling and it is expressed as:

$$c = \sqrt{\frac{K_s}{\rho}} \tag{2.2}$$

where K_s is the bulk modulus or compressibility, related to the stiffness of the medium, and ρ is its density. Therefore, in fluids, the speed of sound is affected by only these two parameters: it increases with the stiffness and decreases with an higher density of the substance.

However, while in the case of gases, plasma and liquids, the sound waves propagates as longitudinal, compression/rarefaction waves, in solids the transmission is different and occurs both as longitudinal and transverse waves. The transverse component applies a certain shear stress on the solid and, for this reason, the transverse speed depends on the shear modulus (G) of the medium and on its density (rather than the bulk modulus):

$$c_t = \sqrt{\frac{G}{\rho}} \tag{2.3}$$

As a consequence, in solids the speed of sound relies on an additional property which is the shear deformation.

An important parameter that determines the transfer of acoustic energy between two media is the acoustic impedance (Z), described as the resistance of a medium to the displacement of its particles when an acoustic pressure wave is applied. It is given by the product of the density through which the sound wave travels and its velocity:

$$Z = \rho \cdot c \tag{2.4}$$

Since the sound wave propagates differently depending on the nature of the medium, when it reaches an interface between two different substances, it can be partially transmitted and reflected according to the intrinsic difference between the acoustic impedances. As shown in Figure 2.7a, an acoustic wave impinging on an interface between a first medium, whose impedance is Z_1, and a second one, with impedance Z_2, generates a reflected and a transmitted waves whose intensities are described by the transmission (T) and reflection (R) coefficients:

$$T = \frac{2Z_2}{Z_1 + Z_2} \tag{2.5}$$

$$R = \frac{Z_2 - Z_1}{Z_1 + Z_2} \tag{2.6}$$

As an example, the steel-water interface (Figure 2.7b) produces very different transmitted and reflected waves: since steel has an impedance $Z_1 = 46.5 \times 10^6\ kg/(m^2 s)$ and water $Z_2 = 1.5 \times 10^6\ kg/(m^2 s)$, the reflection and transmission coefficients are respectively $R = -0.938$ and $T = 0.063$.
This means that the reflected wave has an amplitude that is 93.8% of the incident wave with an added phase of 180° to its phase term, implying that when the incident wave is compressive, the reflected wave is tensile [32].
Instead, the transmission is lower, being only the 6.3% of the incident amplitude and thus, the transmitted amplitude greatly decreases compared to the incident one, while maintaining the same phase.

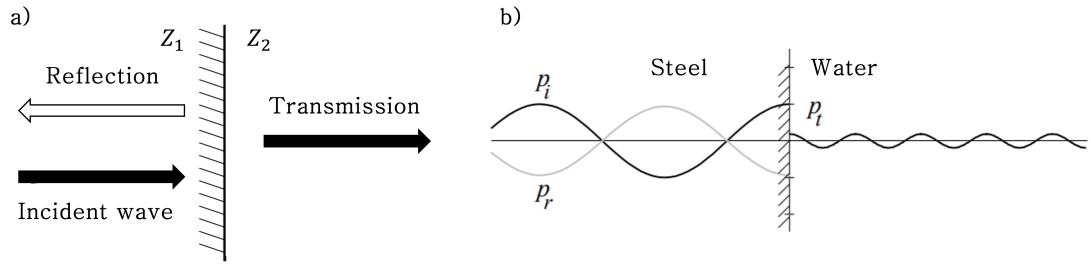

Figure 2.7: a) Reflection and transmission components of an incident acoustic wave. b) Particular case of steel-water interface. [32]

Acoustic cavitation

The US interaction with tissues during the propagation causes both thermal and non-thermal effects.

The thermal effects are related to the absorption of US wave during the propagation, which generates compressive and decompressive mechanical forces, inducing friction inside the tissues. These friction effects are the reason for the increase in temperature and local heating. Since a high temperature can lead to the cancer cell death through necrosis, the thermal effects can be enhanced by using high intensity focused ultrasound (HIFU) waves to induce hyperthermia, with an increase in the temperature up to 80 $°C$ [31], and provide

the thermal ablation of the tumor.

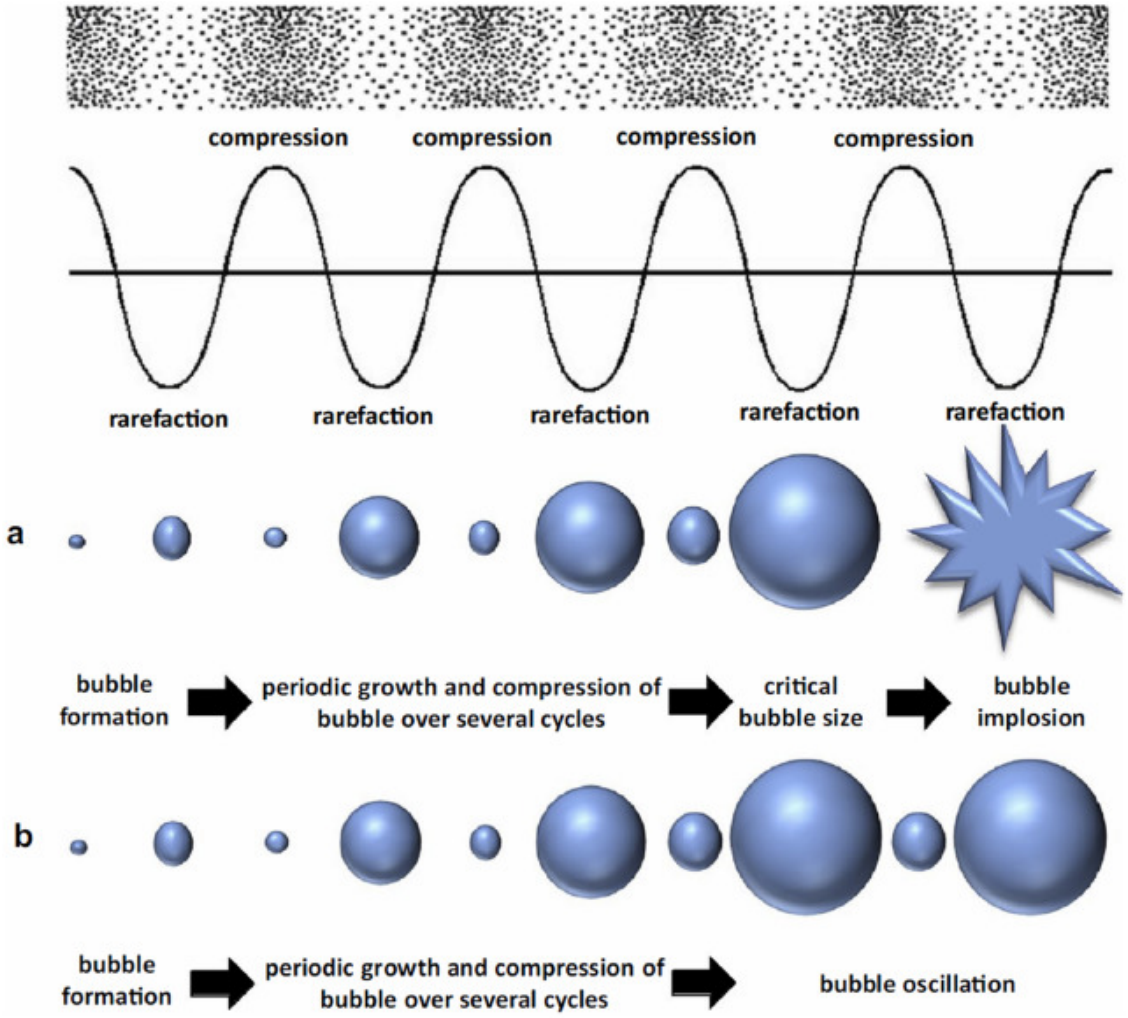

Figure 2.8: Acoustic cavitation mechanism: (a) Transient cavitation. (b) Stable cavitation. [33]

On the other hand, the non-thermal effects rely on various phenomena as the acoustic cavitation, microjets, microstreams formation and radiation forces. These processes depend on the interaction between US waves and gas bubbles, usually trapped in fluids inside the tissues. When an US wave is applied, the dimension of the gas bubbles starts to oscillate following the compression and decompression cycles of US, as shown in Figure 2.8. If these oscillations in their size occur around an equilibrium dimension, the phenomenon is called *non-inertial or stable cavitation*, that generates fluid streaming and mixing of the medium. Differently, if the oscillations lead to the rapid growth of the bubbles, and, after many

cycles they reach a critical size and violently collapse, the mechanism is called *inertial or transient cavitation*. When the bubbles implode, a great amount of energy is released due to the extremely high temperature (above 5000 K) and pressure (higher than 800 atm) reached inside the cavity, at their interface ROS are produced and intense shear forces are generated in the surrounding media.
There are mainly four effects related to the acoustic cavitation phenomenon: the sonoluminescence (SL) that induces extremely short flashes of light of about 100 ps, the pyrolysis of water, the generation of reactive oxygen species and shear forces in the liquid medium. In relation to the biological application, the ROS and shear forces generation can be employed to impart a damage to a living cell, causing lipid peroxidation, DNA damages, breakage of cell compartment and cell membrane and possibly leading to cell death.

The reason behind the sonoluminescence (SL) is not yet totally clear as different mechanisms can participate to the phenomenon. Mainly, this process relies on two elements: the first one is the emission from several molecules and atoms, such as CO (having an high dissociation energy and providing emission in the ultraviolet range), CO_2, N_2O, NO, NO_2, contributing to the continuum emission of the sonoluminescence phenomenon [34]. The second one is the presence of inert noble gases inside the bubbles, such as argon and xenon, that ionize due to the high pressure and temperatures released during the bubble collapse. Then, the free electrons generated by the ionized gas atoms interact with the surrounding neutral atoms, producing the Bremsstrahlung radiation. This process occurs when a highly energetic electron approaches an other charged particle, such as an ion or an other electron, while following its trajectory. Due to the attractive or repulsive forces depending on the sign of the charge, its trajectory is deflected and the electron undergoes a deceleration. For the conservation of energy, the decrease in the kinetic energy of the electron is compensated by the emission of photons, thus producing a radiation.

Another consequence of the acoustic cavitation phenomenon is the pyrolysis of molecules inside the bubbles, involving gases dissolved in the liquid and vapors of the liquid [35]. If the gas/vapor is characterized by an high heat conductivity, the heat produced by the collapse of a gas bubble is quickly carried away from the bubble interior, providing the heating of a shell of liquid close to the bubble. The high temperatures in this hot region cause the pyrolysis of molecules at the bubble/liquid interface, producing radicals such as ·H and ·OH in aqueous solutions:

$$H_2O \rightarrow \cdot H + \cdot OH \tag{2.7}$$

Then, these radicals tends to react with other molecules in the bulk of the solution, forming ROS.

These phenomena are included in the sonochemical effects produced by acoustic cavitation, which are based on a cascade of chemical reactions, leading to the final formation of radicals and ROS, in particular singlet oxygen.

In parallel to these effects, a mechanical damage is caused to the tumor cells as a consequence of the gas bubbles collapse. In fact, several forces of different strength such as shear stresses, microjets, acoustic streaming and violent shock waves [31] can cause various phenomena, from the mere displacement of ions and molecules resulting in a change in the biological environment surrounding the cells, to great physical injuries to the cell membranes, leading also to their perforation in some cases, and damages to intracellular components. Therefore, the mechanical stress applied to the cells membranes seems to generate membrane wounds, responsible for an enhanced permeability and pore formation, that facilitate the influx of Ca^{2+} inside the cells, leading to an increased production of ROS in the intracellular environment and thus, to cell apoptosis.

Synergistic effect of acoustic cavitation and NPs

Both organic and inorganic sonosensitizers are involved in the sonodynamic therapy process, providing an enhancement of the acoustic cavitation effects by lowering the cavitation threshold, defined as the minimum US intensity able to induce the cavitation phenomenon. While in early SDT studies, the majority of sonosensitizers were organic molecules as porphorins and chlorins, the same used for photodynamic therapy, in recent experiments nanoparticles have shown a great potential. In fact, the organic sonosensitizing agents are affected by some issues as the hydrophobicity, that tends to aggregate them in physiological environment, the possible toxicity of some molecules and the low selectivity to cancer tissues, that can result in the damage of healthy cells.
Differently, thanks to the large surface area of nanoparticles, they can be properly functionalized improving biocompatibility, biodistribution and selectivity to cancer tissues [31].

The first beneficial effect of nanoparticles relies on their ability to trap gas bubbles on their surface thanks to the particular size, surface characteristics and chemistry, thus increasing the number of acoustic cavitation nuclei. With an higher amount of nuclei, the probability of cavitating gas bubbles is enhanced, leading to an intensified cavitation phenomenon which produces more ROS, responsible for cellular toxicity.

Another advantage is based on the possibility to increase ROS generation related to the sonoluminescence process. Actually, the sonosensitizers (both organic or inorganic) absorb the sonoluminescent light passing to an excited state that, similarly to the photodynamic therapy, generates electron-hole pairs. These excited charges, in turn, interact with oxygen

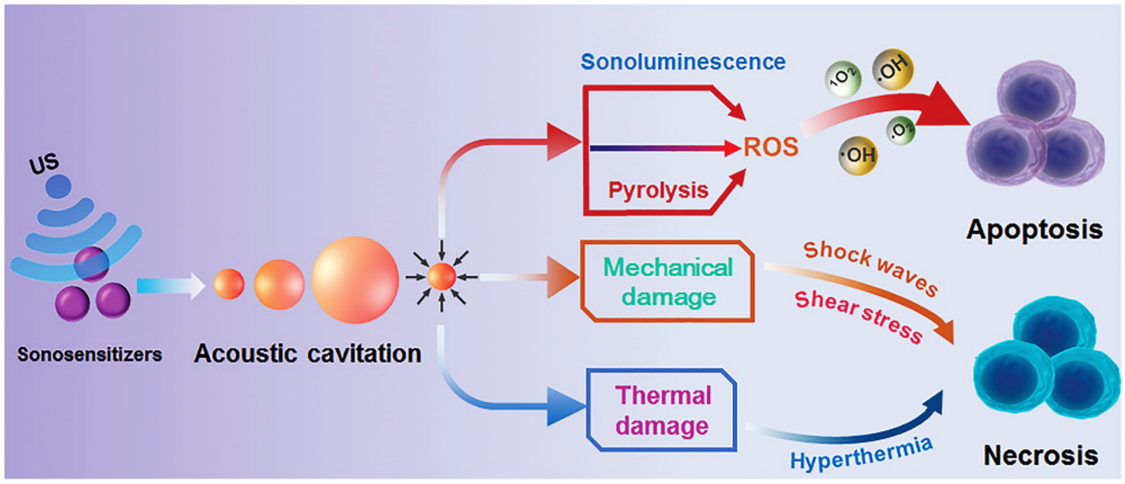

Figure 2.9: Sonodynamic therapy mechanism [30].

molecules and other biomolecules, producing singlet oxygen and ROS.

Furthermore, NPs can contribute to the physical perforation and disruption of cells membranes, especially in the case of inorganic NPs, such as Au, ZnO and TiO_2. In fact, the presence of edges and sharp elements facilitate the mechanical abrasion and injury to the cells membranes when NPs are moved due to the cavitation phenomenon, thus increasing the cytotoxic effect.

To conclude, the NPs belonging to the class of semiconductors have the unique ability to produce ROS thanks to their particular crystal structure. As an example, ZnO is a semiconducting material having a quite large energy gap of 3.7 eV, thus the excitation of electrons from the valence to the conduction band is possible only if a sufficient energy from an external source is provided. However, thanks to the nanometric scale of ZnO nanocrystals, electrons can be promoted to excited states even in the absence of an external stimulus. Then, in systems at macro or microscale, electrons and holes tend to quickly recombine; differently, in nanoparticles, they move towards the surface and start to interact with the absorbed species. In this context, while holes are responsible for the dissociation of water molecules into hydrogen (·H) and hydroxyl radicals (·OH), acting as strong oxidant agents, electrons work as reducer agents, reacting with the adsorbed oxygen molecules, forming superoxide radical anions (O_2^-). In turn, O_2^- can react with hydrogen, generating HO_2^- and then, after the interaction with oxygen, H_2O_2 is formed in a cascade of reactions that leads to the production of all these different ROS [36].
This intrinsic mechanism can be easily enhanced with the application of an external US

stimulus, providing an increment in the oxidative stress to the tumor cells.

Finally, since ZnO nanocrystals are employed in the experiments carried on during the thesis work, a particular attention should be payed also to another characteristic of these NPs that concerns their ability to release zinc ions.
In fact, zinc plays an important role inside the cells as it takes part in the synthesis of various mammalian proteins or also it can be directly a component of proteins, such as DNA-binding proteins or proteins involved in DNA repair. Therefore, it regulates the transcription function, the antioxidant defence and the DNA repair inside the cells [37].
Consequently, while on the one hand the presence of dissolved zinc ions in the extracellular environment seems to contribute poorly to the cytotoxicity, and even it appears to form zinc-carbonate phosphate precipitates that protect the cell membranes from the toxic effects of zinc, on the other hand the formation of intracellular zinc ions greatly increases the cytotoxicity. This higher amount of Zn^{2+} inside the cells causes an imbalance in normal protein activity, resulting in several issues concerning DNA repair, oxidative stress, mitohcondrial-driven apoptosis [36].

Cytotoxic effects of ROS

In general, in normal cell activity, Reactive Oxygen Species are produced during the reduction of molecular oxygen to water, a particular process that occurs in mitochondria for the synthesis of ATP, an organic molecule which represent the main source of energy in cells [38]. In fact, due to the presence of two unpaired electrons in different orbitals and with the same spin, the oxygen molecule (O_2) can easily undergo reduction processes, forming radical species if oxygen is not completely reduced. Therefore, with the transfer of a single electron, it produces superoxide anion (O_2^-), that, in turn, can generate hydrogen peroxyde (H_2O_2) by losing an electron and reacting with hydrogen. Finally, hydroxyl radicals ($HO\cdot$) are formed, characterized by a high reducing potential and provide low activation energies for the reaction mechanisms [21]. As a consequence, ROS are intrinsic byproducts of the metabolic activity of cells and are involved in signaling processes, mitochondria working mechanism and mitogenic response [38].
The presence of intracellular ROS, that are oxidant species which "steal" electrons from the surrounding environment (proteins, lipids...), is properly counterbalanced by antioxidants, that are reducing agents, able to donate electrons or hydrogen atoms, which represent the only defense against an high amount of ROS.

However, an intense production of ROS, induced for example by SDT, can lead to oxidative stress, altering the balance between oxidant and antioxidant species inside the cells. This phenomenon causes a distortion in normal cell functions due to the aggressive

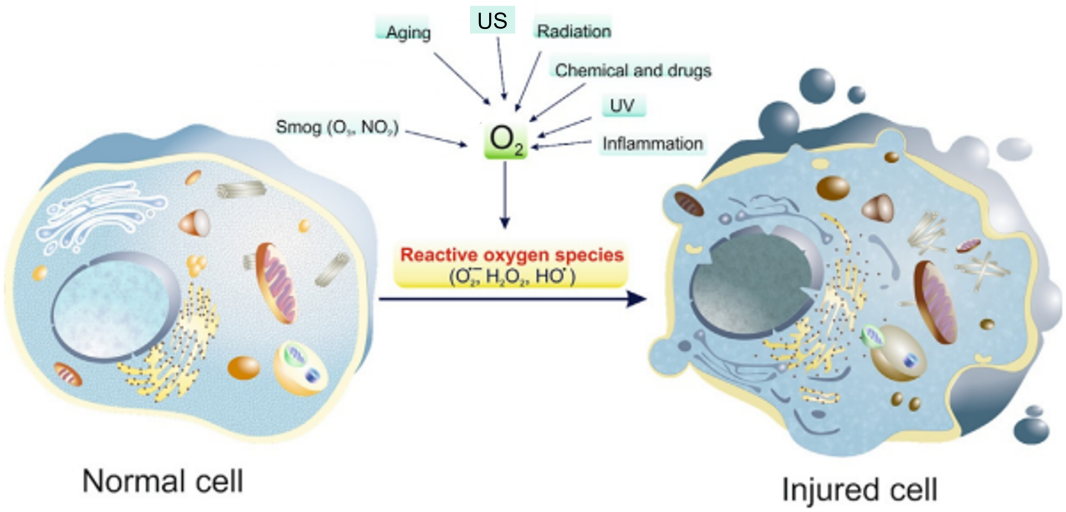

Figure 2.10: Consequence of Reactive Oxygen Species [21].

nature of ROS, with hydroxyl radicals above all. Several consequences are induced by this mechanism such as the oxidative modification of proteins, leading to their denaturation and impeding their catalytic function, the alterations in nucleic acids, the inhibition of DNA repair mechanisms due to the degradation of proteins and consequent DNA damage, and the lipid peroxidation, a process that consists in the oxidative degradation of lipids due to the transfer of electrons from lipids to ROS, resulting in cell membrane damage. In turn, this last issue leads to alteration of the transport functions, of cell signaling mechanisms and also of receptor functions.
The sum of all these damages may result in cell death (Figure 2.11), following different paths depending on the injury and on the type of cell [21], [39]:

1. **Apoptosis** is a direct cell death mechanism that belongs to the "Programmed cell death" processes, meaning that it is genetically controlled. Since this "programmed" death restricts the number of cells, eliminating the dysfuntional ones, apoptosis mechanism is suppressed in tumors, causing its proliferation and growth.
   The main evidence of an ongoing apoptosis mechanism is the decrease in the cell and nucleus dimensions, DNA fragmentation, the formation of blebs on the membrane and the presence of apoptotic bodies. A crucial role in apoptosis is played by caspases, a particular group of proteases able to attack and cleaves specific target proteins as a response of particular apoptotic signal. The death can occur following two different pathways: the death-receptor and the mitochondrial paths. The first one starts when species of the tumor necrosis factor (TNF) family, released by the immune system cells (e.g. macrophages) to activate an immune response, bind to the death receptors

on the surface of the cells. Upon binding, a signaling cascade is induced inside the cell, leading to the final cell death.
On the other hand, the mitochondrial pathway begins when an high level of intracellular ROS produces lipid peroxidation, leading to the depolarization of the mitochondrial membrane potential and enhancing its permeability [40]. This damage to the membrane is the responsible for the release of cytochrome c (Cyt c), a pro-apoptotic protein, from the mithocondria to the cytoplasm of the cell providing the activation of caspases cascade leading to the cell death.

2. **Necrosis**, differently from apoptosis, is characterized by the swelling, loss of integrity and rupture of cell membranes with consequent increased permeability, leakage of intracellular moieties and influx of extracellular ions. The main responsible for necrosis are a high amount of intracellular ROS, the presence of Ca^{2+} and the action of poly–ADP–ribose polymerase (PARP). In particular, this last contribution comes from an enzyme, PARP, that employes the ATP supplies inside the cells to catalyze the DNA repair during cell injury. This process causes extremely low levels of ATP, that represents the main difference between apoptosis, in which PARP is inactivated, and necrosis. The synergistic action of ROS and low level of ATP causes an increase in membrane permeability, allowing Ca^{2+} to enter within the cell and activate proteases, responsible for the degradation of proteins, leading to the final cell lysis.
Furthermore, when a cell dies due to necrosis, since the cell constituents are released in the surrounding environment due to the damaged membrane, they can enter in the circulation and trigger an immune response. Finally, necrosis can also be activated by an high concentration of TNF.

3. **Autophagy-associated cell death** is suggested to be another type of "programmed cell death" mechanism that occurs as a consequence of cell starvation. In this context, the cell tends to digest its own macromolecules and constituents to produce energy and survive. Therefore, ROS, especially H_2O_2, are produced to generate an oxidative condition favouring the formation of autophagosomes: these are double-membrane structures responsible for the confinement of the constituents. Then, autophagosomes undergoes a fusion process with lysosomes and the digestion of organelles and proteins occurs.
However, autophagy is a mechanism arising from other cell death processes, thus it is not a specific cell death mechanism.

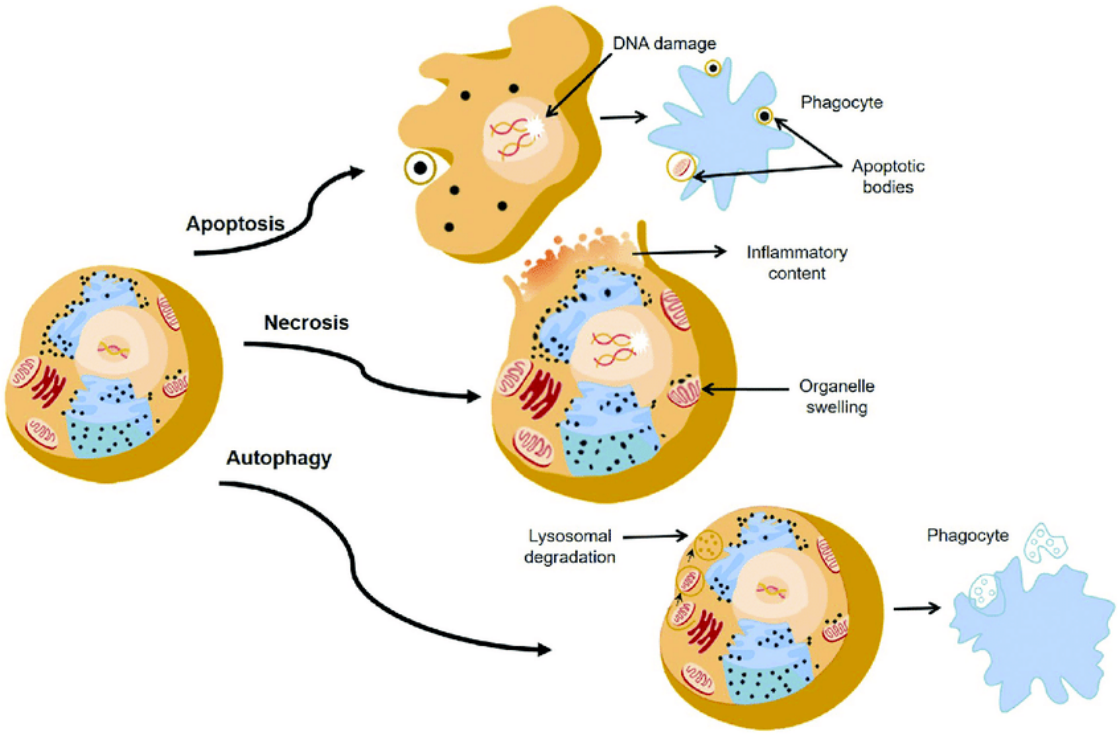

Figure 2.11: Three different pathways for cell death [41].

2.2 Materials and methods

This section of the Thesis provides a complete overview on the approach and methodology employed behind the two techniques for the ROS generation detection, Luminol sonochemiluminescence and EPR spectroscopy, starting from the description of the synthesis, functionalization and characterization of amino-functionalized ZnO nanocrystals.

It should be underlined that all the experiments, both relying on Luminol and EPR techniques are carried on using always the same medical device for the US excitation of the sample, namely LipoZero G39 (GLOBUS), able to generate unfocused US waves and commercially available especially for aesthetic treatments, as liporeduction and cutaneous flow. As shown in Figure 2.12, it is composed of two parts: a main body where it is possible to select the US wave characteristics, such as frequency, duty cycle and power, and an US transducer with circular surface area, upon which is always poured a thin layer of gel before the positioning of the sample. This is done in order to ensure the proper impedance coupling between the transducer's surface and the well, preventing the presence of air in between that can reflect the incoming acoustic wave, decreasing the effective US intensity

in the sonicated solution.

Figure 2.12: LipoZero G39 (GLOBUS) medical device.

2.2.1 ZnO−NH_2 synthesis, functionalization and characterization

ZnO nanocrystals are synthesized through a novel approach developed by Garino et al. [42], relying on a fast, highly-reproducible and efficient microwave-assisted synthesis method [43], [44].

Firstly, zinc acetate di-hydrate ($Zn(CH_3COO)_2 \cdot 2H_2O$ Puriss. p.a., ACS Reagent, $\geq$ 99.0% Fluka), chosen as zinc precursor and consisting in a fine white powder kept under vacuum condition since it easily reacts with water, is weighted and dissolved in methanol to obtain a concentration 0.09 M. Then, this opaque white solution is directly stirred in the Teflon reactor vessel, with the addition of double-distilled water, leading to a completely transparent solution. Also a potassium hydroxide solution (KOH $\geq$ 85% pellets, Sigma-Aldrich) composed of KOH dissolved in methanol with a concentration 0.02 M, is introduced inside the vessel, whose temperature and pressure are constantly controlled with specific probes. The final solution is then inserted in a microwave oven for 30 min at $60°C$. The reaction leading to the formation of ZnO nanocrystals relies on the hydrolysis of the zinc precursor induced by the presence of the hydroxide inside the solution. After that, the solution is cooled down at room temperature and centrifuged for 10 min at 3500 g so that the NPs precipitate and it is possible to remove the solvent and the unreacted compounds. This procedure is carried on twice to completely replace the solvent with ethanol (Sigma-Aldrich, 99%). Finally, ZnO nanocrystals are dispersed homogeneously through US sonication.

Then, the ZnO NCs are functionalized with amino-propyl groups to obtain ZnO-NH_2 nanoparticles.
The desired quantity of ZnO nanocrystals dispersed in ethanol are drawn and inserted in a round glass flask, heated up to $80°C$ and subjected to stirring and nitrogen gas flow. To provide the NCs functionalization, 3-aminopropyltrimethoxysilane ($H_2N(CH_2)_3Si(OCH_3)_3$ APTMS 97%, Sigma Aldrich) is introduced to the solution at 10 mol% of the total ZnO amount. After 6 hours, two washing steps are performed through centrifugation (10 min, 10000 g) to remove all the unreacted APTMS and replacing it with ethanol.

XRD (X-ray diffraction) is used characterize and analyse the final crystalline structure of the ZnO-NH_2 NCs. In this technique, some drops of the NCs colloidal suspension are placed on a small silicon wafer and they are left to dry at room temperature. The XRD employs a Panalytical X'Pert diffractometer in $\theta - 2\theta$ Bragg-Brentano configuration, having a radiation source of Cu-Kα, with $\lambda = 1.54$ Å, 40 kV and 30 mA).

Furthermore, High Resolution Transmission Electron Microscopy (HRTEM) is used to analyse the morphological features of the NCs. The employed equipment includes a a FEI Titan ST microscope, providing an acceleration voltage of 300 kV, and equipped with h a S-Twin objective lens an ultra-bright field emission electron source (X-FEG) and a Gatan 2k $\times$ 2k CCD camera. The imaging is obtained by depositing a drop of the samples (NCs diluted in ethanol with a concentration of 100 $\mu g/mL$) on a holey carbon copper grid and left to dry overnight.

Finally, the particles size and Z-potential value of ZnO-NH_2 NCs in water suspension was determined through the Dynamic Light Scattering (DLS) technique (Zetasizer Nano ZS90, Malvern).

2.2.2 Luminol sonochemiluminescence

The sonochemiluminescence provided by Luminol molecules is the first method employed in the experiments for a rapid analysis over a large range of sonication power and time combinations to find the most effective conditions for the cells treatment.
As previously mentioned, the sonoluminescence is one of the several effects generated by the acoustic cavitation, consisting in the emission of flash of light due to different mechanisms, as the recombination of free radicals and the Bremsstrahlung radiation. However, due to the relative difficulty to detect the sonoluminescence process in water, which lasts few picoseconds, specific molecules can be introduced in the solution to enhance the SL process, known as sonochemiluminescence (SCL) [45].

Therefore, the SCL experiments rely on the detection of a blue luminescence ($\nu = 430$ nm), produced by Luminol molecules when reacting with the radicals sono-generated during the cavitation (·OH in particular for its high reduction potential) [44]. Futhermore, even if Luminol has no efficient chemiluminescent characteristics, it produces light when properly mixed with oxidizing agents, such as H_2O_2 and O_2 [46].

As shown in Figure 2.13, a complex pathway consisting on a cascade of chemical reactions is responsible for the emission of light. Starting from the Luminol molecule, at first it oxidizes and deprotonates, forming the associated monoanion (**I**) that, in turn, oxidizes (i) by HO· producing the diazaquinone radical anion (**II**). Then, the reaction of **II** with O_2^- (ii) generates the hydroperoxide addition product (**III**) which that can follow two different paths: its neutral form may return to the starting material producing also O_2 through a dark reaction (iv) or its monoanion form can decompose (iii) to give the exited state of the aminophthalate monoanion (**IV**). When **IV** relaxes to its ground state, then light in the blue visible range is emitted [46], [47].

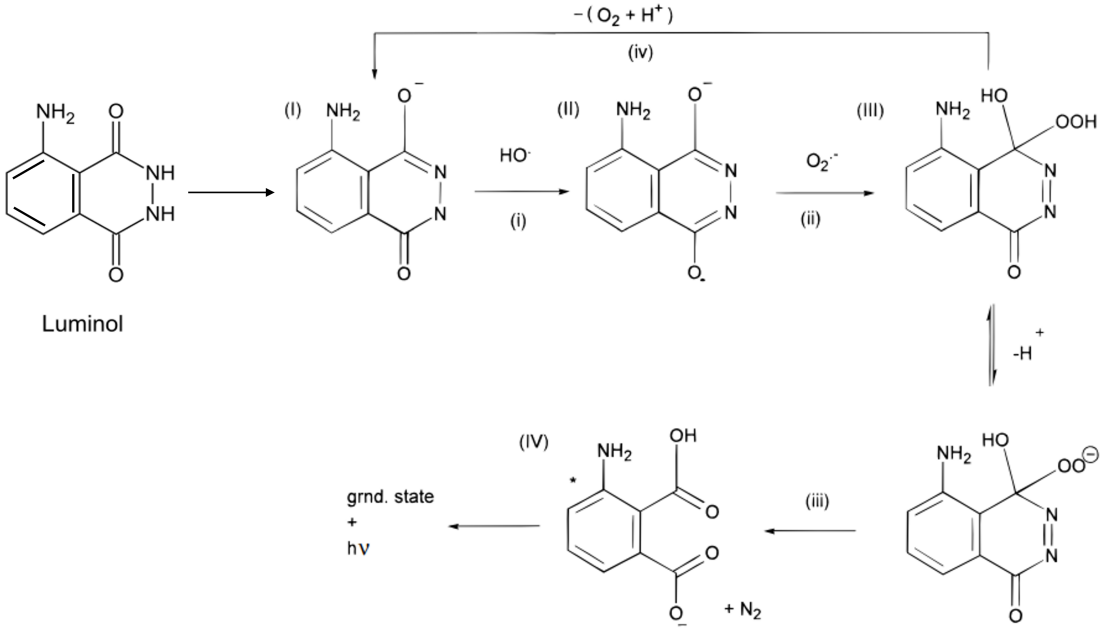

Figure 2.13: Cascade of reaction responsible for Luminol sonochemiluminescence (adapted from [47]).

Prior to the beginning of the experiments, two reservoir solutions used to store specific constituents at particular concentrations are prepared: the first one contains sodium hydroxide, NaOH, weighted (3.999 g) and dissolved in double-distilled water up to 1 L

of solution, obtaining a final molarity 0.1 M. The second reservoir is composed of H_2O_2, drawn from the original storage package from Sigma-Aldrich at 30% v/v and diluted in 30 mL of double-distilled water, leading to a concentration 0.02 M.

Therefore, to ensure a proper activation of the SCL process, Luminol 97% (80 mM), purchased from Sigma-Aldrich, is introduced in a water-based solution composed of hydrogen peroxide, H_2O_2 with molarity $5{\cdot}10^{-4}$ M, drawn from the 30 mL reservoir Falcon having molarity 0.02 M, and sodium hydroxide, NaOH, extracted from the reservoir in which it has a concentration 0.1 M. For the production of the control solution, the Luminol powder, stored in the fridge at 4 $°C$, is weighted and inserted inside a Falcon, properly covered with a sheet of alumina so to keep the solution in a dark environment. Then, to provide the effective and homogeneous dispersion of Luminol powder inside the solution, the Falcon is firstly agitated and then immersed in a sonicating bath for few minutes, $1 - 2$ min.
The same procedure and concentrations are employed in the preparation of the solution containing the nanoparticles, with the addition of amino-propyl functionalized ZnO nanocrystals having a concentration of 200 $\mu g/mL$ in the final solution.

Since the main purpose of these experiments is to find the conditions in which the ultrasound excitation and the nanoparticles are separately safe for the cells, without providing any damage, but their synergistic action becomes detrimental for the CTCL, the results obtained with the control solution are always compared to the effects of the nanoparticles-enriched solution. In fact, as NPs are responsible for an enhancement of the SCL phenomenon, thanks to their ability to provide further nucleation sites for cavitating bubbles and, consequently, an higher amount of ROS produced, the analysis is focused on how much greater is this improvement of SCL.

Afterwards, 2 mL of the prepared solution are inserted in a single well of a 24 well-plate. The well is positioned in the central part of the Lipozero G39 (GLOBUS) transducer by placing a thin layer of gel in between to ensure the acoustic impedance coupling (Fig. 2.14). In order to obtain the darkest environment possible, the experiments are held in a optics laboratory, with the possibility to use proper curtains to prevent the light from passing through the windows. Furthermore, the transducer is placed in a box, employed specifically for this aim (Figure 2.15).

Figure 2.14: Positioning of a single well of a 24 well-plate on the transducer.

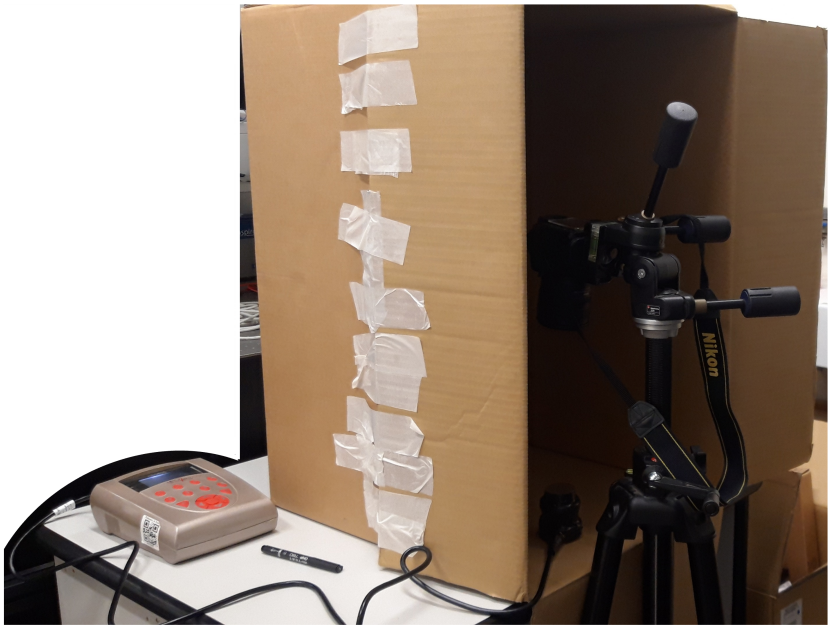

Figure 2.15: Set-up used for Luminol sonochemiluminescence experiments.

The Lipozero G39 is positioned outside the box and it is set with the following sonication characteristics:

1. **Frequency** = 1 MHz
2. **Duty Cycle (DC)** = 100%
3. **Sonication conditions for single well of a 24 well-plate**:
   (a) High powers: 60%, 80%, 100%.
   Short sonication times: 5s, 10s, 15s, 30s.
   (b) Low powers: 10%, 15%, 20%, 25%, 30%.
   Long sonication times: 30s, 1min, 2min, 3min.

In Table 2.2 are presented the US intensities associated to the different power percentages.

Power, %	**Power, W/cm^2**
100	3
80	2.4
60	1.8
30	0.9
25	0.75
20	0.6
15	0.45
10	0.3

Table 2.2: Conversion of the ultrasound power from percentage to W/cm^2.

The blue light produced by SCL during the sonication of the solution is captured by using a digital camera Nikon D80 model with long exposure time, depending on the sonication time, and the specific manual setting: ISO 1250 and Bulb f/4. The video camera is fixed on a tripod and positioned right above the well, partially inside the box. Thus, the images are acquired in a dark environment, showing a visible circle of blue light corresponding to the well shape. Before each experiment, a frame image is taken in absence of sonication so that the final SCL mean value intensity is found by subtracting the frame image to the acquired one.
Therefore, upon the acquisition of the images related to the sonication process, they are processed using the open source Image J software. First of all, a math subtraction of the background in a pixel-by-pixel approach is performed (Fig. 2.16a), as to remove both the thermal noise of the camera and the light captured from the environment caused by the long exposure times [45].
Secondly, the area of the acquired image that corresponds to the upper part of the well and follows its circular perimeter is properly selected through a circular or a rectangular shape,

depending on the needs, called Region Of Interest (ROI). The blue intensity associated to each image is obtained by considering that each pixel in the image is described by an intensity value, ranging from $0 - 255$ (with 2^8 bits) for each of the three different colors: Red (R), Green (G) and Blue (B).
The circular ROI (Fig. 2.16b) is employed to find the average intensity value of blue (Fig. 2.16d) inside the selected region. Differently, the rectangular ROI (Fig. 2.16c) permits to calculate the mean intensity value for each vertical line of pixels and for each type of color, thus resulting in a RGB profile plot along the diameter of the well (Fig. 2.16e). However, since the blue intensity is of interest, only the data related to "B" are stored and plotted using Origin software.

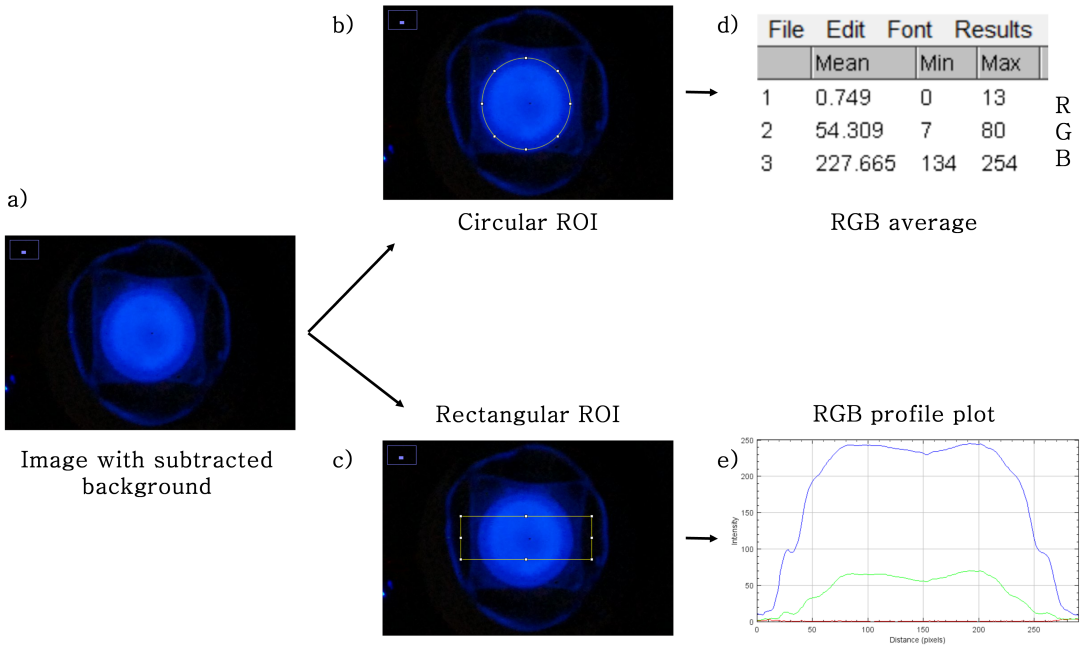

Figure 2.16: Image processing using Image J.

2.2.3 Electron Paramagnetic Resonance (EPR) Spectroscopy

Once the study over the many possible sonication conditions is performed, some most relevant cases, particularly involving low powers, are further examined to obtain more quantitative results on the amount of ROS generated upon sonication by employing the Electron Paramagnetic Resonance (EPR) Spectroscopy technique (EMXNano X-Band spectrometer from Bruker).

EPR is a spectroscopic technique that relies on the absorption of an electromagnetic radiation to study paramagnetic samples, thus species having unpaired electrons [48], [49]. The main principle behind the EPR spectroscopy is the Zeeman effect, arising upon the interaction of these unpaired electrons with a magnetic field generated by the EPR equipment. In fact, electrons are characterized by an intrinsic angular momentum, also known as spin, $s = \frac{1}{2}$, at which is associated a magnetic moment (μ). Since the description of the spin belongs to the quantum mechanics field, it is possible to know only its modulus and the projection of the angular momentum on one axis. Electrons can "spin" on one of the two directions of the axis and, depending on its orientation, the spin quantum number (m_s) can assume two values: $m_s = +\frac{1}{2}$ or $m_s = -\frac{1}{2}$, each one related to a magnetic moment [50].
Therefore, in absence of a magnetic field, the two energy states of an electron, related to the two different spin quantum numbers, are degenerate and corresponds to a unique energy level.
Differently, when a magnetic field B_0 is applied (Fig. 2.17), it induces the splitting of the two possible energy states, labelled $m_s = -\frac{1}{2}$ if the magnetic moment is aligned in parallel with the magnetic field, and $m_s = +\frac{1}{2}$ if the spin is in an antiparallel configuration; this phenomenon is called Zeeman effect. In this condition, an electron may switch between the two levels, changing sign of the spin, by absorbing or emitting a certain energy $h\nu$ corresponding to the energy difference between the two levels.
The energy levels are described by the fundamental equation for EPR:

$$E = g_e \mu_B m_s B_0 = \pm \frac{1}{2} g_e \mu_B B_0 \tag{2.8}$$

and

$$\Delta E = h\nu = g_e \mu_B B_0 \tag{2.9}$$

is the energy difference between them. In the above expressions, g_e is called the g-factor, a constant that depends on the nature of the radical and for electrons it is equal to $g = 2.0023$, μ_B is the Bohr magneton, the natural unit of electronic magnetic moment, ν is the frequency and h is the Plank's constant.

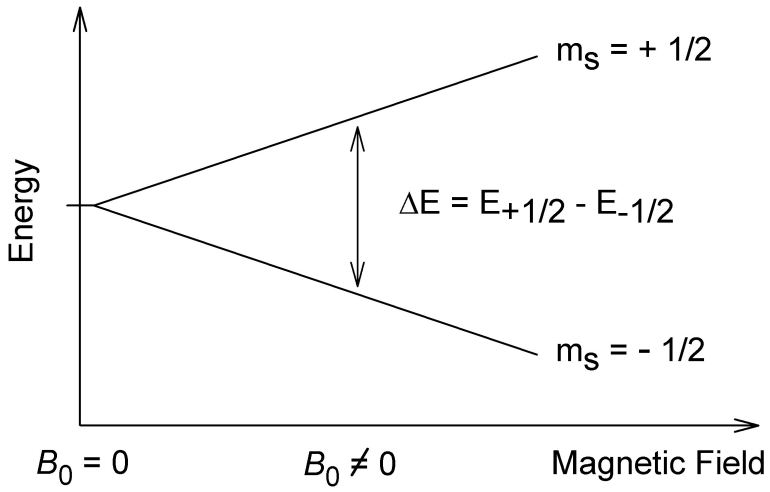

Figure 2.17: Zeeman effect machanism.

Therefore, the working mechanism involves a constant electromagnetic radiation, usually in the range of microwaves, which is applied to provide a specific energy $h\nu$ to the system, and a magnetic field, whose frequency is scanned over a wide range of values. Since the energies of the two states depend linearly on B_0, as the frequency increases, also the energy difference between them is raised, until it reaches the same value of the radiation energy. In this stage, the radiation is absorbed, and the unpaired electron switches to the higher state, inverting also its spin.
As a consequence, EPR is a technique completely specific for radicals since, if there are no radicals or unpaired electrons in the sample, the absorption cannot occur [48].

Furthermore, the absorption peaks obtained in the final spectrum strictly depend on several factors such as the nature of the radical (generating different lines for each specific radical species), its surrounding environment and its structure. Actually, the interactions of the unpaired electrons with the nearby magnetic nuclei (known as hyperfine couplings) provide characteristic spectra, with a definite pattern of lines [48], [49].

Since radicals are extremely reactive species, they tend to decay in a very short time, usually ranging from hundreds of picoseconds to few nanoseconds, hindering the possible detection from the EPR equipment. Hence, to prevent the extremely rapid decay, spin traps need to be employed in this technique to stabilize the ROS, in particular the hydroxyl radical. Spin traps are particular chemicals able to establish covalent bonds with the radical species, allowing for the formation of more stable compounds, called spin adducts, having

a longer half-life, of the order of minutes or even hours [51], that makes them detectable by the EPR equipment. Another property of spin traps is that they have the same number of unpaired electrons, so that they corresponds to the effective number of reactive radicals in the sample.
The most popular spin trap molecule is the 5,5-dimethyl-L-pyrroline N-oxide (DMPO) used specifically for the detection of hydroxyl radical, as shown in Figure 2.18, since OH· is the main reactive species of interest produced during the sonication mechanism.

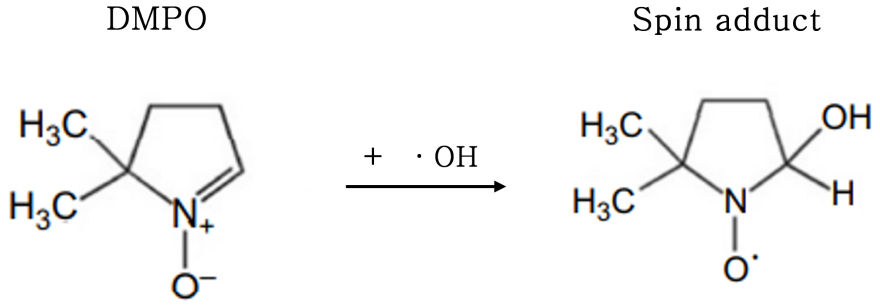

Figure 2.18: Structure of the spin trap molecule DMPO (right) and of the spin adduct after the reaction with OH· radicals (left).

The final spectrum obtained is the first derivative of the absorption peaks and is characterized by a certain number of lines that depends on the hyperfine couplings and thus on the interactions of the unpaired electron with the surrounding nuclei, following the expression:

$$Number\ of\ lines = 2nI + 1 \tag{2.10}$$

where n is the number of nuclei involved and I their nuclear spin.
In the case of DMPO-OH, the EPR spectrum is composed by four lines (Fig. 2.19), resulting from the hyperfine interactions with nitrogen ^{14}N, having I=1, and ^{1}H atom with I=1/2. As a consequence, three lines derive from the nitrogen atom and then, each of them split in two lines due to the presence of the hydrogen atom. At the end, the two central lines are higher due to the superposition of lines during the splitting, while the two lateral ones remain lower, giving a 1:2:2:1 final spectrum configuration [52].

The DMPO-OH spectra is acquired and processed through the Xenon software (Bruker), providing also the SpinFit feature for the fitting (Fig. 2.19) and simulation of the spectrum that calculates the double integral and thus the area below the four peaks. Combined with

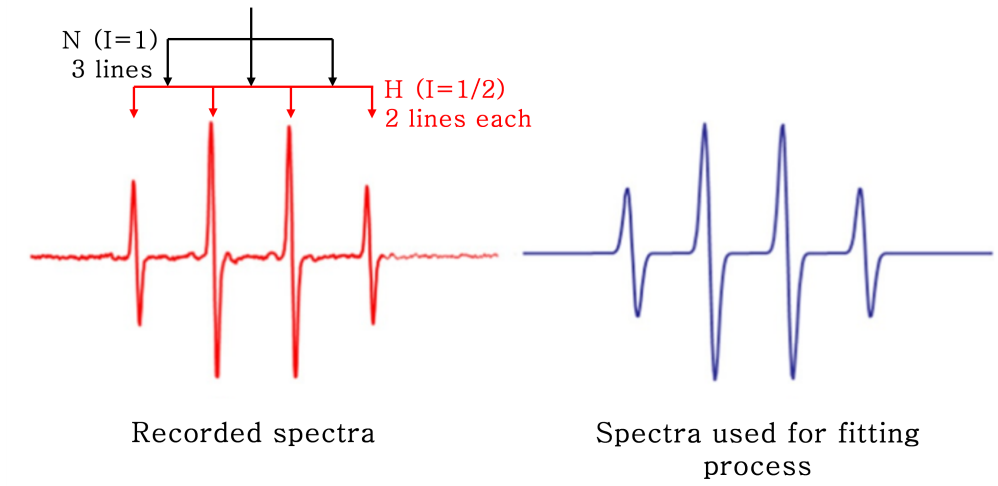

Figure 2.19: DMPO EPR spectra and the related lines (left) and simulated spectra for the fitting process (right). (adaptation of [21]).

the spin counting module, the double integral is converted into the number of spins for each species, in this case for DMPO-OH adducts [53].
In fact, the area below the acquired spectrum is related to the malr concentration of DMPO-OH adducts, which, in turn, corresponds to the amount of hydroxyl radicals inside the sample.
Finally, null molar concentration and area are considered for spectra not having the correct trend: spectra showing additional lines or, more in general, not exhibiting the characteristics four peaks of DMPO-OH.

The EPR experiments are carried on by employing the same solutions volumes already used in the case of Luminol experiments, allowing for a comparison between the two methods. Therefore, 2 mL of solution are introduced in a single well of a 24 well-plate.

To provide the spin trapping mechanism, 10 μL of DMPO by Sigma, with a concentration of 1% v/v, are collected and diluted in 990 μL of double-distilled water in a Eppendorf used as reservoir, obtaining a concentration of 10 $\mu L/mL$. Since DMPO is a light-sensitive compound, the Eppendorf is covered with an aluminum sheet and stored in the refrigerator at -20 $°C$. Then, right before each experiment, the Eppendorf reservoir is defrosted for some minutes to collect the proper amount of DMPO. At the end, the control solution (without NCs) is prepared directly inside the single well of a 24-well plate by withdrawing 200 μL of DMPO from the previously prepared Eppendorf reservoir and diluting them in

1800 µL of double-distilled water, obtaining a final concentration of 100 µL/mL.

To evaluate the effect of nanoparticles in the ROS generation, ZnO-NH_2 nanocrystals, with a concentration of 200 µg/mL, are added in the solution just described, producing the nanoparticles-enriched solution. Since ZnO-NH_2 nanocrystals are stored in an ethanol solution with a concentration of 5.9 mg/mL, a proper amount is firstly withdrawn from this original solution and inserted in an Eppendorf, used as reservoir. Then, three cycles of centrifugation and washing with water (5 min , 1000 RFC) are performed in order to remove the ethanol from the solution and disperse the NPs in a final double-distilled water solution, with a concentration of 1 mg/mL. After that, the Eppendorf is immersed for few minutes ($2-3$ min) in a sonicating bath to ensure a homogeneous dispersion of NPs. Finally, the solution is left at rest for approximately 30 min before being used.

To resume, the composition of the various solutions are the following:

Single well of a 24 well-plate:

1. Control solution: 2 mL = 1800 µL (water) + 200 µL (DMPO)
2. ZnO-NH_2 solution: 2 mL = 1400 µL (water) + 200 µL (DMPO) + 400 µL (NPs)

As in the previous experiments with Luminol, the single wells are placed at the center of the US transducer, with the addition of the coupling gel in between for impedance coupling. The EPR sonication conditions corresponds to a subset of all the combinations tested with Luminol, and are characterized by:

1. **Frequency** = 1 MHz
2. **Duty Cycle (DC)** = 100%
3. **Sonication conditions for single well of a 24 well-plate**:
   Low powers: 10% and 15%.
   Long sonication times: 30s and 1min.

Immediately after the sonication process, the sample is collected through a quartz microcapillary tube, having a capacity of 50 µL, and inserted in the EPR equipment. Finally, the spectra are acquired setting specific conditions in the Bruker Xenon Software of EPR:

1. **Center field**: 3428 G
2. **Sweep time**: 60 s
3. **Sample g-factor**: 2.00000

4. **Receiver gain**: 60
5. **Number of scans**: 15
6. **Mode**: Manual
7. **Number of points**: 0

At the end of the measurements, the spectra acquired are saved and the resulting molar concentration as well as the area are extrapolated for each sample.

2.2.4 Cell culture and related experiments

The effects of the synergistic action of US excitation and amino-functionalized nanocrystals is analysed on cervical adenocarcinoma KB cell line (ATCC® CCL17TM) grown in Eagle's Minimum Essential Medium (EMEM, Sigma) supplemented with 10% heath inactivated fetal bovine serum (FBS, Sigma), 100 $units/mL$ penicillin and 100 µg/mL streptomycin (Sigma) and maintained at 37°C, 5% CO_2 atmosphere [42], [54].

The three major processes that need to be controlled during the actual experiments are: the cytotoxicity of ZnO-NH_2 concentration, the internalization of NCs inside the cells and, finally, the US cytotoxicity.

Since the main purpose of these experiments is to find the effective combination of US and nanoparticles concentration able to produce a cytotoxic effect only when used in conjunction, the NCs cytotoxicity tests are performed in order to choose a NCs concentration that results to be non-toxic for the cells but at the same time, sufficiently high to provide an effective uptake of the NCs inside the cells. To accomplish this, 1.5×10^3 cells/well are seeded into single plastic wells using 96 well-plates (TC-Treated, Corning) and incubated for 24h at 37 °C, 5% CO_2. Then, the culture medium is replaced with fresh medium containing ZnO-NH_2 at different concentrations (5, 10, 15, 20, 25, 50 µg/mL). The NCs employed are withdrawn from a stock ethanol solution (1 mg/mL), bath sonicated at 40 kHz for 10 min before being added to the culture medium. After 24h of incubation, the cell viability is analysed by introducing 10 µL inside each well of WST-1 cell proliferation assay. The tetrazolium salt (WST-1) is cleaved by cellular enzymes to formazan, chemical compounds able to absorb light at specific wavelengths. Following 2h of incubation, the formazan absorbance is measured at 490 nm by the Multiskan GO microplate spectrophotometer (Thermo Fisher Scientific) using 620 nm as reference. Therefore, the higher is the cell proliferation, the more dynamic is their metabolic activity, leading to an effective internalization of WST-1 by the cells that is converted into formazan, providing an increased absorbance spectra. On the other hand, if the cells are suffering or dying, the absorbance

obtained is lower. The control values, obtained from the cells seeded in medium alone are set at 100% of viability and all the other results are expressed in terms of percentage of the control. Finally, the cell viability is measured after 5, 24, 48, 72 h of incubation with ZnO-NH_2 NCs.

The second process that requires a careful control is the cell internalization of NCs. Initially, 1×10^5 cells/well are plated with a complete culture medium inside a 6-well plate (Corning). After 24 h, the culture medium is replaced with a fresh medium enriched with ZnO-NH_2 nanocrystals labeled with a fluorophore, Atto647-NHS ester dye and having a concentration of 10 $\mu g/mL$. Since the cells themselves normally tends to emit a certain fluorescence signal, a fresh medium without NCs is introduced in a control well where cells are not treated. After waiting for 24 h of incubation, the uptake is tested by washing twice the cells with phosphate buffered saline (PBS), and by trypsinizing and centrifuging them at 130 g for 5 min. Then, the cells are re-suspended in 1 mL of PBS and analysed with the flow cytometer. By setting a flow rate of 0.59 $\mu L/s$, 1×10^4 gated events are considered excluding cellular debris, with low forward scatter (EFC) and side scatter (SSC). The results are obtained in terms of fluorescence positive events, represented by a shift to higher intensities with respect to the control, taken as reference.

At last, the US cytotoxicity should be investigated to choose the proper US intensities that are not harmful for the cells when used alone. For this purpose, control wells, containing cells seeded in a culture medium without NCs, are exposed to different combinations of US power and sonication times. The examined conditions relies on three US power values, 10%, 15% and 20%, tested for various sonication times, 5, 10, 15, 30 s and 1, 2, 3 min.

Since these experiments are intrinsically dependent on biological factors, a huge importance is played by the starting conditions that should be the most equal as possible for all the experiments. For this reason, the KB cells contained in a treated culture flask are trypsinized in order to collect a specific amount of cells, corresponding to 5×10^5 for each single well of a 96-well plate. Then, the cells are introduced in two different Eppendorf: one for the control values and the other for the cells treated with NCs. Thus, all the cells are centrifuged so to replace the culture medium with a fresh one; however, in the case of treated cells, the new introduced medium contains also ZnO-NH_2 nanocrystals. After that, the cells are plated inside the 96-well plate. After 24 h of incubation time, both the control and the cells with NPs are exposed to US by placing the 96-well plate upon the Lipozero transducer head with a thin layer of coupling gel. As soon as the treatment is finished, 2×10^3 cells are seeded in 100 μL of culture medium for the WST-1 proliferation assay. Therefore, at the end, four types of values are obtained: two of them are related to

the cells seeded in culture medium without NCs both exposed and unexposed to US, while the other two values refer to the cells seeded in a culture medium enriched with 10 $\mu g/mL$ of ZnO-NH_2 NCs, both exposed and unexposed to US. As before, the results are reported as percentage of the untreated cells viability.

2.2.5 COMSOL simulations

All the laboratory measurements are validated and supported by acoustic wave simulations, performed to emulate the physical behavior of the experiments and to investigate properly the acoustic wave propagation inside the solutions, both in terms of intensity and pressure. In fact, the knowledge of these parameters allows to predict the probability and strength of cavitation processes in each different sample areas, useful for the comparison with experimental results. For this purpose, the *Pressure Acoustic Frequency domain (acpr)* COMSOL interface, belonging to the COMSOL Acoustic Module, is used to simulate the acoustic wave in a static water-based solution, with definite boundaries corresponding to the wells dimensions.

This interface provides the solution in the frequency domain of the Helmholtz equation, known as the linearly approximated form of the acoustic wave equation for a time-harmonic wave [55]. Since the solution is implemented in terms of frequency, the specific frequency of interest, 1 MHz (the same employed for the experiments) is set in the solving parameters.

In order to reduce the simulation complexity, some assumptions are considered in the description of the system:

1. All the thermoviscous effects are neglected, supposing the system to be adiabatic (no substantial differences were found in the work of Spigarelli et al. [56]) with a fixed temperature equal to the standard ambient one (298.15 K).
2. The fluid is assumed to be homogeneous and isotropic.
3. The US wave has a linear propagation, as considered in Hadi et al. work [57].
4. The presence of cavitating bubbles inside the water-based solution is not simulated [58].

The acoustic wave equation solved during the simulation can be written as follows:

$$\nabla \cdot \Big(-\frac{1}{\rho_c} \nabla p_t - q \Big) - \frac{k_{eq}^2 p_t}{\rho_c} \tag{2.11}$$

where $k_{eq} = \frac{\omega}{c}$ is the wave number with angular frequency $\omega = 2\pi f$, c is the ultrasound propagation velocity in water, ρ_c is the water density, and q is a dipole source, in this case considered to be $q = 0$ since there are no other sources of sound within the system [58]. Lastly, p_t is the sound pressure, described by a time-harmonic variation and by the ambient pressure amplitude (P_A): $p_t = P_A \cos(\omega t)$.

This equation is solved by the software within a properly chosen domain, completely composed of static water and whose boundaries correspond to the characteristic geometry of a single well of a 24 well-plate or of a well of a 96 well-plate. In particular, the water-based solution inside the two wells is implemented by introducing manually all the water parameters in the above equation, as shown in Table 2.3, while the domains dimensions are described by two quantities: the radius of the wells and the solution volume heights. As a consequence, as presented in Figure 2.20, the single well containing 2 mL (24 well-plate) is characterized by a radius, $r = 7.95\ mm$ and height $H = 10.78\ mm$, while the well containing 200 ţL (96 well-plate) has $r = 2.5\ mm$ and $H = 10.19\ mm$. It should be remarked that this solution volume height are lower than the total heights of the two wells.

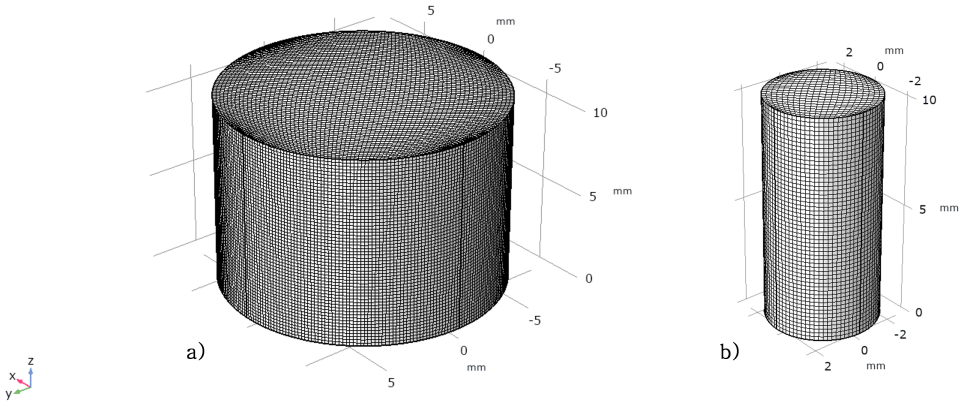

Figure 2.20: Single well part of a 24 well-plate with the characteristic dimensions: radius = 7,95 mm and height = 10,78 mm. b) Single well part of a 96 well-plate with radius = 2,5 mm and height = 10,19 mm.

Figure 2.20 also shows the mesh of the wells, realized by selecting a *Mapped* quadrilateral mesh on a boundary surface and then extending it to the whole domain volume through the *Swept* mesh command. The size of the mesh elements is imposed to be at least greater than $\lambda/10$, but smaller than $\lambda/8$, since 8/10 mesh elements within the acoustic

wavelength are able to provide a sufficiently accurate simulation of the acoustic pressure field.

Since the selected domain is described as an isolated water system, specific conditions should be added to its boundaries in order to simulate the presence of the wells solid material (polysterene) surrounding it, and consequently the behavior of US wave in close proximity to the lateral faces, and the source of the acoustic field, associated to the lower wells surface.

Actually, since the US transducer converts an electrical input into a mechanical displacement of its upper surface, whereon is placed the single well in the experimental measurements, the generation of the acoustic pressure field within the well is simulated to occur at the bottom area of the domain, imposing a certain *Inward displacement* L_0, on this boundary surface. The value of the displacement is found considering the US output intensity (I_0) of the Lipozero device, according to the expression:

$$I_0 = \frac{1}{2}\rho c\omega^2 L_0^2 \rightarrow L_0 = \sqrt{\frac{2I_0}{\rho c\omega^2}} \tag{2.12}$$

By setting this parameter in the simulation, the software automatically insert the *Normal displacement* in the right-hand side of the *Normal acceleration* equation, written as follows:

$$-n \cdot \left(-\frac{1}{\rho_c}(\nabla p_t - q)\right) = (i\omega)^2 L_0 \tag{2.13}$$

As a consequence, it is possible to simulate different US intensities by mathematically calculating the associated value of L_0.

Finally, the behavior of the acoustic wave close to the boundaries is described by setting specific *Impedance boundary* conditions on the lateral and upper surfaces of the domain, strictly dependent on the materials surrounding the solution. Therefore, for each boundary surface, except for the bottom area, the acoustic impedance of the material Z_i is introduced and the software insert it automatically in the right-hand side of the *Normal acceleration* equation:

$$-n \cdot \left(-\frac{1}{\rho_c}(\nabla p_t - q)\right) = -p_t \frac{i\omega}{Z_i} \tag{2.14}$$

Since the lateral walls of the well are made of polystyrene, the imposed impedance is $Z_i = \rho_{ps} \cdot c_{ps} = 1050\ Kg/m^3 \cdot 2350\ m/s$; differently, since the upper area of the liquid volume is in contact with air, the selected impedance is $Z_i = \rho_{air} \cdot c_{air} = 1.3\ Kg/m^3 \cdot 343\ m/s$.

In the following Table 2.3 are resumed all the quantities and parameters described in this section, used in COMSOL simulations:

Variable	Expression	Value	Description
freq	1[MHz]	1E6 Hz	applied US frequency
kz	2· p· freq/c	4197.2 1/m	US wavenumber
omega	2· p· freq	6.2832E6 Hz	US angular frequency
lambda	c/freq	0.001497 m	US wavelength
k0	$1/(c^2 \cdot \rho)$	4.4712E-10 1/Pa	water isoentropic compressibility
mu	0.890[mPa· s]	8.9E-4 Pa· s	water dynamic viscosity
mu_b	0.0024852[Pa· s]	0.0024852 Pa· s	water bulk viscosity
ρ_c	998[Kg/m^3]	998 Kg/m^3	water density
T0	298.15[K]	298.15 K	Equilibrium Temperature
r_24	7.95[mm]	0.00795 m	24 well basis radius
r_96	2.5[mm]	0.0025 m	96 well basis radius
H_24	10.78[mm]	0.01078 m	solution height in 24 well plate
H_96	10.19[mm]	0.01019 m	solution height in 96 well plate
L0_P0.30	14.19[nm]	1.419E-8 m	Inward displacement at P=0.30 W/cm^2 (10%)
L0_P0.45	17.5[nm]	1.75E-8 m	Inward displacement at P=0.45 W/cm^2 (15%)
L0_P0.60	20.056[nm]	2.0056E-8 m	Inward displacement at P=0.60 W/cm^2 (20%)
Z_air	4.46e2[Pa· s/m]	446 Pa· s/m	Air acoustic impedance
Z_ps	2.5e6[Pa· s/m]	2.5E6 Pa· s/m	Polysterene acoustic impedance

Table 2.3: COMSOL simulation parameters.

2.3 Results - Ultrasound irradiation on ZnO-water solutions within a single well from 24-well plate

In this section are reported all the results obtained from the laboratory experiments involving the single well of a 24 well-plate. The discussion begins with the COMSOL simulation outcomes, providing a general idea on how the acoustic field propagation is expected to behave within the well, specifically considering the intensity and pressure fields. Then, at a later stage, the Luminol and EPR measurements are discussed and compared also with

the KB cells viability results.

2.3.1 COMSOL simulations

Well 24

The acoustic pressure and intensity distributions of the US wave propagating along the single well of a 24-well plate were simulated through COMSOL, whose aim is to map and estimate the induced cavitation in different regions of the well. For this purpose, both vertical and horizontal planes within the well are selected to properly show the US wave behavior.

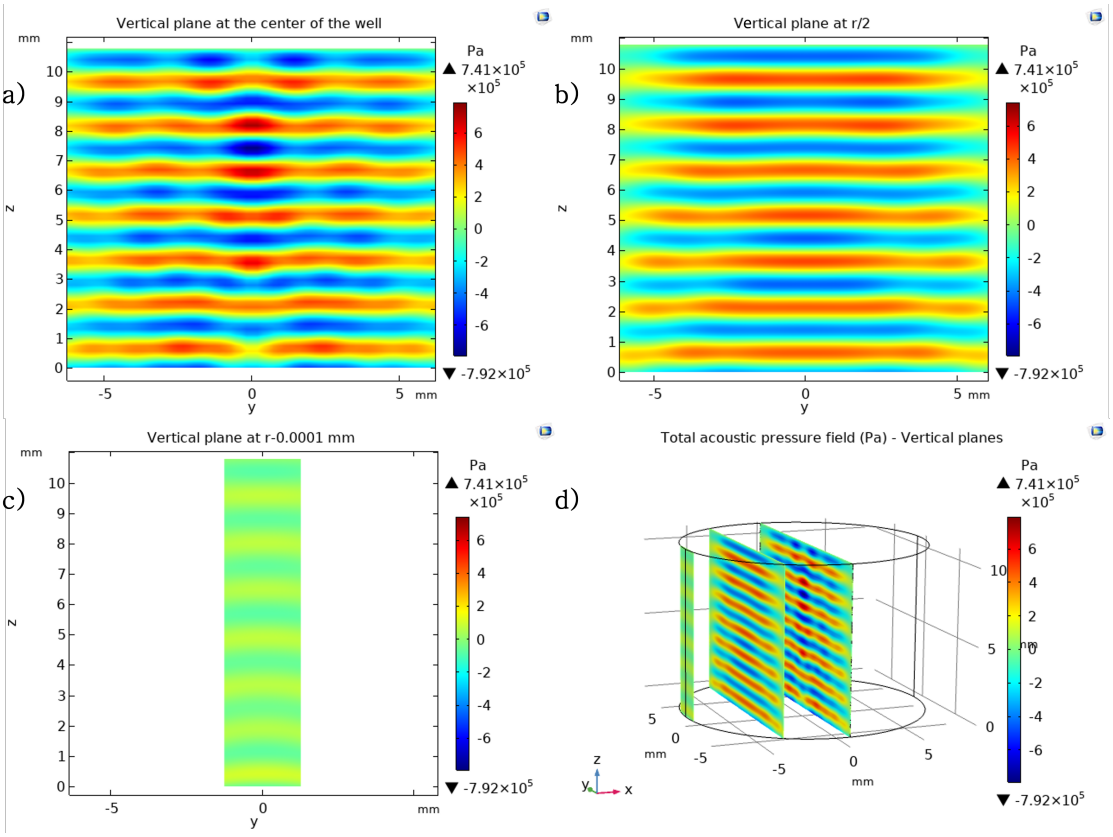

Figure 2.21: Pressure field distribution along different vertical planes within a 24 well: a) at the center of the well, b) at half the radius length, c) close to the boundaries at r-0.0001 mm, while d) highlights the position of the vertical planes.

All the simulation results reported in Figures 2.21, 2.23 and 2.22, were obtained by setting an input US power equal to 0.45 W/cm^2, corresponding to 15% of the Lipozero

maximum power, later employed in the experimental measurements. To allow the comparison with the other two analysed input powers, equal to 0.30 (10%) and 0.60 (20%) W/cm^2, since the US behaviour through the well was proved to be the same for every input power, only the average pressure amplitude and intensity in each vertical plane (Table 2.4) were extracted from their simulations. The choice of simulating these low input US powers relies on the evidence that cells, employed in the laboratory experiments, would completely die if exposed to higher US intensities, even without the presence of NCs. In fact, since 0.60 W/cm^2 is considered as the threshold power beyond which the viability rapidly decreases, these lower power values allow to simulate a scenario in which the cells viability mainly depends on the synergistic action of US and NCs.

As shown in Figures 2.21 and 2.23a, the acoustic pressure variation is represented by a gradient of colours in the "rainbow" scale, where the darkest red and blue colours indicate respectively the maximum and the minimum values that the pressure can assume, equal to +- 0.74 MPa. For the acoustic intensity, (Figures 2.22 and 2.23b), the darkest blue and red colours correspond to 0 W/cm^2 and 11 W/cm^2 respectively.

In particular, as presented by Figures 2.21 and 2.22, three vertical Y-Z planes were chosen at specific coordinates inside the well: at the center (X = 0), at half of the radius length (X = 3.98 mm) and close to the lateral surface (X = 7.85 mm, namely 0.0001 mm from the well outer walls). These planes positions allow to study the pressure and the intensity distributions along the wave propagation direction (i.e. the vertical axis, Z) and analyse their different behavior when moving towards the well boundaries (along the horizontal X and Y axis).

The vertical pressure distribution (Figure 2.21) demonstrates that the input US wave, normally incident to the well bottom surface, forces the acoustic field inside the well to experience an alternation of compression and rarefaction cycles, corresponding respectively to the highest and lowest pressure phases, with intermediate phases in between. In general, a sinusoidal trend characterizes the pressure along the vertical direction; however, its behaviour in the central plane particularly differs from the others since the pressure peaks are subjected to a visible variation along both the vertical (Z) and horizontal (Y) directions. Instead, in the other two planes, a more regular trend of the pressure is observed, where the peaks assume similar values both along Z and Y. This difference may be caused by the particular interferences generating inside the planes due to the interaction (transmission and reflection phenomena at each specific position) of the US wave with the well cylindrical surfaces as well as with air, simulated at the top of the well. Therefore, the central plane appears to be subjected to strong constructive and destructive interference effects,

respectively originating diversified local maxima and minima pressure amplitude regions, while the other two planes seem to be less influenced by this phenomenon. Furthermore, the central plane shows that the highest pressure amplitudes are found around its central vertical line (Y=0), reaching their maxima in correspondence of half the well's height, and then tend to decrease moving closer to the lateral boundaries. Consequently, the pressure peaks along the plane at the surface, which is the most distant from the central region of the well, show a visible decrease in their amplitudes. This reduction could be caused by the scattering of the US wave while propagating inside the water solution as well as its interaction with the lateral walls, since both the particular geometry and the well material (polysterene) may generate destructive interferences near the surfaces.

The computed acoustic intensity distribution along the vertical planes (Figure 2.22) is in agreement with the pressure results; in fact, since the pressure amplitude is proportional to the intensity, the highest intensity values are observed around the central vertical line of the central plane, reaching the maximum at the center of the well. Moreover, some characteristics of the US field already acquired from the pressure plot are even more appreciable from the intensity distribution: firstly, the interference effects, represented by the fringes pattern, are much stronger in the central plane than in the other two planes; secondly, Figure C distinctly reveals how the energy transported by the US wave rapidly decreases moving from the well center towards its lateral surfaces. Therefore, this simulation result suggests that the strongest cavitation activity occurs around the well central region.

The simulated US field was analysed also along X-Y horizontal planes, set at different well's heights: at Z = 0 (bottom surface), Z = 2.5 mm, Z = 7.5 mm and Z = 10.7 mm (top surface), as shown in Figure 2.23. Concerning the pressure behaviour, Figure 2.23a demonstrates that, along each plane, the pressure distributes horizontally with a gradually decreasing oscillatory trend, expanding from the center to the lateral surface by means of symmetrical phases. This trend can be associated to the superposition of the wave components propagating along the X-Y plane, which interfere after interacting with the well walls. Furthermore, at both the central regions of the top and the bottom surfaces, an extremely low pressure (near to 0 Pa) is observed, indicating that the cavitation mechanism is more likely to occur and has a stronger intensity inside the well internal volume, while it rapidly vanishes moving towards the top and the bottom surfaces.

Similar observations can be done for the horizontal intensity distribution (Figure 2.23b): a pattern of concentric fringes generated by interference clearly expands through the two internal planes, where the intensity presents the highest values in a narrow region at the well center and sharply decreases by moving towards the well lateral edges. Differently, in

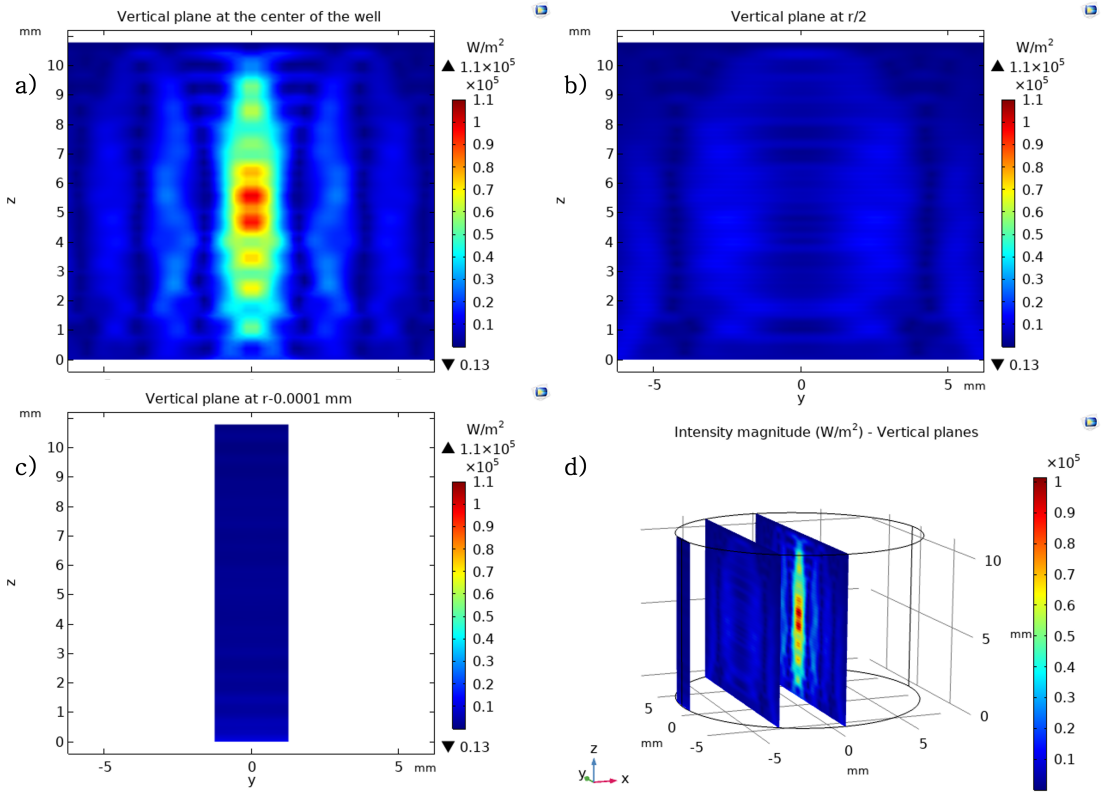

Figure 2.22: Intensity distribution along different vertical planes within a 24 well: a) at the center of the well, b) at half the radius length, c) close to the boundaries at r-0.0001 mm, while d) highlights the position of the vertical planes.

correspondence of the two outer horizontal planes of the domain, the intensity assumes almost negligible values which underlines once more the presence of an internal well volume, around half the well's height and quite distant from the top and bottom surfaces, responsible for an enhanced cavitation strength.

A final analysis is carried out by extracting the average pressure amplitude and intensity for each of the input US powers, along the previously considered three vertical planes (Table 2.4). The numerical results can be interpreted at each fixed power and at each fixed well plane. By fixing any of the powers, the average pressure amplitude and intensity rapidly decrease by moving from the well center towards its lateral surface, in coherence with the previous results. By fixing the well plane, a decrease of both the pressure amplitude and the intensity proportionally to the power reduction occurs for each plane. More in details, the average intensity in the central plane is subjected to a much important reduction when

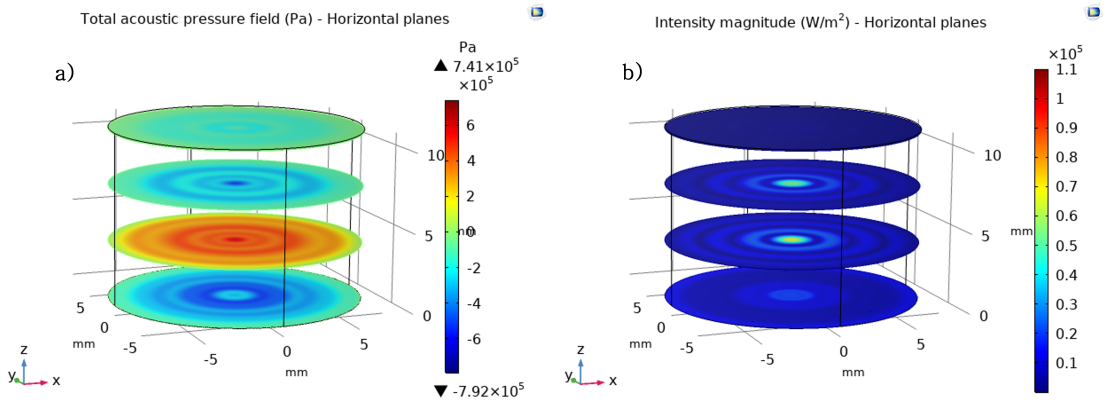

Figure 2.23: Planes cutting horizontally the 24 well and showing a) the pressure distribution and b) the intensity distribution.

the input power is decreased: this different behaviour could be associated to a stronger influence of the input US power on the well center compared to the positions closer to the lateral surface, which indeed present average intensity values approaching 0 W/cm2 for each input power condition.

Power	**20%**	**15%**	**10%**
Input intensity (W/cm^2)	0.60	0.45	0.30
Bottom wall displacement (nm)	20.056	17.5	14.19
P amp avg central (MPa)	0.307	0.268	0.217
P amp avg r/2 (MPa)	0.253	0.221	0.179
P amp avg wall (MPa)	0.146	0.128	0.104
Intensity average Central (W/cm^2)	1.665	1.268	0.833
Intensity average r/2 (W/cm^2)	0.779	0.593	0.389
Intensity average wall (W/cm^2)	0.624	0.475	0.312

Table 2.4: Different intensity and pressure values within a 24 well associated to 20%, 15% and 10% US powers.

Well 96

The US wave pressure and intensity distributions are also simulated in a single well of a 96-well plate to allow for a direct comparison with the 24 well results as well as to get an idea over the intensity and pressure magnitudes to which cells are subjected during their

treatment (usually the cells are placed in single wells of a 96-well plate).

In general, from both the pressure and intensity simulations, the behaviour obtained seems to be strictly dependent on the particular well geometry, showing slight differences compared to the single well of a 24-well plate. In fact, since the wells material remains the same (polysterene), the change in the pressure and intensity distributions are caused only by the different shape of a 96 well, characterized by a solution volume height which is almost the same of a 24 well, but with a much smaller radius, resulting in an higher aspect ratio of its structure.

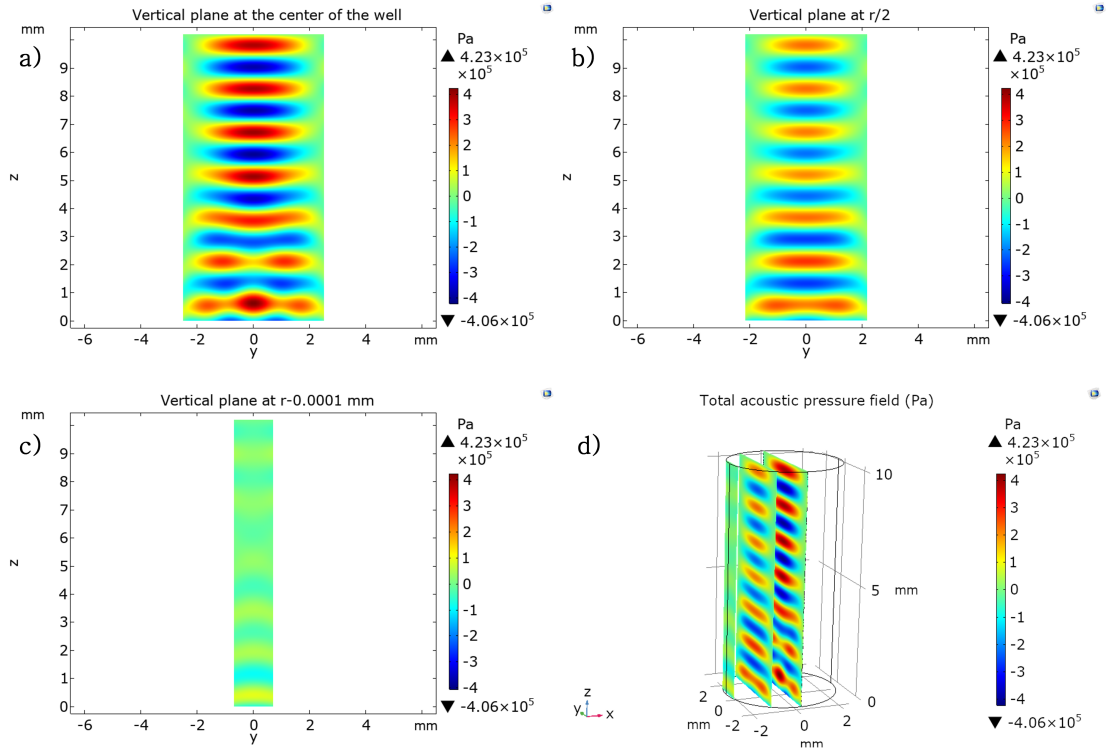

Figure 2.24: Pressure field distribution along different vertical planes within a 96 well: a) at the center of the well, b) at half the radius length, c) close to the boundaries at r-0.0001 mm, while d) highlights the position of the vertical planes.

The pressure distribution along the vertical planes within the well (Figure 2.24), whose positions in relation to the well radius remain the same as in the 24 well, reveals a higher pressure magnitude in correspondence to the well central region, which decreases by moving towards the lateral surfaces. Compared to the 24 well results, even if the global behaviour is approximately equal, some slight differences can be observed: firstly, the decrease of

the pressure peaks when moving from the center towards the lateral regions of the well (along X and Y axis) is much sharper, caused by the smaller well radius; secondly, in the vertical plane positioned at half of the radius length, the pressure visibly reduces when moving from the well bottom towards the top surface. These trends may be caused by the particular interference effects originating from the different well geometry, responsible for an important destructive interference at the well lateral surfaces, which affects also the pressure peaks along the height of the well.
The pressure distribution along the horizontal planes, Figure 2.26a, further underlines the rapid pressure decrease when moving from the center of the well towards its lateral walls.

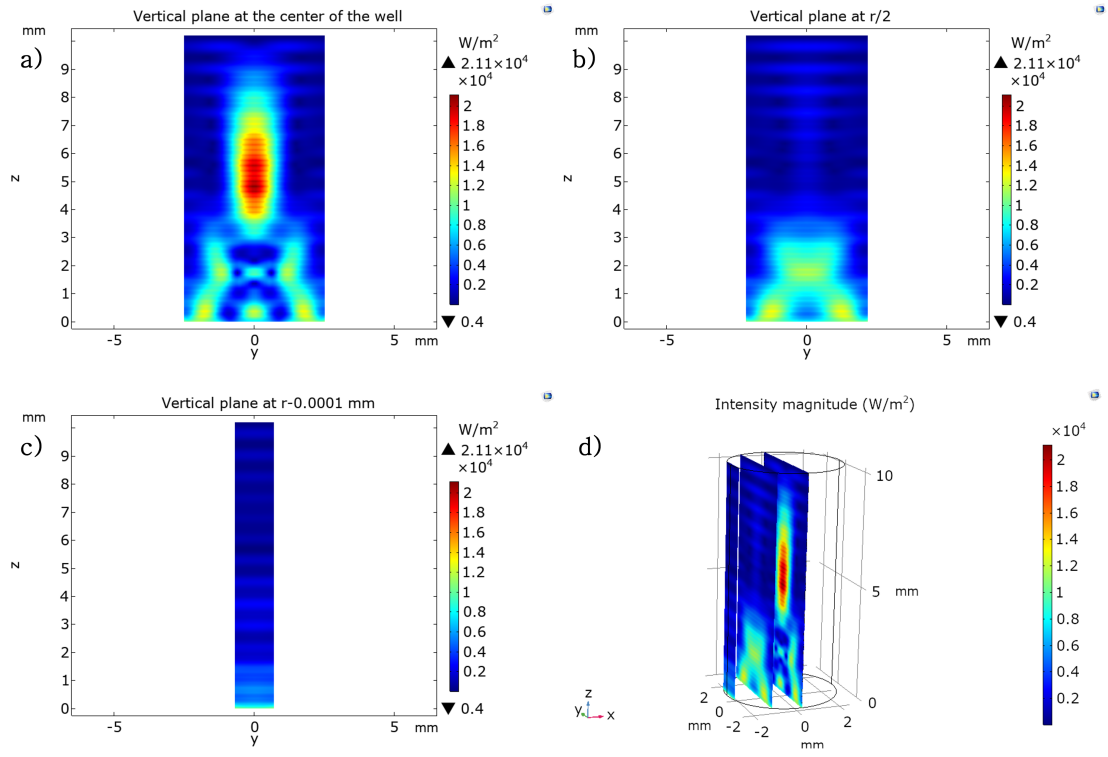

Figure 2.25: Intensity distribution along different vertical planes within a 96 well: a) at the center of the well, b) at half the radius length, c) close to the boundaries at r-0.0001 mm, while d) highlights the position of the vertical planes.

The intensity distribution, in Figures 2.25 and 2.26b, emphasize the presence of an inner volume at the center of the well showing the highest intensity values: this region, corresponding also to the highest pressure peaks, may be responsible for an enhanced cavitation strength. On the other hand, differently from the 24 well simulations, also the liquid volume below the central area of the 96 well presents moderate intensity values, following a

concentric shape in relation to the well central vertical line: this behaviour may be caused by the narrower 96 well geometry.

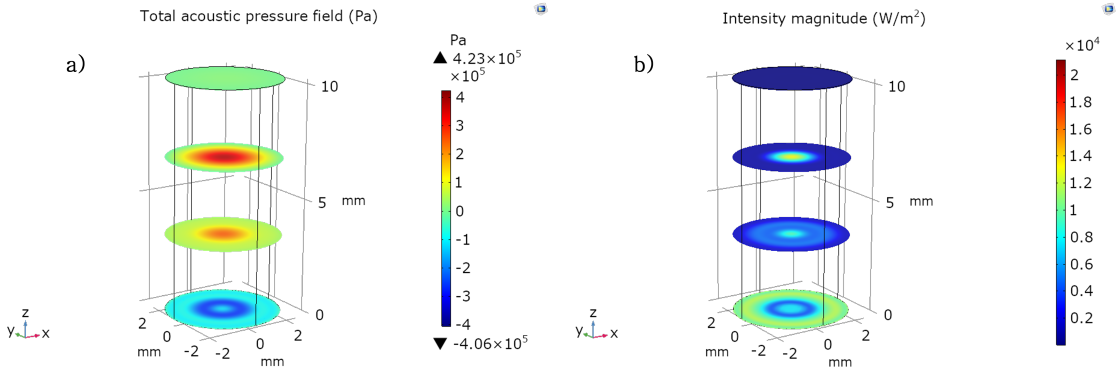

Figure 2.26: Planes cutting horizontally the 96 well and showing a) the pressure distribution and b) the intensity distribution.

Power	**20%**	**15%**	**10%**
Input intensity (W/cm^2)	0.60	0.45	0.30
Bottom wall displacement (nm)	20.056	17.5	14.19
P amp avg central (MPa)	0.192	0.167	0.136
P amp avg r/2 (MPa)	0.147	0.129	0.104
P amp avg wall (MPa)	0.075	0.066	0.053
Intensity average Central (W/cm^2)	0.617	0.469	0.309
Intensity average r/2 (W/cm^2)	0.410	0.312	0.205
Intensity average wall (W/cm^2)	0.213	0.163	0.107

Table 2.5: Different intensity and pressure values within a 96 well associated to 20%, 15% and 10% US powers.

All the previous simulations results are associated to an input US power of 0.45 W/cm^2 (15%), while for the 0.60 W/cm^2 (20%) and 0.30 W/cm^2 (10%), only the average pressures and intensities in each vertical planes are extracted and presented in Table 2.5.

As already observed for the 24 well, by fixing any US power, both the pressure and intensity magnitudes decrease when moving from the center of the well towards its lateral surfaces; then, by fixing a specific plane, the pressure and intensity average values vary proportionally with the US input power considered.

In general, compared to the 24 well, both the average pressure and intensity values within a 96 well are lower, being approximately equal to half of the magnitudes obtained in the 24 well, under the same conditions of applied US input power. In fact, while for the 24 well the central plane was characterized by US intensities much higher than the input ones, the US intensities obtained in the central plane for a 96 well reflects almost the same values of input intensity (0.60 W/cm^2 of input power corresponds to 0.617 W/cm^2 of average US intensity developed along the central plane of the well).

2.3.2 Luminol sonochemiluminescence

Since the initial laboratory experiments, relying on Luminol sonochemiluminescence, consist in a large amount of measurements in order to find the best possible sonication power and time combinations, the results are numerous and can be organized in two main categories: high and low US powers.

1. High US powers

The first analyzed conditions are focused on the high sonication powers, in particular 60%, 80% and 100% associated to short sonication times, 5, 10, 15 and 30 s. Since the results obtained are various, after the following description the measurements related to the four sonication time periods are presented in Figures 2.28, 2.29, 2.30 and 2.31, each one divided in three different images.

In general, for all the considered conditions, the first table shows the well images resulting from the pixel-by-pixel subtraction procedure between the acquired image, taken during the sonication process in the dark environment, and the frame/background image. By comparing the tables associated to different sonication times, it is evident an increase in the blue colour intensity as the time period becomes longer, even without having done yet any processing of the image. However, this behaviour is supported by the second and third images of each condition, that represent the blue intensity profile along the diameter of the well and the average blue intensity value within the well, respectively.

Since the rectangular ROI employed for the extrapolation of the blue intensity profiles slightly exceeds the lateral boundaries of the well circular shape, the profiles themselves are characterized by two lateral regions, corresponding to the more distant areas from the center of the well, with the lowest blue intensity values. As the distance from the central part of the well is reduced, the intensity increases, showing a particular trend consisting on two peaks in close proximity to the center and a slight drop approximately at the center of the well. However, this distinctive behavior seems to disagree with the COMSOL simulations previously presented; in fact, while in the simulation results, the highest possible acoustic wave pressure and intensity are found to be in the region at the center of the well, inducing an enhanced acoustic cavitation phenomenon and consequent production of ROS, in the experimental results the blue intensity shows a drop in correspondence to the central area of the well, meaning a slightly lower generation of ROS in the same region. This phenomenon may be explained by the motion and turbulence of the Luminol solution during sonication, that provides a redistribution and rearrangement of the particles inside

the fluid, leaving the central area which is the most affected by the presence of high acoustic field and thus, stronger liquid streaming phenomena.

By comparing the three different powers while maintaining the same sonication time, no great differences between them are highlighted in the blue intensities obtained, in some cases characterized by a predominance of the 60% power over the 80% and 100%, while in other conditions a higher 80% intensity overcomes the other powers. In general, it seems that the blue intensity values reach a certain saturation condition when dealing with very high powers, over the 60%, that give no major differences between the Luminol blue intensities obtained with the 80% or the 100% powers. This characteristic is also evidenced in the average intensity values histogram.
Finally, the effect of nanoparticles can be investigated for each condition through the comparison of the blue intensities obtained in the control solutions (left) and in ZnO-NH_2 enriched solutions (right). However, the influence of NPs that should provide an increase in ROS generation and therefore, an enhanced blue intensity, is not so evident, showing higher values only for some time periods, in particular for 5 and 10 s.

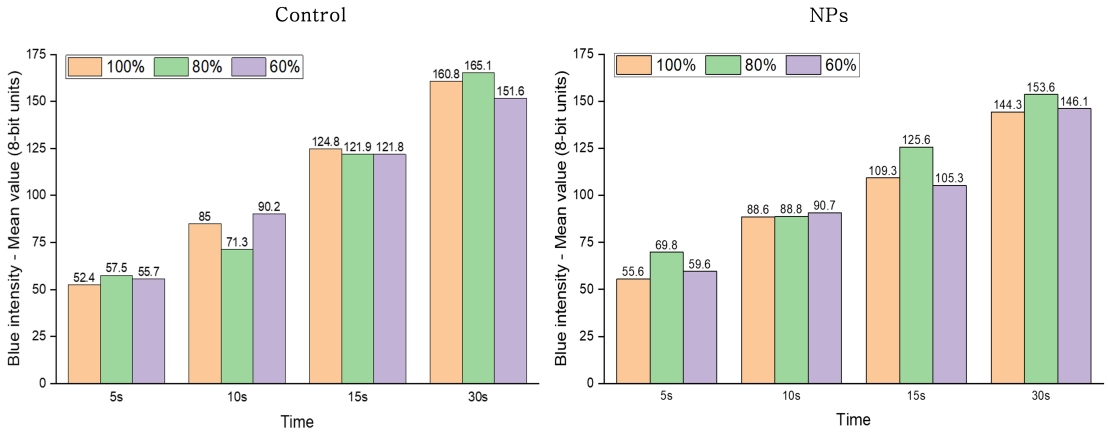

Figure 2.27: Summary of all the average blue intensity values obtained for high powers.

To conclude, the last Figure 2.27 summarizes all the average intensity values obtained for all the conditions of sonication powers and times, allowing for an immediate sight over the general trend of the results as well as a direct comparison between the values related to the control solutions and to the NPs-enriched solution. The most noticeable behaviour remains the increase of the blue intensity as the sonication time is increased, while a not so evident difference is found both when considering different sonication powers but also

when comparing the control and the NPs-enriched solutions.

Power (%)	Time (s)	Image	
		Control	NPs
100	5	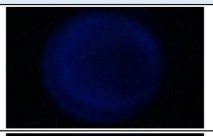	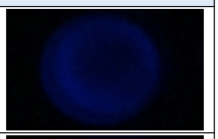
80	5	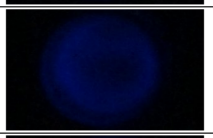	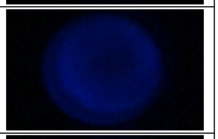
60	5	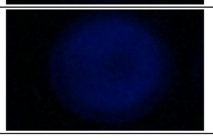	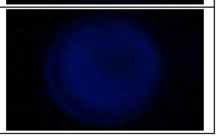

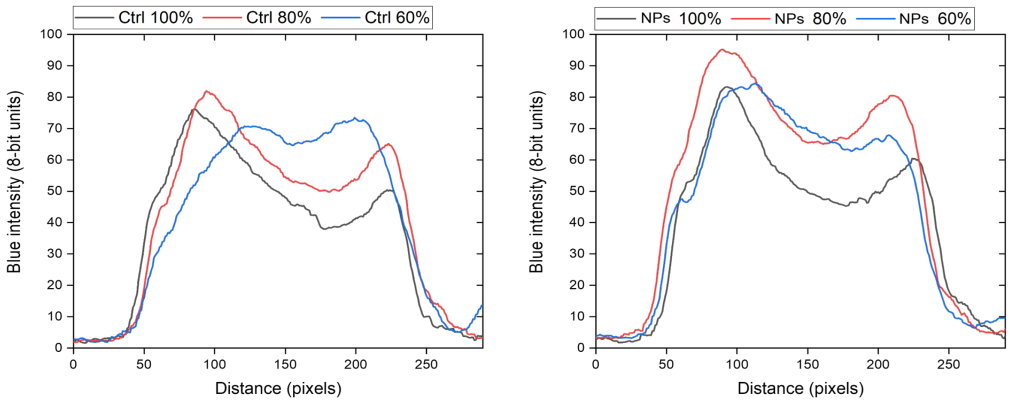

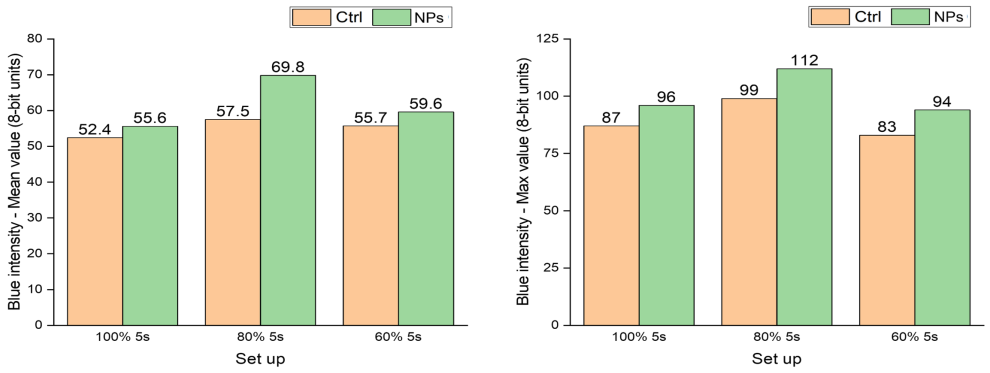

Figure 2.28: Results of the condition with high powers and sonication time = 5 s. Top: well images without background; Center: blue intensity profiles for the control (left) and NPs-enriched (right) solutions; Bottom: average (left) and maximum (right) blue intensities.

Power (%)	Time (s)	Image	
		Control	NPs
100	10	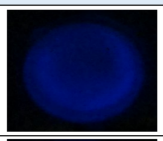	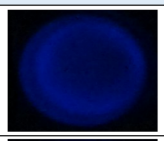
80	10	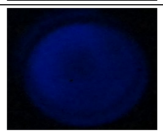	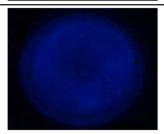
60	10	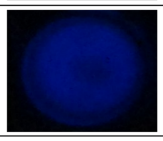	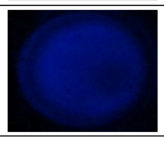

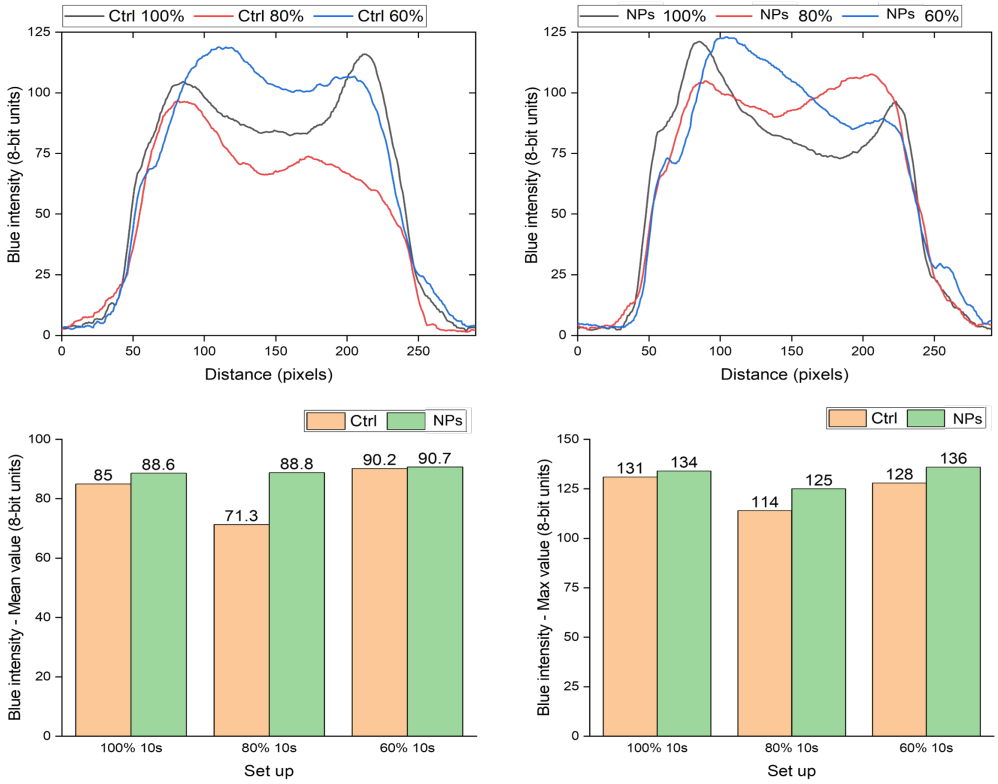

Figure 2.29: Results of the condition with high powers and sonication time = 10 s. Top: well images without background; Center: blue intensity profiles for the control (left) and NPs-enriched (right) solutions; Bottom: average (left) and maximum (right) blue intensities.

Power (%)	Time (s)	Image	
		Control	NPs
100	15	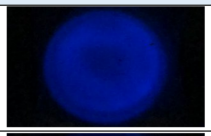	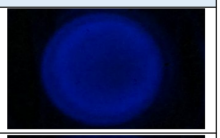
80	15	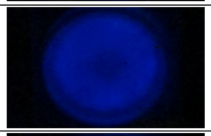	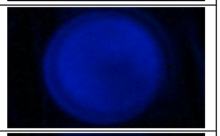
60	15	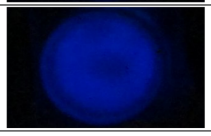	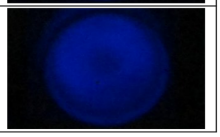

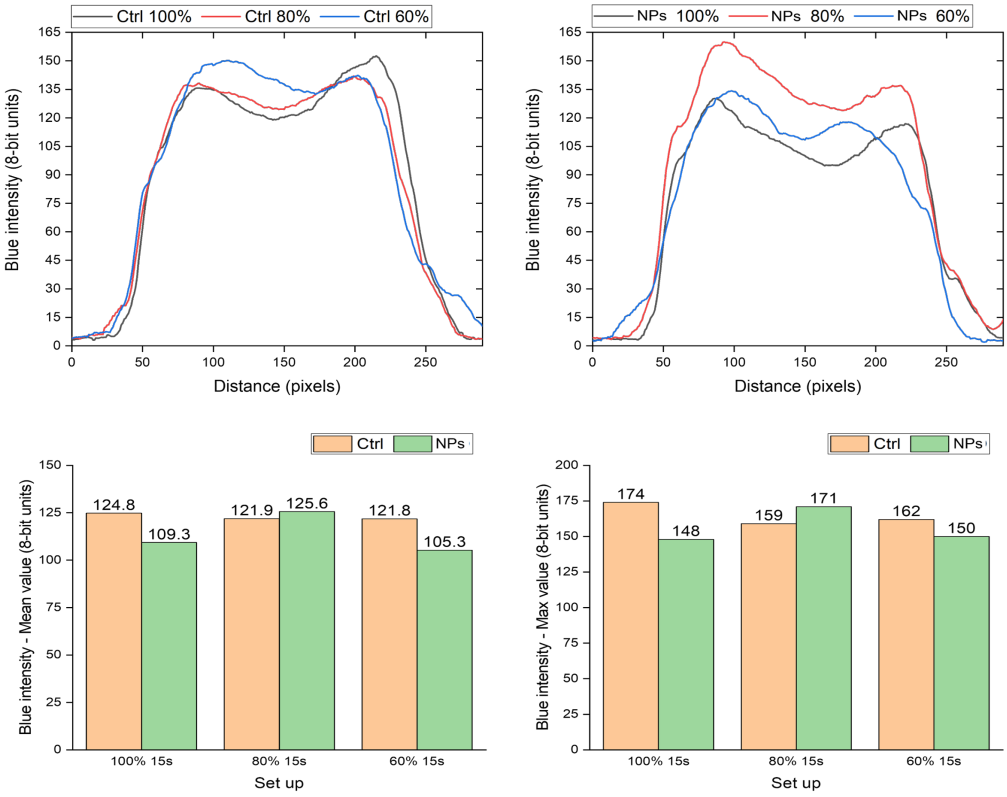

Figure 2.30: Results of the condition with high powers and sonication time = 15 s. Top: well images without background; Center: blue intensity profiles for the control (left) and NPs-enriched (right) solutions; Bottom: average (left) and maximum (right) blue intensities.

Power (%)	Time (s)	Image	
		Control	NPs
100	30	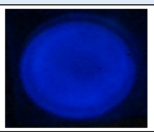	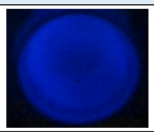
80	30	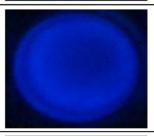	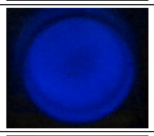
60	30	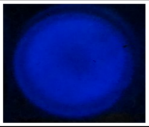	

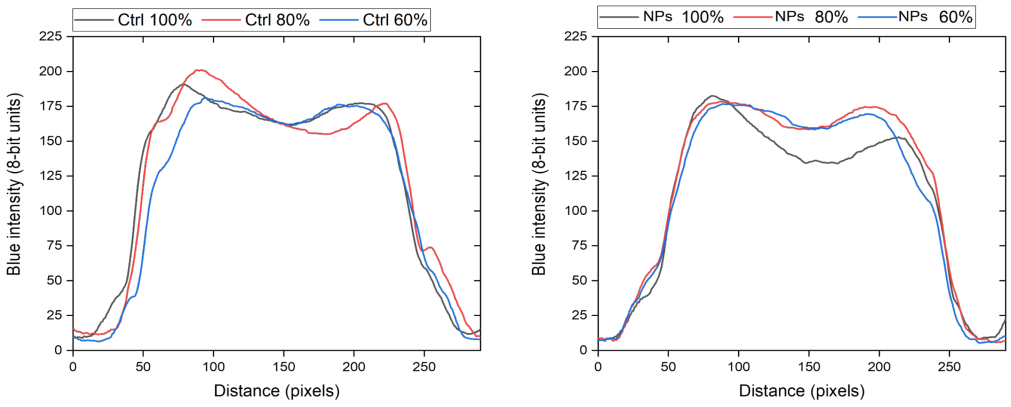

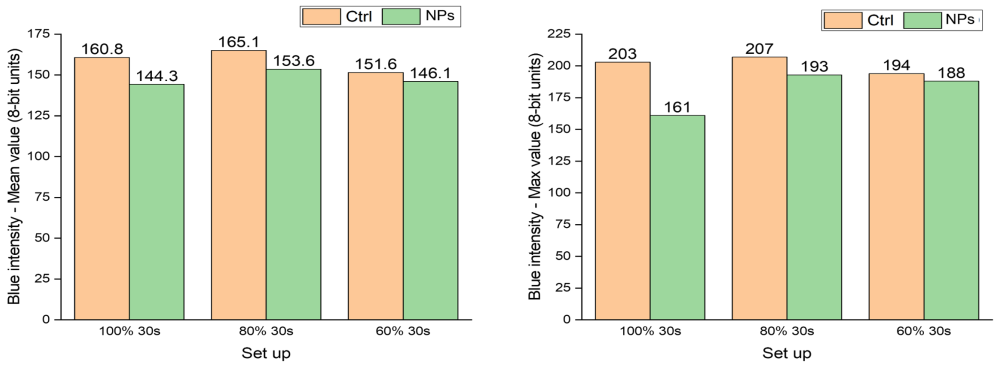

Figure 2.31: Results of the condition with high powers and sonication time = 30 s. Top: well images without background; Center: blue intensity profiles for the control (left) and NPs-enriched (right) solutions; Bottom: average (left) and maximum (right) blue intensities.

2. Low US powers

The discussion concerning the low powers measurements are quite similar to the previous high powers analysis. In this case, since the lower powers are the most suitable for the treatment of cells, the effect of several power values are examined, in particular the 50%, 40%, 30%, 25%, 20%, 15% and 10% for four longer sonication times 30 s and 1, 2, 3 min. As before, the various results are reported in Figures 2.32, 2.33, 2.34 and 2.35.

Following the same description, the first table related to each sonication time condition reports the acquired images, already processed by subtracting the background. Also in this case, only by looking at the images, before any blue intensity extrapolation, it is possible to notice the increase in the blue color as the sonication times become longer. Furthermore, differently from the high powers condition, for increasingly higher powers, thus starting from 10% value and rising it up to 50%, a gradual increase in the blue intensity inside the well is evident for each sonication time. This trend is also in accordance with the blue intensity profiles and the mean intensity values.

The general behaviour of the blue intensity profile is almost the same also described for the high powers condition; however, for all the various sonication times, a net difference between the associated profiles of each low power is rather visible. As the US treatment is prolonged for longer time periods, the blue colour acquired is so intense that the maximum achievable value of blue intensity that can be processed through ImageJ software, corresponding to 255 (2^8 bits), is reached. As a consequence, the blue intensity profiles show a saturation for the higher powers, as 40% and 50%, particularly in the case of 3 min sonication time.

By comparing the results related to the control and NPs-enriched solutions, both the blue intensity profiles and the mean blue values obtained give a quite conflicting behaviour: for some sonication times, as 30 s and 1 min, the control values result to be higher than the NPs ones, while for the time periods 2 min and 3 min, the NPs solutions have higher blue intensities than the control ones.

At the end, Figure 2.36 summarizes the overall behaviour, allowing for a direct comparison among the results concerning all the sonication powers and times as well as the difference between control and NPs solutions. In general, for the low powers condition, it is possible to notice an increase in the blue intensity values in two particular cases: when the sonication power is increased while maintaining fixed the sonication time and when the time period is prolonged while maintaining constant the US power. Moreover, as the US treatment time is increased, the effect of NPs becomes increasingly significant.

Power (%)	Time (s)	Image	
		Control	NPs
50	30		
40	30		
30	30		
25	30		

Power (%)	Time (s)	Image	
		Control	NPs
20	30		
15	30		
10	30		

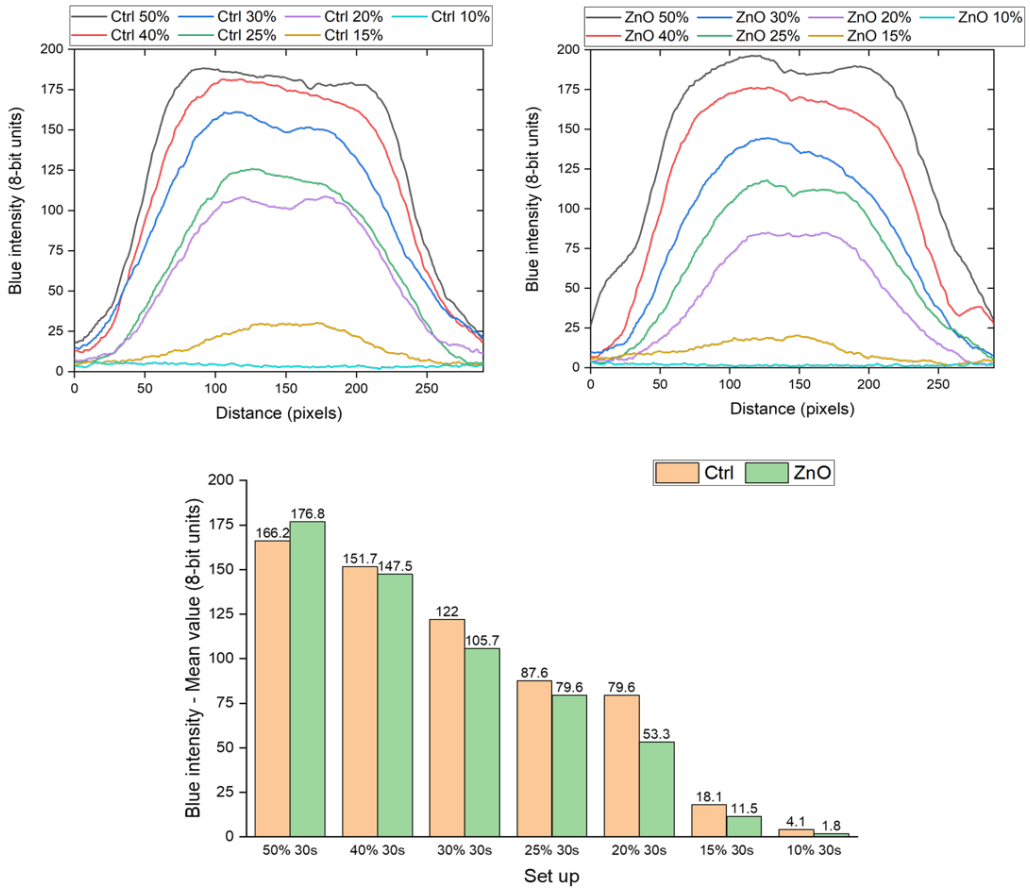

Figure 2.32: Results of the condition with low powers and sonication time = 30 s. Top: well images without background; Center: blue intensity profiles for the control (left) and NPs-enriched (right) solutions; Bottom: average blue intensity.

Power (%)	Time (s)	Image	
		Control	NPs
50	60	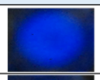	
40	60		
30	60	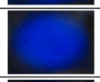	
25	60	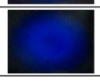	

Power (%)	Time (s)	Image	
		Control	NPs
20	60		
15	60		
10	60		

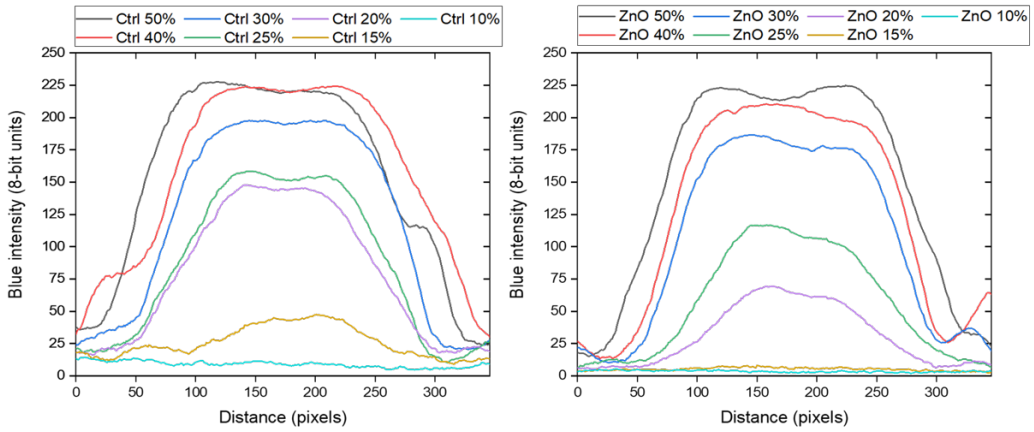

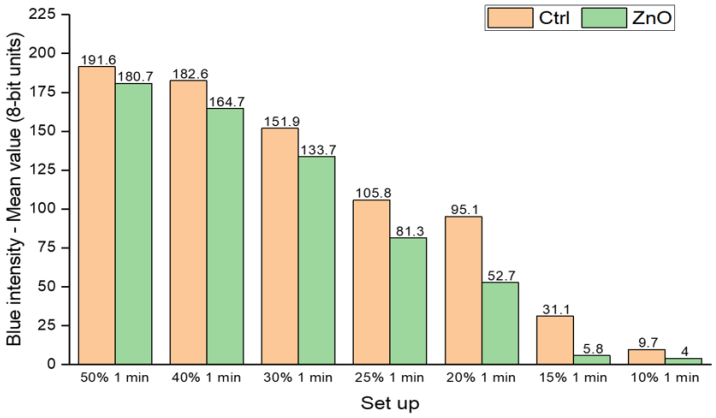

Figure 2.33: Results of the condition with low powers and sonication time = 60 s = 1 min. Top: well images without background; Center: blue intensity profiles for the control (left) and NPs-enriched (right) solutions; Bottom: average blue intensity.

Power (%)	Time (s)	Image	
		Control	NPs
50	120		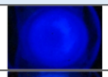
40	120	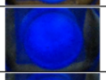	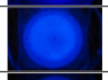
30	120	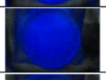	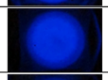
25	120	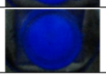	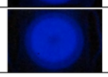

Power (%)	Time (s)	Image	
		Control	NPs
20	120	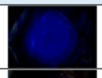	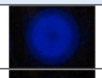
15	120		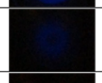
10	120		

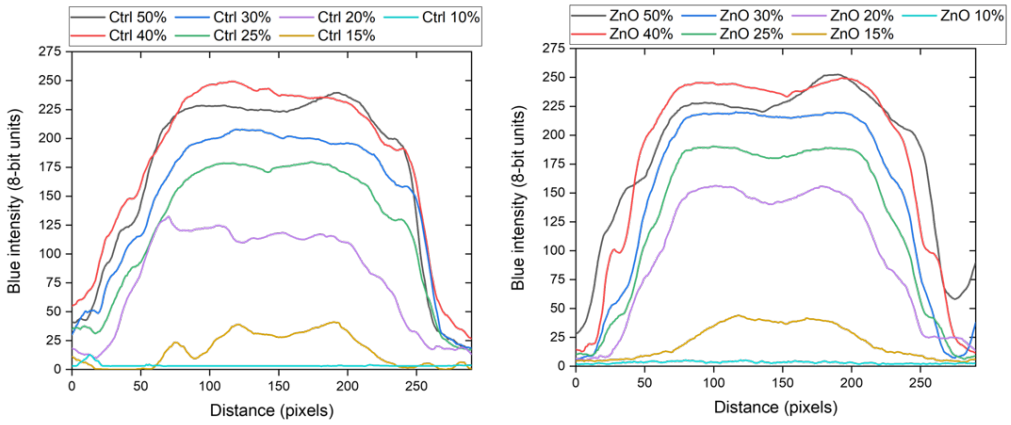

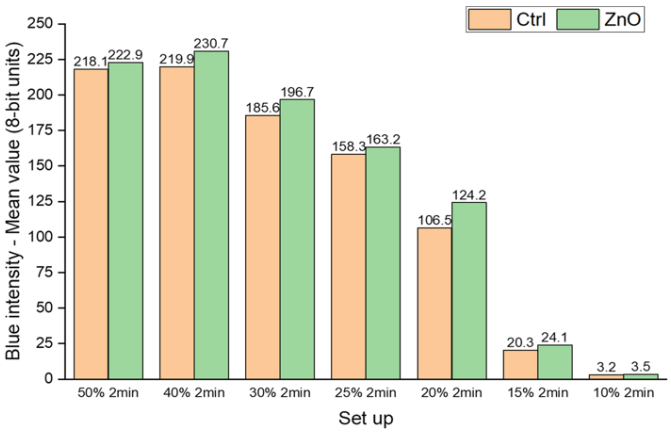

Figure 2.34: Results of the condition with low powers and sonication time = 120 s = 2 min. Top: well images without background; Center: blue intensity profiles for the control (left) and NPs-enriched (right) solutions; Bottom: average blue intensity.

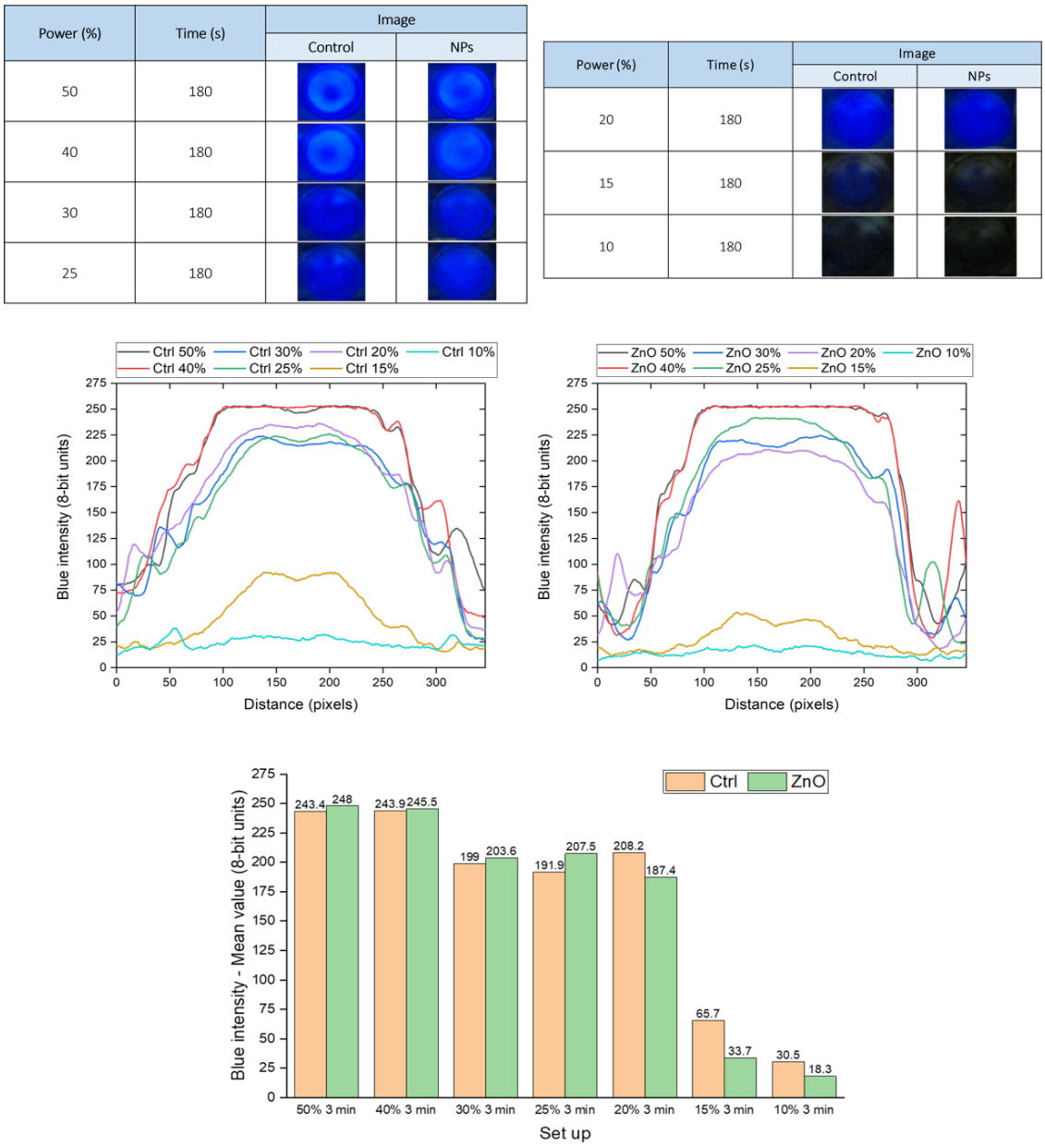

Figure 2.35: Results of the condition with low powers and sonication time = 180 s = 3 min. Top: well images without background; Center: blue intensity profiles for the control (left) and NPs-enriched (right) solutions; Bottom: average blue intensity.

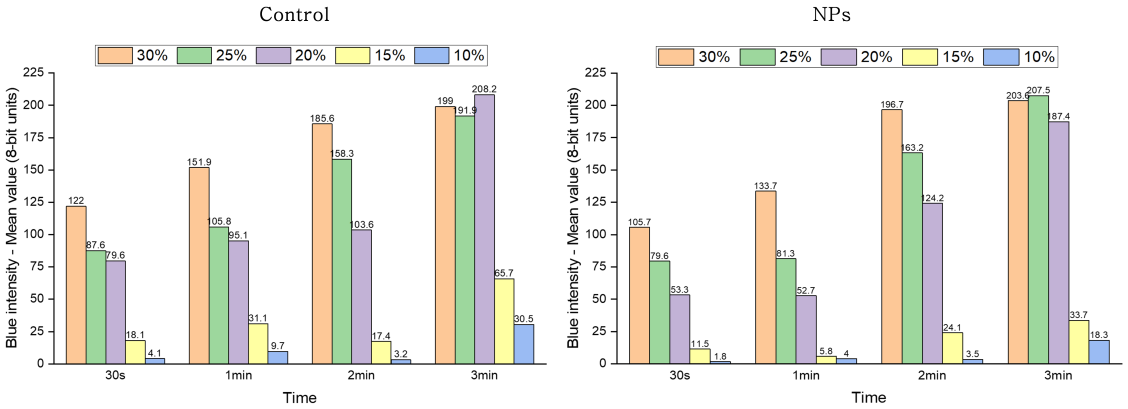

Figure 2.36: Summary of all the average blue intensity values obtained for low powers.

Control measurements

Figure 2.37 compares the results obtained respectively from the KB cells viability and the SCL control measurements (i.e. in absence of ZnO nanoparticles). As Figure 2.37a shows, cells viability provides an estimation of the US-induced cytotoxic effects on cells for any treatment condition. Focusing on the lowest applied power, 0.3 W/cm^2 (corresponding to 10% of the maximum achievable power from Lipozero), the cells result to be not significantly affected by the US treatment, even for the longest sonication times. In fact, the observed high viability values, exceeding also the 100%, are indicative of cells proliferation and growth at these US conditions, rather than of their death.
The cells viability trend appears to be globally lower at 0.45 W/cm^2, as expected by the stronger cytotoxic effect being proportional to the applied US power. In particular, even if the standard deviation is quite large for all the measurements, the average values show a significant decreasing behaviour when the US treatment is prolonged for sonication times longer than 1 minute. This implies that, for treatment times of the order of tens of seconds, cells are not notably harmed by US, whose cytotoxic effects seem instead to become increasingly important for longer sonication times, of the order of minutes.
A completely different behaviour is presented by the measurements at 0.60 W/cm^2 of applied US power, whose average cells viability values are indicative of an evident cytotoxic effect at any employed sonication time: the reduction in the fraction of alive cells can be noted even for shorter treatment times, with a sharpdecrease when the time is extended from 15 to 30s. From this sonication time onwards, the US treatment has significant effects, responsible for the death of the majority of cells: up to 3 minutes, the viability is not subjected to a considerable further decrease, but it remains quite low, around 30%.

The cells viability behaviour is well supported by the Luminol sonochemiluminescence measurements, Figure 2.37b. In fact, the average blue intensity of the light coming from the well globally shows an increasing trend proportional to longer sonication times and higher powers of the applied US. Therefore, a direct comparison between the cells viability and the SCL results for each treatment condition may be discussed. Considering firstly the lowest US power (0.3 W/cm^2), since the related blue intensity assumes negligible values for all the sonication times, not showing any increasing behaviour even for longer US time periods, this trend demonstrates to be rather consistent with the cells viability obtained at the same power. In fact, the absence of cells death in a viability experiment corresponds to a null blue intensity detected in a SCL analysis, meaning that a not sufficient amount of ROS is generated to induce cells to death as well as to activate Luminol molecules.

Concerning the results obtained by applying the second US power, 0.45 W/cm^2 (15%), a negligible Luminol blue intensity is observed for shorter sonication times, while, differently from the previous power condition, it gradually increases from 1 to 3 minutes. In particular, at 0.45 W/cm^2, a treatment of 1 min represents the first sonication time able to produce a detectable SCL light, even if its value is still very low. This result is consistent with the cells viability data, where the first non-negligible cytotoxicity was obtained at 2 minutes, associated to a slightly higher SCL intensity. Actually, 3 minutes of sonication time corresponds to the first condition at which both a noticeable cells death and SCL intensity were measured. Therefore, the combination of an applied power of 0.45 W/cm^2 and a treatment time of 2 minutes may represent a threshold condition for the production of a sufficient amount of ROS able to provide an effective cells death.

Finally, at 0.60 W/cm^2 (20%), the SCL intensity histogram shows not negligible values even at the shortest sonication time, 5 seconds, and assumes a gradual increasing trend as function of the treatment time. As expected by the proportionality between generated ROS and cells death, this behaviour is in strong agreement with the average cells viability values: at shorter times, both the percentage of dead cells and the blue intensity have a certain relevance, which is further enhanced for treatment times longer than 30s. Therefore, the highest possible values of dead cells and SCL intensity were measured by applying an US power of 0.60 W/cm^2 for 3 minutes of treatment. Moreover, it can be affirmed that in this experimental set-up the cavitation threshold lays in the range between 0.45 - 0.60 W/cm^2 since starting from these power values a consistent cavitation effect was observed, both in terms of cells death and SCL intensity.

Therefore, Luminol sonochemiluminescence may represent a useful method to rapidly

and directly measure, in a qualitative way, the amount of ROS generated inside the sonicated solution, proved by the consistency of the obtained results with the cells viability values.

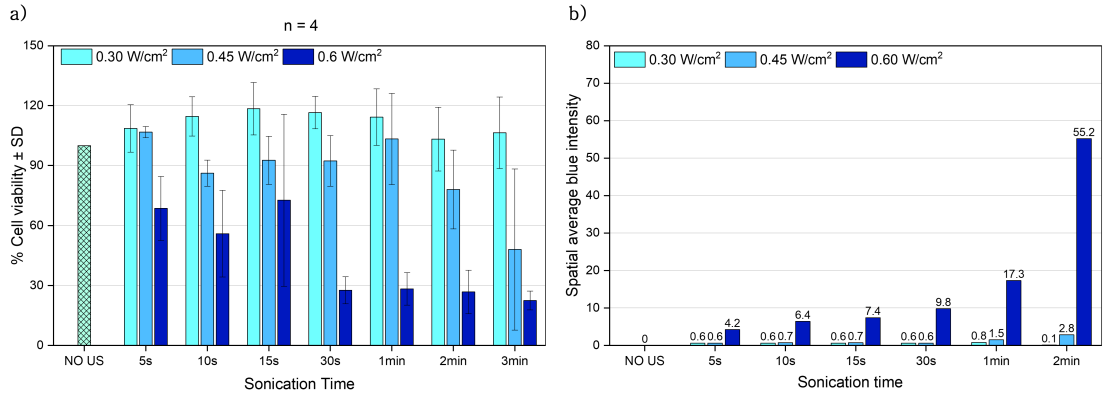

Figure 2.37: Control measurements for different sonication power and time combinations: a) cells viability and b) Luminol blue intensity.

NPs measurements

The control measurements allowed to select the proper US power values employed for the sonication of the NPs-enriched solutions, providing a direct evidence of the effect of NPs compared to the control solutions. In particular, in these late experiments, the choice to apply the US powers equal to 0.3 (10%) and 0.45 (15%) W/cm^2 comes from the evidence that these two input intensities appear to have a non-toxic behaviour to the cells when used alone (without NPs), as it is demonstrated by the cells viability control results (Figure 2.37). For similar reasons, the NPs concentration of 10 µg/mL was introduced inside the solutions since, on one hand, it resulted to not cause any damage to the cells in absence of an applied US input power, but on the other hand, it provides a sufficiently high amount of NPs to obtain an effective uptake. Therefore, Figure 2.38c shows whether the synergistic action of US and NPs affects the cells viability, by analyzing also the influence of different sonication times. As presented by the reference results, in which the solutions did not undergo any US treatment, the cells viability obtained for the NPs-enriched samples is higher than the control one, even higher than 100%, indicative of cells proliferation. This behaviour does not differ much when any US power is applied for different times: globally, the effect of an US external stimuli together with the presence of NPs inside the solutions results to be not so visible.

However, these measurements are consistent with Figure 2.38a, showing the SCL results for the same US power and sonication time conditions. In fact, to the cells viability average values, which overcome 90% or even 100%, correspond negligible SCL intensities, meaning that a minimal amount of ROS is generated. Therefore, it is evident that the cavitation threshold was overcome for a so little amount that the applied sonication times were not sufficient to generate a detectable fraction of dead cells and blue intensity, or that the threshold itself was not reached.

In general, from the behaviour presented in Figure 2.38a and Figure 2.38b, the NPs resulted to not improve greatly the cavitation effects. To explain this evidence, it can be supposed that, since the generated cavitation was so weak, even its enhancement by NPs compared to the corresponding control samples was too low to be detected. On the other hand, the consistency of the results between the cells viability and SCL measurements, further highlights the adequacy of Luminol SCL experiments in indicating the amount of ROS generated.

In order to quantitatively find the concentration of generated ROS inside both the control and NPs-enriched solutions, treated with US, the most representative measurements among the previous ones were repeated by means of the more detailed EPR spectroscopy method. The related results are presented in Figure 2.38b, showing the applied experimental conditions (including the reference measurement) and the corresponding molar concentrations of hydroxyl radicals, each of them being the average value among four repeated measurements (n = 4). A clear monotonically increasing trend of the OH· radicals concentration as function of the sonication time and the US power is well distinguished (both with and without NPs), as it would be expected. Differently from the previous experiments, the amplification of cavitation effects thanks to the presence of NPs in the treated solutions is strongly manifested: for each US condition, a higher amount of OH· radicals was detected in the solutions containing NPs compared to the control solutions.
Therefore, thanks to the EPR measurements, quantitative results on the concentration of radicals produced during the solutions treatment is obtained as well as the influence of the synergistic action of US and NPs; however, the molar concentrations found are apparently not sufficient to induce the cells death and to provide a detectable SCL intensity.

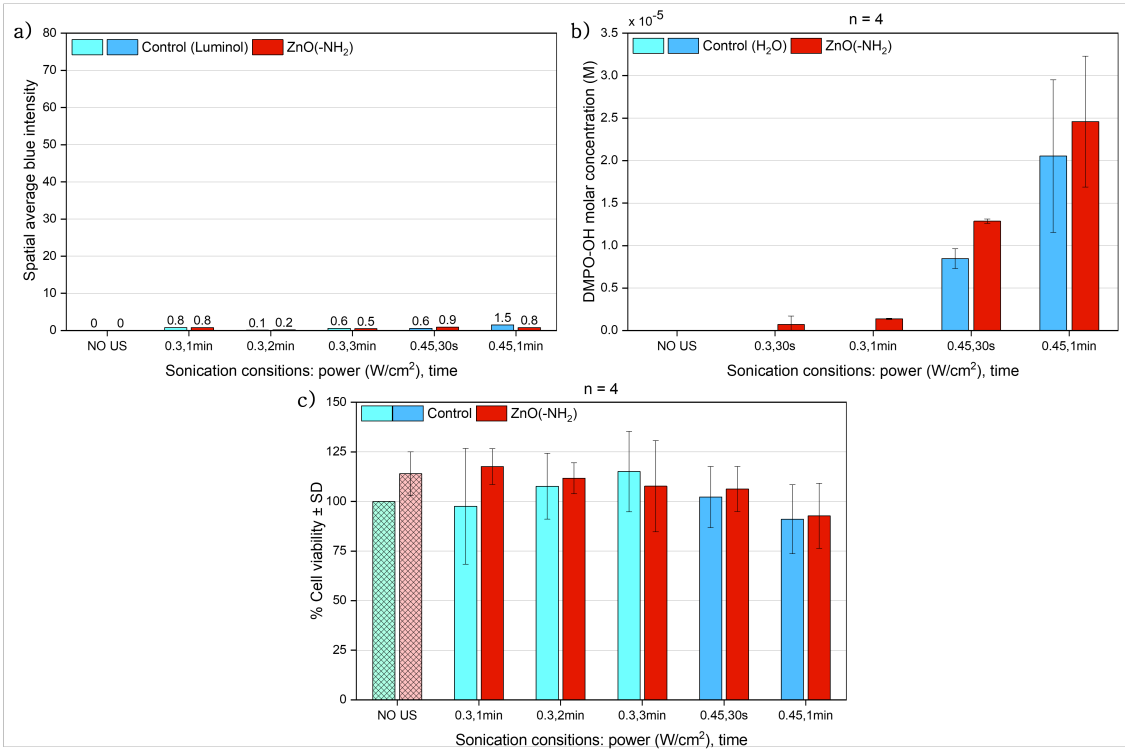

Figure 2.38: Comparison between control and NPs results concerning: a) cells viability, b) Luminol SCL and c) EPR spectroscopy.

Chapter 3

Second part - Cartridge

3.1 Introduction

The second part of the Thesis work focuses on the study and development of a cartridge specifically designed and fabricated to meet several requirements in various fields, regarding the specific fluid flow developed inside its channel, the effectiveness of the sonication of the solution and the constraints on its structure so to be successfully built through a light-based 3D printer.
This introductory part provides the basis for the subsequent results presentation, starting from the detailed description of the already employed Therakos® CELLEX® Irradiation Chamber, used as starting point for the cartridge design and proceeding with an insight of the fluid dynamic equations and properties, in particular concerning the Laminar flow. It follows an overview over the parameters used in COMSOL simulations, both for the fluid flow and for the acoustic wave propagation inside the cartridge.

3.1.1 Insight on the Therakos® CELLEX® Irradiation Chamber

As previously mentioned in 2, the technical description of the photoplate used in the Therakos® CELLEX® Photopheresis system for the UV treatment of leukocytes, is addressed in this second part of the Thesis work. In fact, the whole design and general characteristics of the photoplate, from the choice for the channels' particular shape to the material used for its fabrication, were the starting point and source of inspiration for the development of a new cartridge prototype more suitable for US excitation rather than UV light.

The technical details description of the first FDA approved photopheresis activation chamber is illustrated in the US Patent Number 4,737,140 [59], dating back to the year 1988, and presented in Figure 3.1, showing all its various components.

Following the pathway pursued by the buffy coat, consisting mainly of leukocytes and plasma, it is firstly delivered through the entrance line (**501**) to the inlet tubing **209**, thus entering within the irradiation chamber **513**. Then, the channel at the inlet gradually enlarges until the required width is reached and develops upwards showing a serpentine pathway **503**.
In particular, this chamber is properly designed to meet some requirements imposed both by the excitation source, UVA light, and also by the fluid circulation.
Concerning the first issue, the material employed in the fabrication of the photoplate should provide the transmission of UVA light through the material itself, allowing for the irradiation of the fluid beneath the chamber walls. For this reason, it is composed of two arranged parts: a male and female thin plates, that are sealed together. The selected material for this purpose is polycarbonate, thanks to its transparency to the wavelength of UVA radiation. In addition, since the UVA light is characterized by a low penetration depth, the cavity where the buffy coat flows from the bottom to the top of the cartridge, as marked by the arrows, is designed to maximize the surface area/volume ratio of leukocytes: in fact, the channel is relatively thin (approximately 0.04 inches, i.e. 1.02 mm) providing an expansion of leukocytes over the entire width of the channel and not along its thickness, therefore minimizing the self-shielding effects of the cells during irradiation.
On the other hand, regarding the buffy coat circulation inside the chamber, a serpentine shape of the channel is suitably chosen for the leukocytes in order to prevent stagnant areas of flow.

Once the fluid has traveled for the entire length of the channel, the buffy coat leaves the chamber from the outlet tube **511**, passes through the pump block **504** and is reintroduced in the initial reservoir through the return line **502**.
The motion of the fluid through the tubing system and the channel occurs thanks to the presence of a recirculation pump rotor **203**, which controls the flow by engaging the outlet tube **511** in the semi-circular tract **508**, thus creating a peristaltic flow inside the chamber. Finally, a shoulder **219** is introduced right before the pump block to avoid creeping of the outlet tube **511** during the pumping action.

Figure 3.1 also represents the arrangement of UV lamps **400** with respect to the serpentine pathway, while Figure 3.2 offers a top view of the two components: the irradiation chamber is inserted vertically in between the two light arrays, one for each of the two thin plate sections composing the photoplate. The suitable light sources consist in elongated and tube-shaped UVA fluorescent lamps, covering the entire transverse length of the chamber. This arrangement is adequately chosen to provide a constant and uniform irradiation over

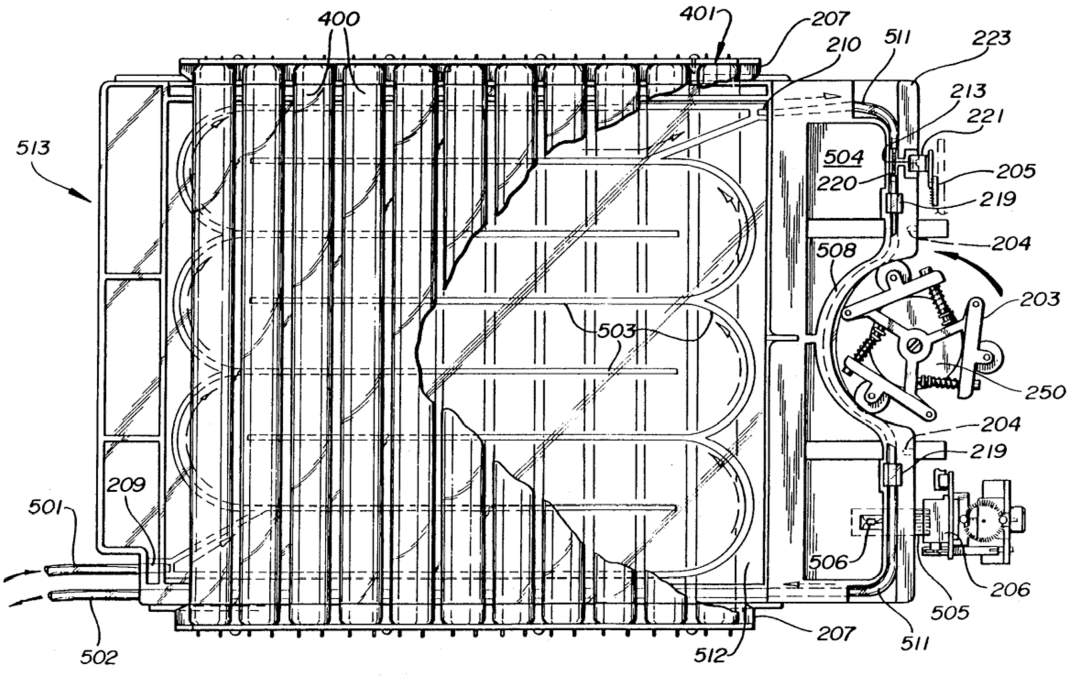

Figure 3.1: Front view of the photoplate irradiation chamber, with the recirculation pump and photoactivating light source arrays [59].

the whole chamber surface area and thus, over the entire cavity.

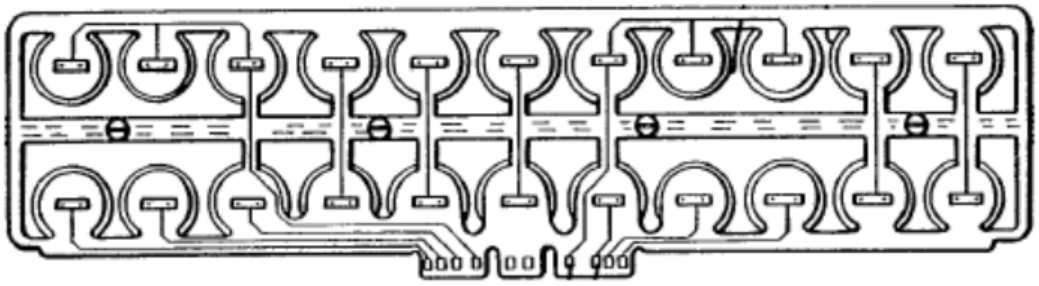

Figure 3.2: Top view of the photoplate irradiation chamber and photoactivating light source arrays (adapted from [59]).

From this first approved project, its design has been further developed and refined during the years, while maintaining always its original structure. In more recent years, a newer irradiation chamber described by the US Patent No. 2004/0143208A1 [60] has been approved, dating back to 2004.

As in the previous project, the photoplate is composed of a thin, large and sterile cavity, accurately designed to prevent the self-shielding effects, and where the buffy coat flows following a serpentine pathway, therefore again minimizing the stagnant areas. The chamber is fabricated by joining together a front and a back plates, made of a material transparent to UV light, as polycarbonate or also acrylic. The manufacturing includes an injection molding process to form the two plates, followed by a RF welding, a particular technique consisting in the clamping of the two components and the application of high-frequency electric fields providing the heating and melting of plastic-based materials. As the joint between the two parts solidifies, the clamping force is removed.
The irradiation chamber so accurately fabricated may have from 4 to 12 channels, although 8 channels is the preferred choice.
Finally, the photoplate is inserted with a vertical orientation in between the two banks of UVA lamps, irradiating the chamber from both sides, allowing for a 180 min UVA-exposure, leading to an average exposure per lymphocyte of $1 - 2\ J/cm^2$.
The irradiation chamber currently used by the Therakos® CELLEX® Photopheresis system is presented in Figure 3.3, having the following features: the thickness of each joined acrylic plate is 2 mm, while the cavity is 1 mm thick; considering that it is positioned having a vertical orientation, its height is of 25 cm and its width of 30 cm.

Figure 3.3: Current irradiation chamber of Therakos® CELLEX® Photopheresis system.

3.1.2 Fluid dynamics and properties

During the design of the cartridge, an important characteristic that should be carefully considered is the fluid flow inside the channel, in order to prevent stagnant or too much turbulent areas that would have detrimental effects during the treatment of cells.

Before setting the parameters for the fluid flow simulations, the intrinsic nature of the flow should be discussed. For this purpose, a useful dimensionless number able to describe the main properties, such as regime, stability and dominant effects of the flow is employed, known as the Reynolds number, introduced for the first time in 1883 by Osborne Reynolds. This number measures the relative importance between inertial effects, coming from the movement of a mass, as velocity and density, and viscous effects, accounting for the reaction of the fluid to the motion. It may be expressed as:

$$Re = \frac{\rho\ U\ L}{\eta} \tag{3.1}$$

where ρ is the density of the fluid, U is the average velocity, η is the dynamic viscosity and L is a characteristic dimension that depends on the internal features of the channel: if it is circular, L represents the internal diameter, while for any other non-circular shape, the hydraulic diameter should be calculated as:

$$D_h = \frac{4 \times Area}{Perimeter} \tag{3.2}$$

The Reynolds number indicates the regime of the flow depending on its value [61]:

1. $Re \leq 2300$ corresponds to a Laminar flow
2. $2300 \leq Re \leq 4000$ corresponds to a Transient flow
3. $Re \geq 4000$ corresponds to a Turbulent flow

However, since the Reynolds numbers found for all the cartridge prototypes are far below the value of 2300, the fluid flow inside the channel is assumed to be in a laminar regime.

The equation governing a laminar fluid flow can be derived by simplifying, with the right set of assumptions, the well known Navier-Stokes (N-S) equation.
In particular, the description of the N-S equation occurs within the Eulerian frame, also called laboratory frame, in which a specific volume of space where the fluid is flowing is selected, monitoring its evolution over time. In this way, the fluid is represented as a vector field composed of different and parallel streamlines, sliding on each other. This description differs from the Lagrangian frame, that, instead of a fixed volume, it considers specific fluid

particles and follows their trajectories inside the fluid. However, this last method prevents the knowledge of average quantities describing the fluid, since the information is restricted to the specific studied fluid particles.
Furthermore, the N-S equation results from the combination of two important laws: the conservation of mass and the second Newton's Law, as explained below:

1. On one hand, the conservation of mass is described by the continuity equation for a fluid in continuum, whose expression is:

$$\nabla \cdot (\rho_m \cdot \mathbf{u}) = -\frac{\partial \rho_m}{\partial t} \tag{3.3}$$

   where ρ_m is the mass density and $\mathbf{u}$ is the vector field velocity. The corresponding equation in the Eulerian frame becomes:

$$\frac{D\rho_m}{Dt} + \rho_m \nabla \cdot \mathbf{u} = 0 \tag{3.4}$$

   that represents the time rate of change of mass in a fixed volume in which the fluid is flowing.

2. On the other hand, the second Newton's Law can be written as:

$$\frac{d\mathbf{p}}{dt} = \sum \mathbf{F}_i \tag{3.5}$$

   where $\mathbf{p}$ is the linear momentum and $\mathbf{F}_i$ are the different forces acting on the fluid. These forces can be both surface forces, such as net shear forces acting tangentially to the fluid, the net pressure forces between the system and the environment acting normal to the fixed volume surface, and also volume forces, for example gravity.

After the necessary mathematical operations and the conversion of the second Newton's Law into the Eulerian frame, the final Navier-Stokes equation can be expressed with the following terms:

$$\rho_m \frac{D\mathbf{u}}{Dt} = -\nabla P + \rho_m \mathbf{g} + \eta \nabla^2 \mathbf{u} + \frac{\eta}{3} \nabla (\nabla \cdot \mathbf{u}) \tag{3.6}$$

This equation accounts for the mass conservation in the left-hand side and describes the fluid in the presence of pressure (P), gravitation ($\mathbf{g}$), and both external and internal viscosity (η) respectively. While the external shear forces are established between the fluid and the boundaries of the channel, the internal ones derive from the friction between the different streamlines sliding on each other within the fluid.

From the N-S equation obtained above, the Laminar flow description may be found by considering the incompressible N-S equation, assuming the time rate of change of the mass density (ρ_m) to be negligible:

$$\frac{D\rho_m}{Dt} = 0 \tag{3.7}$$

This assumption has two main consequences: the first one is related to the mass conservation,

$$\frac{\cancel{D\rho_m}}{\cancel{Dt}} + \rho_m \nabla \cdot \mathbf{u} = 0 \longrightarrow \nabla \cdot \mathbf{u} = 0 \tag{3.8}$$

meaning that the fluid is solenoidal, and therefore the number of streamlines entering within the fixed volume is equal to the number of streamlines exiting from it, providing no new sources inside the volume.
The second consequence is that the last term in the N-S equation regarding the internal friction can be neglected, implying that once the velocity profile is established, it remains the same, and the interaction between the different streamlines is not considered. Finally, the equation describing an ideal laminar fluid flow, characterized by no internal friction, can be written as:

$$\rho_m \frac{D\mathbf{u}}{Dt} = -\nabla P + \rho_m \mathbf{g} + \eta \nabla^2 \mathbf{u} + \cancel{\frac{\eta}{3} \nabla (\nabla \cdot \mathbf{u})} \tag{3.9}$$

also expanded as:

$$\rho_m \left(\frac{\partial \mathbf{u}}{\partial t} + \mathbf{u} \cdot \nabla \mathbf{u}\right) = -\nabla P + \rho_m \mathbf{g} + \eta \nabla^2 \mathbf{u} + \cancel{\frac{\eta}{3} \nabla (\nabla \cdot \mathbf{u})} \tag{3.10}$$

At this point, a further consideration should be taken into account: the fluid motion inside the channel of the cartridge is induced thanks to the presence of a peristaltic pump, responsible for the generation of a pressure-driven fluid flow. As a consequence, in addition to the assumptions made for a laminar fluid flow, a uniform pressure gradient along the channel's length (x direction) is considered to accurately describe the flow and it can be written as follows:

$$\frac{dP}{dx} = -K \tag{3.11}$$

where K is a constant describing the pressure gradient, with a negative sign since the high pressure region is assumed to be at the inlet while the low pressure region is at the end of the channel, causing the pressure to decrease along the x direction. Moreover, to further simplify the description, the flow may be assumed to have already passed the entrance area of the channel where the velocity profile is not yet completely established, meaning that the flow is considered to be fully developed, in a steady-state regime. The development or entrance length can be calculated through the expression:

$$L_d = \frac{D_h}{16} Re \tag{3.12}$$

where D_h is the hydraulic diameter for non-circular shaped channels and Re is the Reynolds number.
After the length L_d, the condition regarding the steady-state assumption can be expressed as:

$$\frac{\partial \mathbf{u}}{\partial t} = 0 \tag{3.13}$$

stating that there is no more acceleration of the fluid and thus, no inertia. The N-S equation for the fluid flow therefore becomes:

$$\eta \nabla^2 u = -K \longrightarrow \nabla^2 = -\frac{K}{\eta} \tag{3.14}$$

leading to a parabolic behaviour of the velocity profile (as shown in Fig.3.4), characterized by no-slip boundary conditions, meaning that the velocity in correspondence to the channel walls is zero, $\mathbf{u} = 0$. Figure 3.4 represents the velocity profile in a 2D model, whose average velocity may be found as:

$$u_{average} = \frac{Q}{Wh} = \frac{2}{3} u_{max} \tag{3.15}$$

where Q is the flow rate imposed by the peristaltic pump, W is the width of the channel and h is its height.

3.1.3 COMSOL simulations of the fluid flow

The entire discussion of the fluid dynamics and equations presented above serves as starting point for the COMSOL simulations description, consisting in several steps.
For this purpose, at first, the required flow model is selected by choosing the single phase flow and, consequently, the laminar flow COMSOL interfaces [62]. After that, the stationary study method is set, in order to simulate an already developed, time-indipendent and steady-state fluid flow, thus implementing the properly simplified Navier-Stokes equation. The selected domain representing the channels inside the cartridges is not built inside the COMSOL software due to the complexity of the geometry. Therefore, the specific CAD project of each cartridge prototypes is firstly designed using SOLIDWORKS software and then, thanks to an appropriate link between the two softwares, it has been possible to load directly the CAD project from SOLIDWORKS to COMSOL Multiphysics.

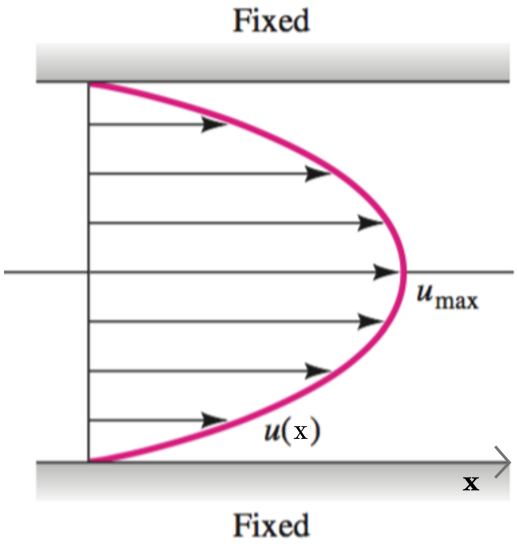

Figure 3.4: 2D velocity profile of a pressure-driven flow.

Once that the domain is designed, the required material has to be selected. As already done in the analysis of the single wells, the domain is considered to be an isolated system, completely composed of water, whose material-related parameters, such as the density and viscosity are set in the simulation.

Then, the analysis is carried on by setting specific boundary conditions and domains. The fluid flow is set to be incompressible and the *Wall property* is considered to be no-slip, thus implementing the zero velocity at the boundaries of the N-S equation for a laminar flow. Then, it is necessary to select an inlet surface from the already built domain, having an associated boundary condition: since in the experimental laboratory set-up, a peristaltic pump is employed, able to provide a certain output flow rate Q, the same value is inserted as inlet boundary condition in the simulation. Differently, outlet boundary condition is chosen to be the pressure, set at zero, $p_0 = 0\ Pa$, in order to simulate the pressure gradient along the length of the channel. Finally, the particular mesh used for these fluid flow simulations is a physics-controlled mesh with fine element size [61].

3.1.4 COMSOL simulations of the acoustic wave

Since an other important requirement that the cartridge should meet is the ability to transmit the acoustic wave generated by the transducer, providing an effective sonication of the solution inside the channels, also the acoustic wave propagation needs to be simulated.

In this case, the general structure of the simulation as well as the selected parameters are exactly the same of the already established acoustic field pressure and intensity simulations employed for the single wells. The only modifications made concern the geometry of the domain, imported from the SOLIDWORKS software as in the fluid simulations procedure, and the mesh employed. In fact, in order to make a comparison between the acoustic intensity and pressure values inside the cartridge and the wells, the mesh is similar to the one exploited for the single wells: a *Mapped* mesh is imposed on the bottom surface and then, expanded over the whole domain through the *Swept* command. However, due to the complexity of the cartridge geometry, the simulations were too computational demanding; therefore, the minimum size of the mesh has been increased from $\lambda/10$ to $\lambda/9$, while the maximum element size from $\lambda/8$ to $\lambda/5$, so to reduce the total number of degrees of freedom that are calculated during the simulation (Fig. 3.5).

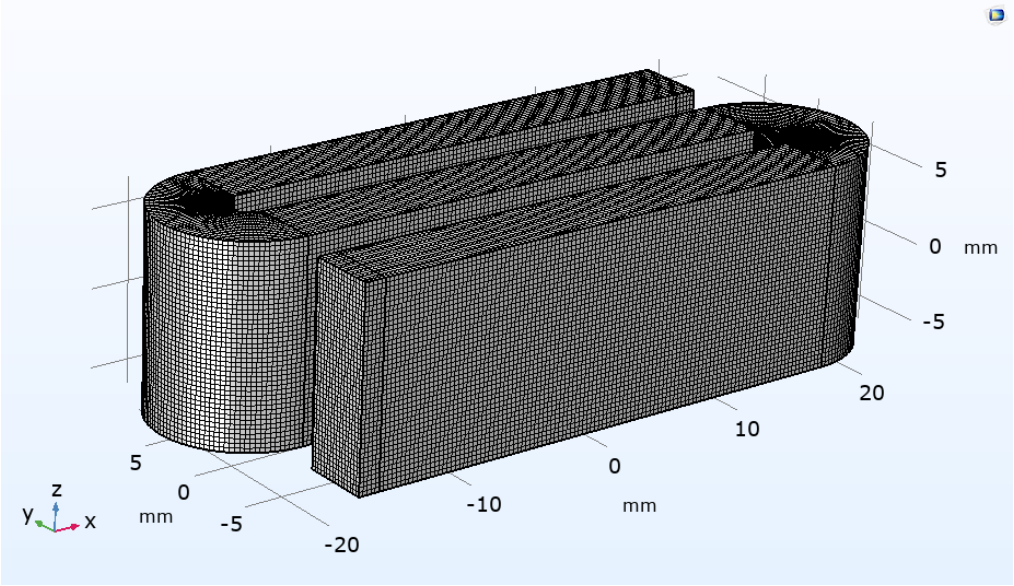

Figure 3.5: Cartridge mesh for the acoustic wave propagation simulation.

3.1.5 3D printing method

Once that the most suitable cartridge design is chosen, able to meet fluidic, acoustic and printing requirements, the sonication chamber is fabricated through a 3D light-based printing technique, known as Digital Light Processing (DLP), described in the work of González et al. [63].

This printing method is a vat polymerization technique that provides the printing of 3D objects through photopolymerization in a layer-by-layer fashion (Figure 3.6). Thus, the initial 3D CAD projects of the cartridges are loaded and divided in thin horizontal layers. Then, a LED light source (405 nm) is directed towards the surface of a Digital Micromirror Device (DMD), composed of thousands of moving micromirrors able to switch between on and off positions [64]: thanks to the particular orientation of each micromirror, the light is reflected in order to recreate the same pattern of a selected layer of the original cartridge design on the surface of a resin. Under the LED light illumination, this thin layer of the resin or liquid polymer solidifies on the exposed area, forming the first layer of the final 3D structure. At the end, the sample holder move upwards of a single step, corresponding to the thickness of a layer, letting the liquid polymer to fill the space underneath and to be cured by light. After that, the procedure is repeated several times until the final 3D object is completely built layer-by-layer.

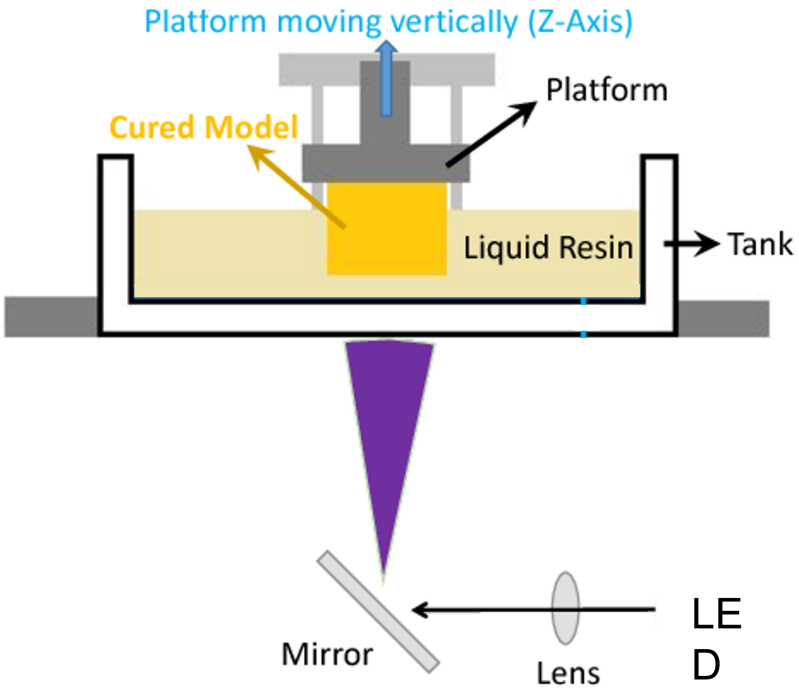

Figure 3.6: DLP working principle.

Since the major properties that the cartridge should satisfy are a certain degree of transparency, and most of all, the biocompatibility, Polyethylene glycol diacrylate (PEGDA, M_n = 250 g/mol) is selected as the most suitable material for the printing process [65], [63].

The diacrylate reactive monomer PEGDA is mixed together with a certain quantity of Phenyl bis(2,4,6–trimethylbenzoyl)-phosphine oxide (BAPO) employed as photoinitiator, giving the ability to the polymeric formulation to solidify under light exposure [63].
After the printing of the cartridge, to increase the cytocompatibility, the cartridge may undergo a deep washing procedure in acetone or ethanol for the complete removal of unreacted products.

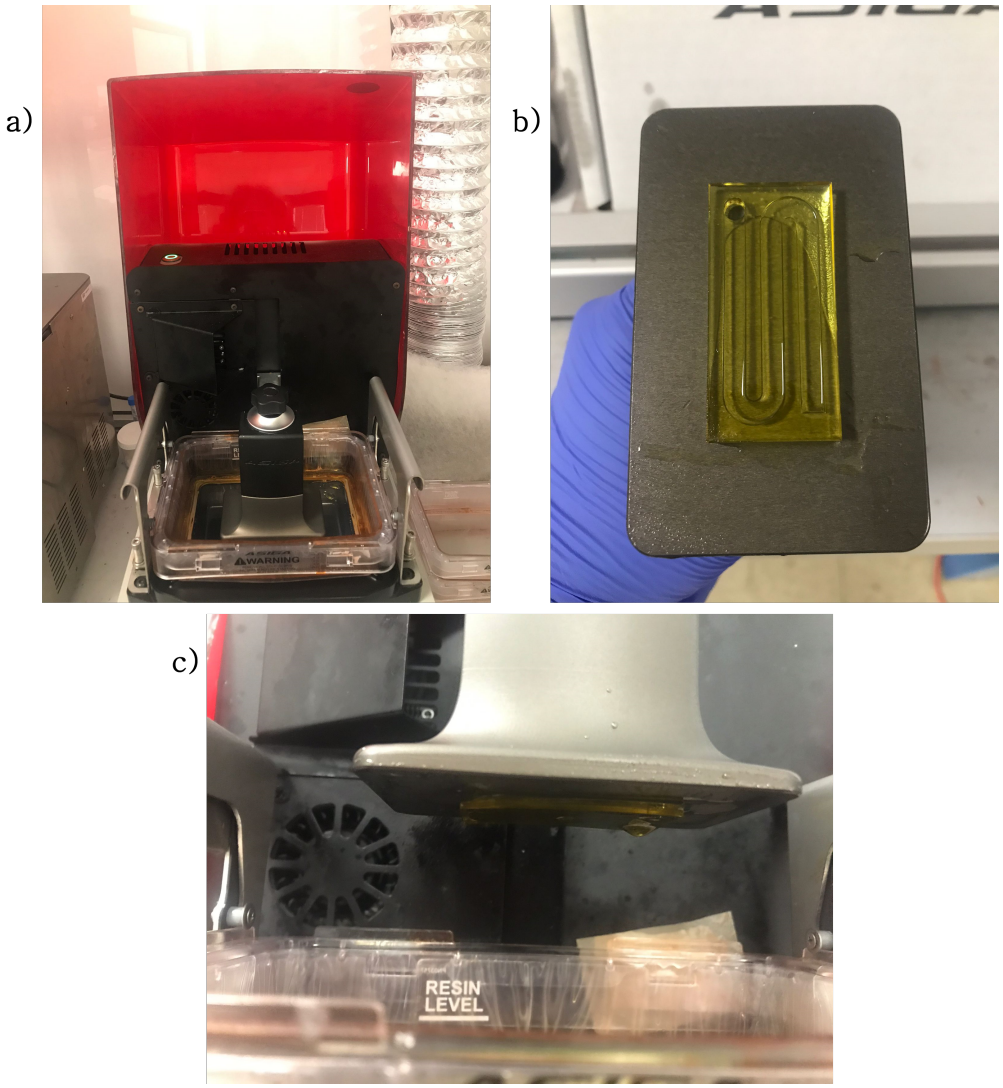

Figure 3.7: DLP printing device: a) top view of the sample holder and of the tank containing the liquid resin, b) cartridge soon after the printing process is ended and c) lateral view of the system, with the cartridge attached upside-down on the surface of the sample holder, in front of the liquid resin.

3.2 Preliminary design study of the cartridge

3.2.1 Preparatory cartridge design

The very first design of a cartridge prototype was thought to have similar structure and characteristics to the irradiation chamber already employed by Therakos®.
In order to prevent stagnant areas of flow during the circulation, it was composed of three parallel and longitudinal channels forming a serpentine pathway (Figure 3.8), whose cross-setional area gradually decreases when approaching the inlet and outlet apertures. This expedient was introduced to prevent or at least, to minimize the turbulence of the flow that can occur at the entrance and exit of the entire channel. In this first project, the inlet and outlet openings protrude outwards from the central structure, having an internal diameter $d_{int-car} = 4.5\ mm$ slightly smaller than the external diameter of the tubes that would be inserted, providing a connection between the cartridge and the peristaltic pump. The tubes considered for the laboratory experiments are from the Therakos® Photopheresis system, with an external diameter $d_{ext-Ther} = 4.6\ mm$.

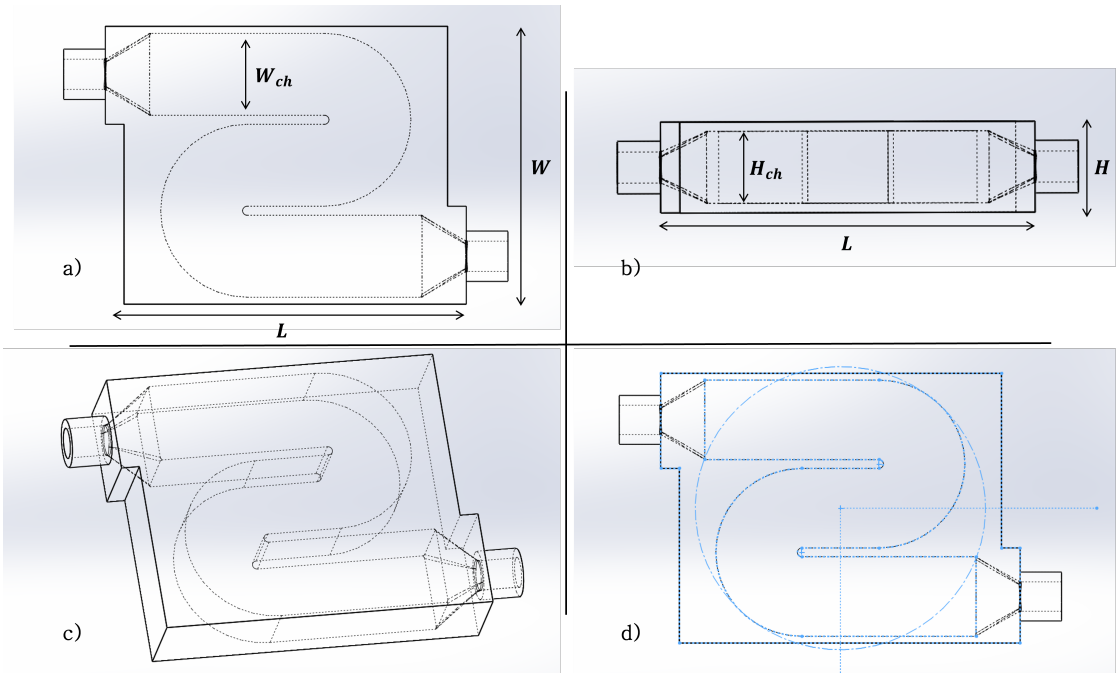

Figure 3.8: CAD project of the first cartridge: a) top view, b) side view, c) lateral view and d) top view with the circular shape of the Lipozero transducer.

On the other hand, differently from the Therakos® photoplate whose thickness is limited by the low penetration depth of UVA light, thus intrinsically requiring a large and thin

channel, with the use of US waves as external excitation, this condition is not necessary. In fact, acoustic waves are able to deeply penetrate into various media and, for this reason, the thickness of the entire channel can be increased from 1 mm of the irradiation chamber to several mm for the sonication chamber.
Lastly, since the final use of the cartridge includes its positioning on the transducer surface to provide the sonication of the solution, the whole project was designed to cover the largest possible disposable area on the US transducer. For this reason Fig. 3.8d represents also the surface of the circular LipoZero transducer, having a radius $r = 21{,}00\ mm$ upon which the cartridge would be placed. To summarize, some significant features of this project are listed in the Table 3.1.

Parameters	**Values**	**Description**
W	40 mm	Width of the cartridge
L	42 mm	Length of the cartridge
H	12.6 mm	Height of the cartridge
W_{ch}	11.8 mm	Width of the channel
L_{ch}	100.67 mm	Length of the channel
H_{ch}	10 mm	Height of the channel
$t_{top,bottom}$	1.3 mm	Thickness of the walls at the top and bottom
Total Volume	11.88 mL	Maximum volume

Table 3.1: Parameters of the first cartridge project.

3.2.2 Second cartridge design

At the same time, in order to explore different possible configurations, a cartridge consisting of five channels is designed by reducing the width of the entire serpentine pathway ($W_{ch} = 7.6\ mm$) and adding two more turns to the entire channel, as shown in Figure 3.9. In this project, since the height of the channel is increased ($H_{ch} = 15\ mm$), the gradual decrease of the cross-sectional area for the connection to the inlet and outlet apertures is designed to be longer. Neverthless, due to the large number of channels that need to fit within the transducer surface area, the three channels configuration was preferred.

Finally, due to the complexity of the design of both three and five channels, the large dimensions of the entire cartridge structure, and the too small thickness chosen for the upper and lower walls as well as for the lateral boundaries, the very first design was abandoned and a new cartridge project able to meet the printing requirements was considered.

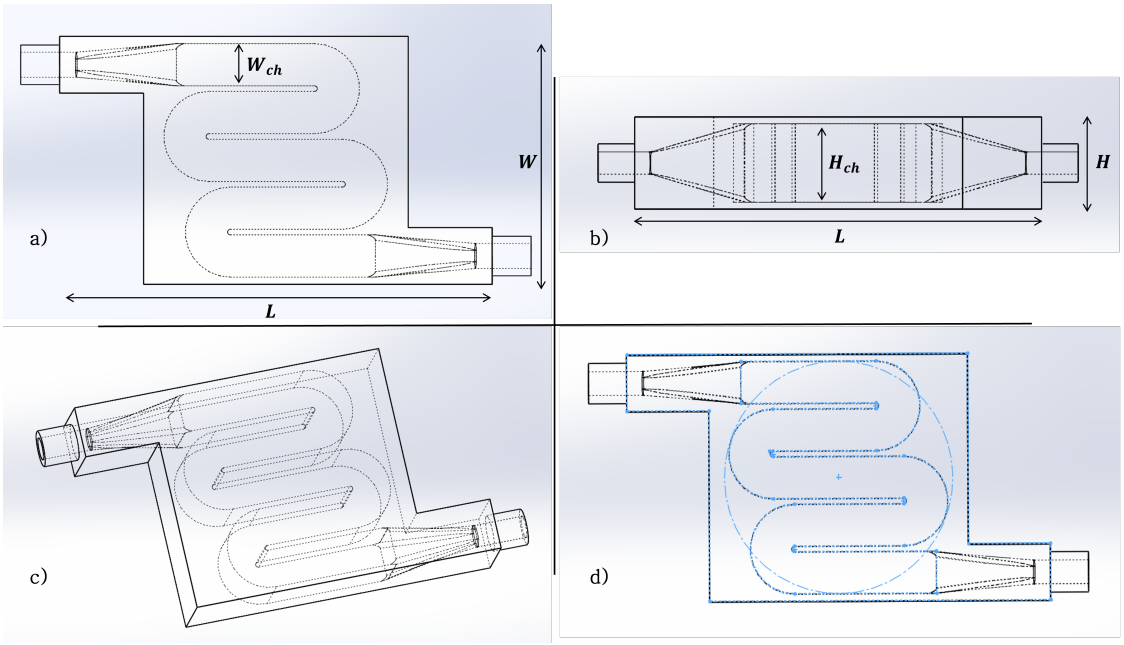

Figure 3.9: CAD project of the five channels cartridge: a) top view, b) side view, c) lateral view and d) top view with the circular shape of the Lipozero transducer.

3.2.3 First printed cartridge prototype

The design of the new cartridge version, after adjustment made also considering the 3D printing requirements, is presented in Figure 3.10: it shows a certain difference in the channel structure, whose serpentine-like path develops along the length of the cartridge, characterized by narrow channels. The choice of this particular project was made in order to fulfill the lower limit dimension that can be printed, equal to 3 mm. Therefore, all the cartridge walls, including the lateral ones, the separation between the channel's turns and the basis at the bottom of the structure were thickened, to prevent the collapse of some parts and to provide a major stability and robustness of the cartridge during the printing process. Furthermore, also the width (W) of the cartridge is decreased to force it within the maximum printable surface area.
Differently from the previous designs, the inlet and outlet apertures fall within the dimensions of the structure in order to provide the required robustness both during the printing steps and also during the use of the device, avoiding possible collapse or breaks when the Therakos® tubes are inserted. The associated holes are 5 mm deep and 4.5 mm wide, allowing for an effective interlocking of the tubes inside the two openings.

Finally, the cartridge was printed without the upper cover, permitting laboratory experiments without the presence of a lid. Only in a second moment, a thin glass used for microscopy purposes was applied to seal the top part by pouring a layer of PDMS. Table 3.2 resumes all the major parameters involved in its design.

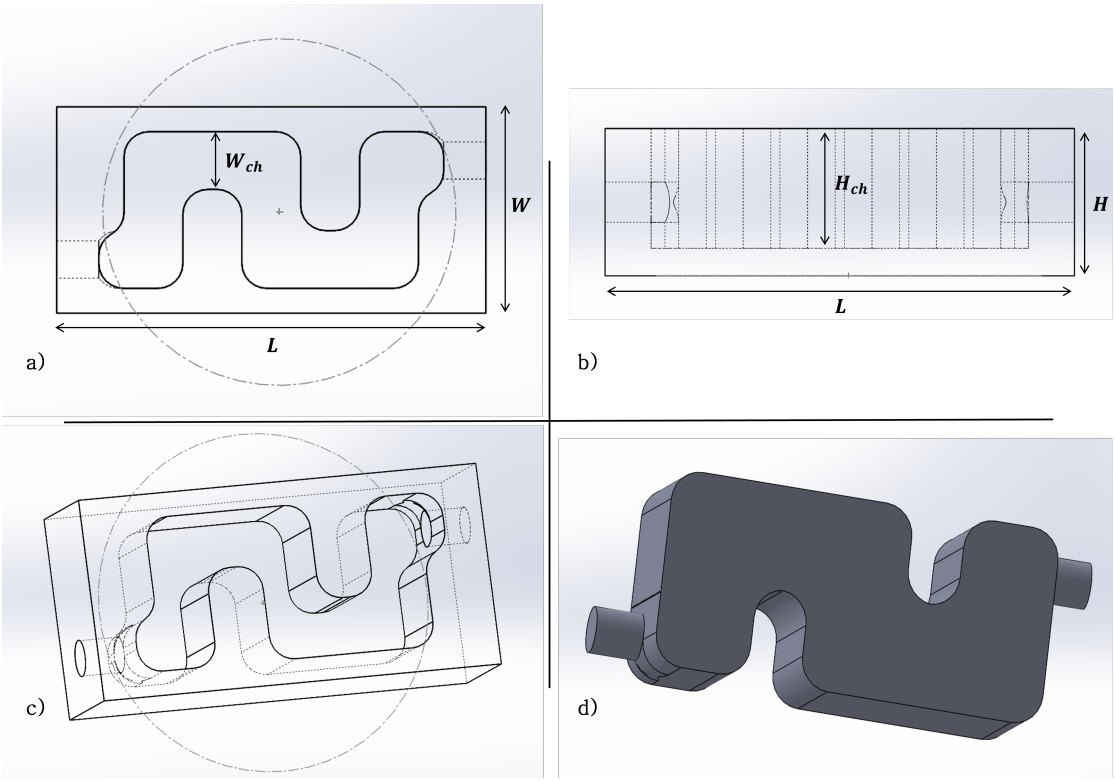

Figure 3.10: CAD project of the first printed cartridge: a) top view, b) side view, c) lateral view and d) project used as COMSOL simulation domain.

Parameters	Values	Description
W	25 mm	Width of the cartridge
L	51 mm	Length of the cartridge
H	16 mm	Height of the cartridge
W_{ch}	7 mm	Width of the channel
L_{ch}	77 mm	Length of the channel
H_{ch}	13 mm	Height of the channel
$t_{lateral,bottom}$	3 mm	Thickness of the walls and of the basis
Total Volume	7.0 mL	Maximum volume

Table 3.2: Parameters of the first printed cartridge project.

Figure 3.11 shows the final printed cartridge, having a general yellowish colour, that does not prevent to provide the required transparency in correspondence to the bottom layer.

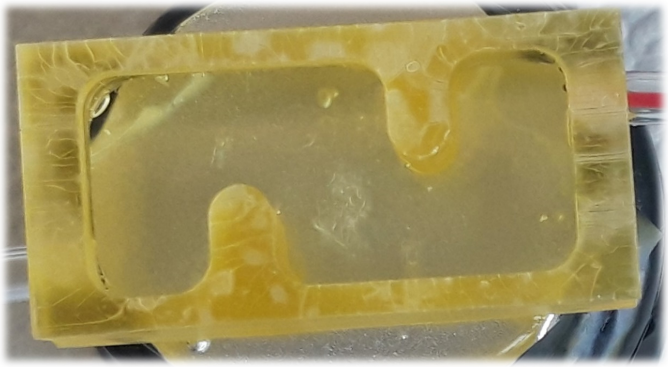

Figure 3.11: 3D printed cartridge.

COMSOL simulations

Since the fluid flow of this cartridge was the first to be simulated, it laid the foundations for all the successive flow simulations.

The Reynolds number associated to this particular channel structure is found by assuming the maximum possible flow rate that can be selected through the peristaltic pump in a laboratory set-up, equal to $Q = 17.47\ mL/min$.

By referring to the previously presented expressions, the average velocity is calculated from the flow rate as:

$$u_{ave} = \frac{Q}{W_{ch} H_{ch}} = 3.2 \ \frac{mm}{s} \tag{3.16}$$

After that, the hydraulic diameter is found:

$$D_h = \frac{4 \times W_{ch} H_{ch}}{2(W_{ch} + H_{ch})} = 9.1 \ mm \tag{3.17}$$

leading to the final expression of the Reynolds number:

$$Re = \frac{\rho \, U D_h}{\eta} = 32.65 \tag{3.18}$$

where $\rho = 998 \ Kg/m^3$ is the water density and $\eta = 8.9 \cdot 10^{-4} \ Kg/(m \cdot s)$ is the water dynamic viscosity.
Since the Reynolds number was found to be lower than 2300, the flow is described by a laminar regime.

Once all the simulation parameters related to the laminar flow are set in COMSOL software, a specific mesh is built on the whole domain, shown in Figure 3.12.

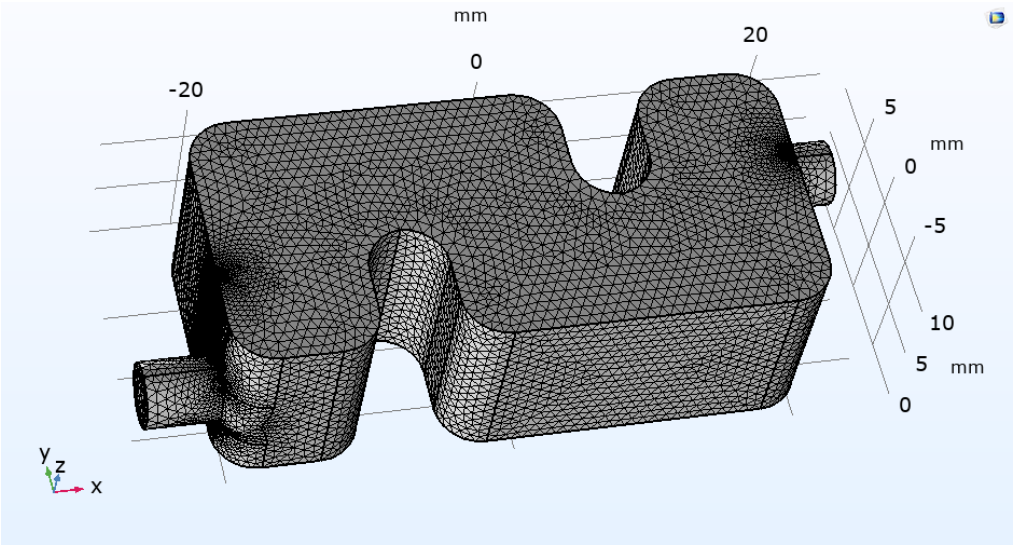

Figure 3.12: Particular mesh implemented for the fluid flow simulation.

Figure 3.13 obtained from the fluid flow simulation represents the velocity magnitude distribution along the channel. In correspondence to the inlet (right side) and outlet (left

side) the velocity results to be higher, reaching also the maximum value of $u_{max} = 38\ mm/s$ at the inlet. However, except for these two regions, the velocity magnitude tends to have much lower values, consistently to the previously calculated mean velocity, found to be $u_{ave} = 3.11\ mm/s$. Besides, it should be noticed that the plane cutting horizontally the domain is in-plane with the height of the inlet and outlet apertures, thus showing a certain high velocity. However, by looking at the vertical planes, the velocity magnitude at the inlet rapidly decreases when considering different heights (z values) that are not aligned with the inlet hole. A similar situation occurs also in correspondence to the outlet, but the difference in velocity magnitude between the central region and the surrounding one is lower due to a decreased velocity value at the outlet.

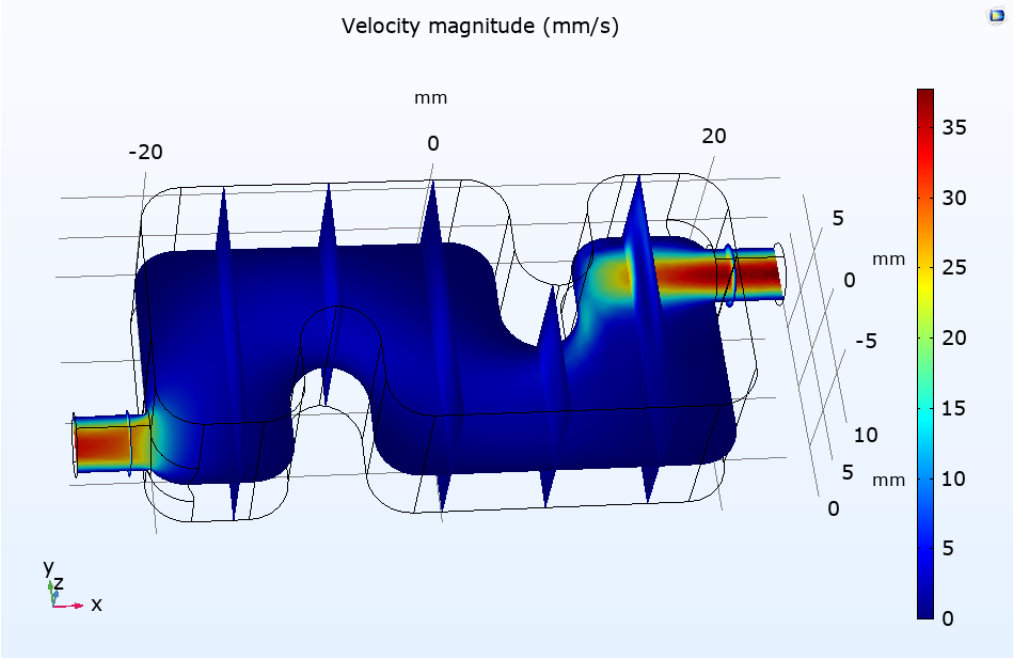

Figure 3.13: Velocity magnitude distribution along the channel.

As a consequence, a proper investigation on the behaviour of the velocity in the blue regions, characterized by the lowest values, should be carried on in order to discover possible turbulent or stagnant areas. For this purpose, the velocity streamlines are plot (Fig. 3.14, thus highlighting the velocity vector and not only its magnitude. Anyway, the colors of the ribbons represented in the streamlines plot are associated to the magnitude.

From these results, it can be noticed a certain turbulence of the flow, mainly occurring at the inlet region. In fact, since the fluid enters within the channel with a relatively high

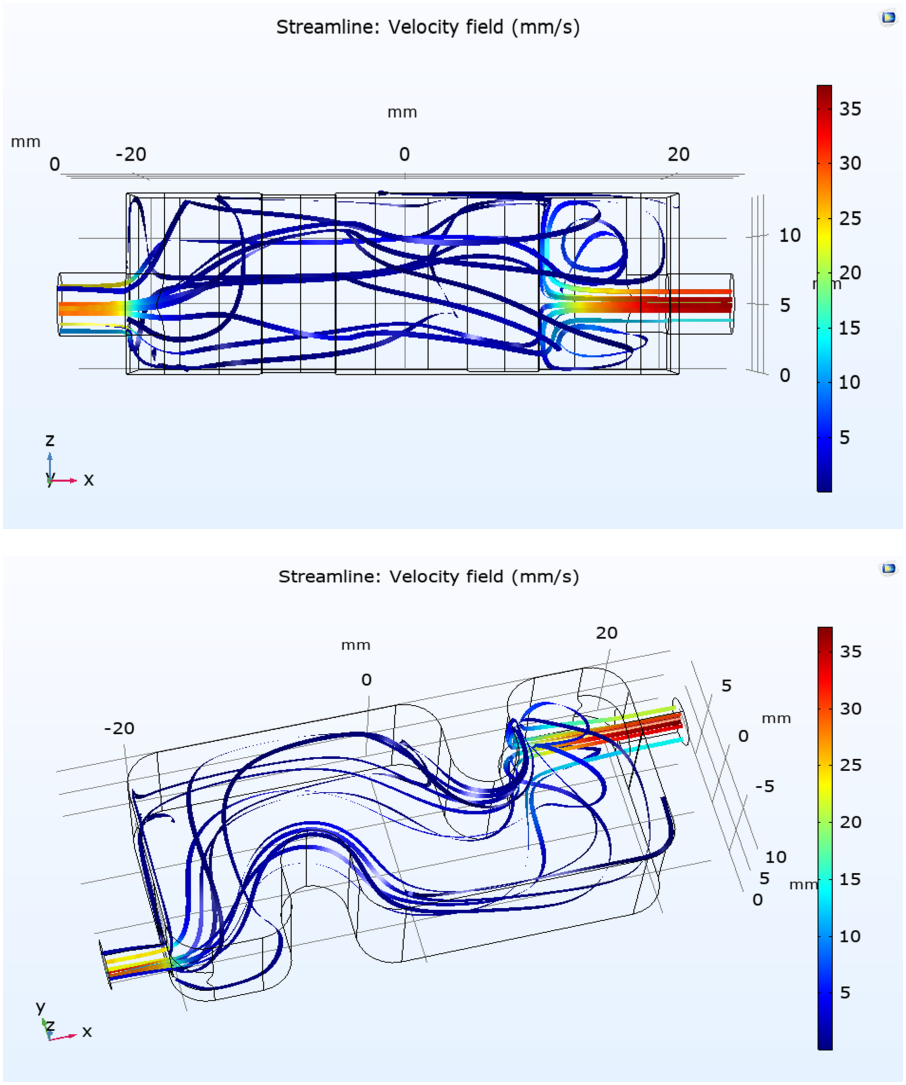

Figure 3.14: Velocity Streamlines: side view (top) and lateral view (bottom).

velocity and soon encounters the wall of the serpentine-like pathway, it tends to return back, generating a turbulent region. As the fluid moves beyond this area, the flow proceeds smoothly until the outlet region is reached. However, in this case, the turbulence noticed remains less significant than the inlet one.

Experimental results

In order to investigate the resistance and robustness of the PEGDA solid material when subjected to the ultrasounds, the cartridge is positioned with a thin layer of coupling echographic gel upon the US transducer to test it under different sonication conditions (Figure 3.15). PEGDA is tested both with and without water within to identify possible differences in the two conditions. Since the cartridge will be employed with cells and blood, the most US powers of interest are the lower ones, such as 10%, 15%, 20% and, at least, 30%. These ultrasound intensities are maintained for various time periods, as 1 min, 2 min and 3 min.
The cartridge has demonstrated an effective structural resistance during the experiments since neither delamination nor heating of the system were observed for the considered powers in both cases (with and without water).

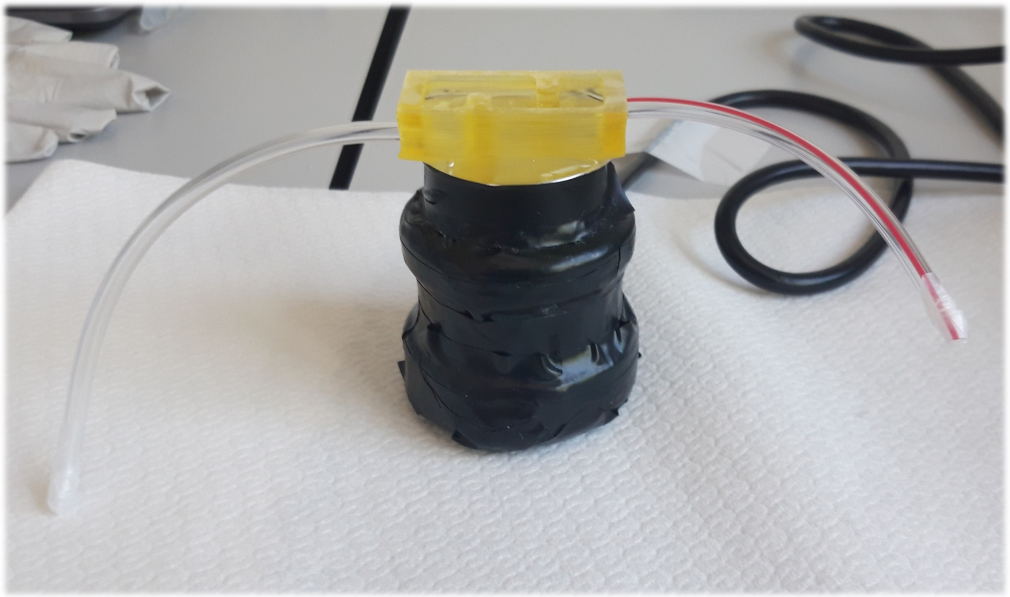

Figure 3.15: Test of the PEGDA cartridge structural robustness.

After the testing of its structural features, the cartridge fluidic properties are investigated. To this aim, the cartridge is connected to the tubes passing through a peristaltic pump, whose flow rate is set to its maximum value, equal to $Q = 17.47\ mL/min$.
In the experimental set-up, shown in Figure 3.16, a specific tube of the peristaltic pump is immersed on one end inside a beker containing double-distilled water, while on the other end it is connected to the Therakos® tube through a parafilm layer tightly wrapped around. Then, the Therakos tube is stuck at the inlet of the cartridge, while another identical tube

is positioned in correspondence of the outlet, ending up in a becher that collects the double-distilled water at the end of the circuit. Therefore, when the peristaltic pump is activated, the double-distilled water is removed from the original beker, passes through the pump and the Therakos® tubes, arriving at the cartridge. When the water reaches a certain level inside the channel, it flows outside the cartridge through the outlet tube.

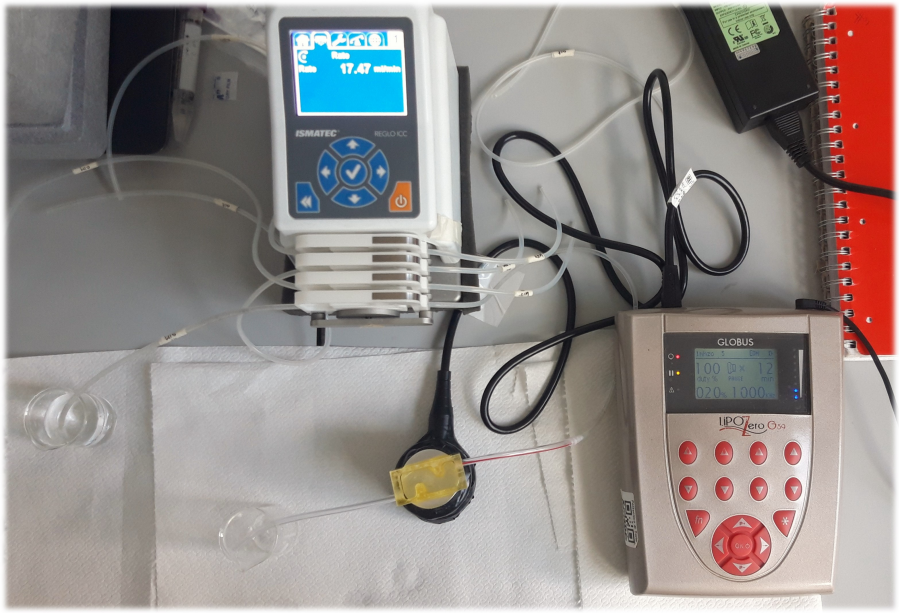

Figure 3.16: Experimental set-up arranged for the study of the fluid flow.

Two different conditions are taken into account: in the first one, the cartridge is completely empty and it is gradually filled with water through the pumping system; in the second situation, the cartridge is already partially filled with water in order to study the fluid flow in a condition closer to the real one. As it would be difficult to investigate the fluid circulation only using water, a few drops of ink are added in the initial beker, mixing it with water.

As demonstrated by Figure 3.17, the COMSOL simulations of the fluid flow are consistent with the experimental results obtained in the real set-up. In fact, when the fluid enters within the cartridge, it directly encounters the channel wall perpendicular to its direction, causing it to be deviated backwards or laterally with a certain degree of turbulence, highlighted by the ink distribution. Once the fluid crosses this first region, the flow becomes smoother, directing towards the outlet from which it is expelled. However, it is possible to notice some areas where a subtle stagnant flow is visible, as in the two final corners close

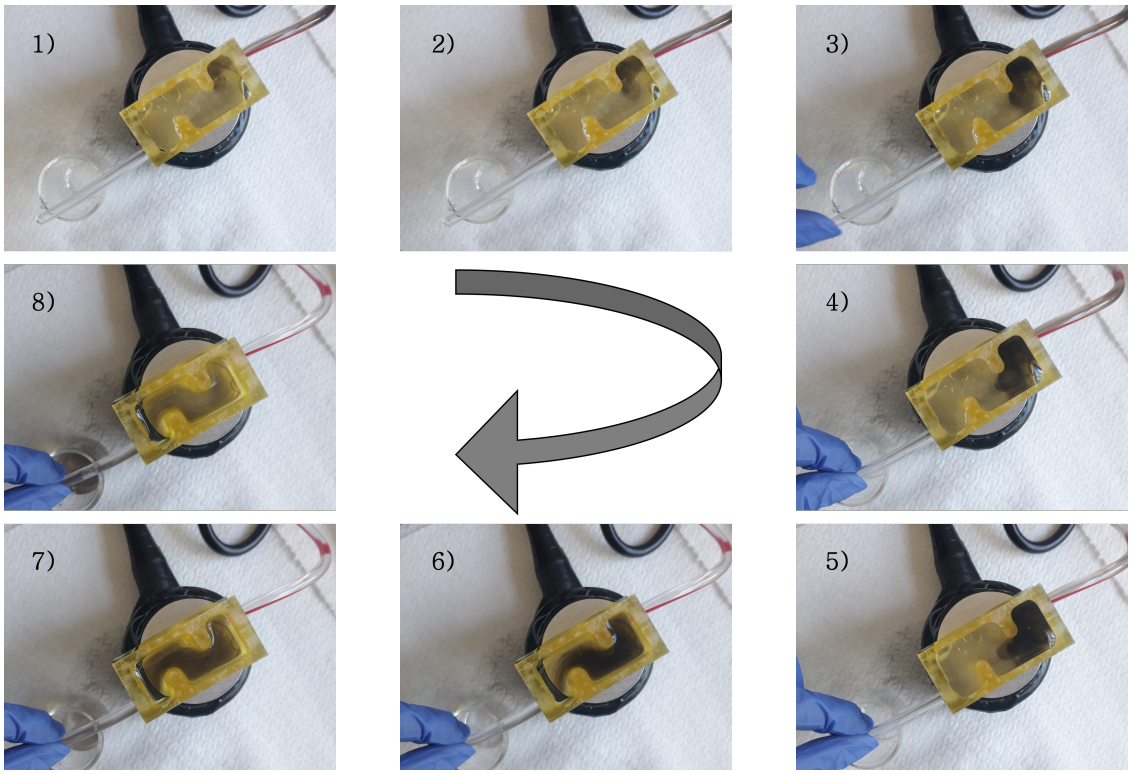

Figure 3.17: Sequence of images acquired during the flow of water and ink in a cartridge already filled with water.

to the outlet.

A different behaviour of the fluid flow is obtained when the cartridge is initially completely empty and then filled by the incoming mix between water and ink. As shown in Figure 3.18, the fluid follows the path of the channel's serpentine without exhibiting an appreciable turbulence. Even if the fluid circulation does not seem to occur as the simulations are predicting, this is also consistent with the COMSOL simulations themselves in which the flow is assumed to be completely developed, in a steady-state condition, while in this case the flow changes over time as the cartridge is gradually filling with water. Indeed, when the water level inside the channel increases, a certain turbulence becomes to appear, with a trend similar to the previous case.

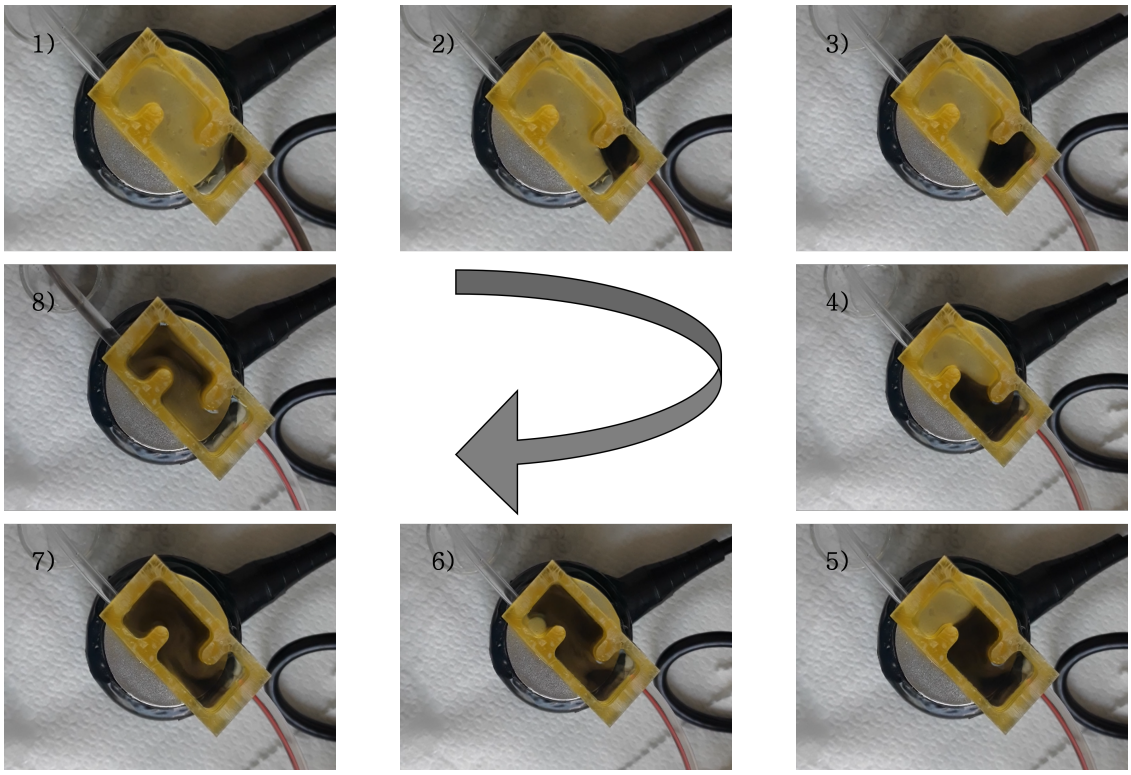

Figure 3.18: Sequence of images acquired during the flow of water and ink in a cartridge initially empty.

Finally, the last experiments are carried on to analyze the effects of US excitation on the solution contained inside the cartridge using Luminol sonochemiluminescence as previously done with the single wells. The solution employed is the same as before, consisting of Luminol 97% with a concentration 80 mM, sodium hydroxyde, NaOH, being 0.1 M, and hydrogen peroxyde, H_20_2, having a molarity of 0.5 mM. However, the prepared solution volumes are larger due to the greater capacity of the cartridge with respect to the wells. In addition, also the Digital camera used has the same settings as before: ISO 1200 and bulb f/4.

A first set of laboratory measurements is obtained with the "open cartridge", in a static solution condition by placing the cartridge above the transducer head adding a thin layer of coupling gel in between. The US powers tested are several, starting from the lowest ones, as 10%, 15% and 20% for 30 s and 2 min sonication times, up to higher powers, such as 50%, 60% and 80% with 30 s of US excitation. However, the following processing of the acquired images, consisting in the subtraction of the sonication image with the background image and the selection of a specific rectangular ROI matching the channel shape, gives

null blue intensity values for all the above mentioned conditions. These measurements are performed with the solution being in direct contact with air, characterized by an acoustic impedance of four order of magnitude lower compared to water, respectively equal to $0.000046 \cdot 10^6$ *Rayl* for air and $1.5 \cdot 10^6$ *Rayl* for water. This large gap is responsible for the reflection of the US wave, directed backward inside the solution. However, this behaviour could be not sufficient to produce an effective sonication of the solution and, consequently, a detectable amount of ROS.
For this reason, the only other possibility to enhance the Luminol sonochemiluminescence inside the solution and detect a possible ROS production is to cover the upper part of the cartridge with a lid, forming a "closed cartridge" system. In general, the glass material seems to provide higher blue intensity inside the contained solution since it is characterized by an acoustic impedance that greatly differs with the water one ($14.3 \cdot 10^6$ *Rayl*). This causes the acoustic wave to be reflected back with a phase delay of 180deg and may allow for a more intense sonication of the solution inside.
Therefore, in a second moment, the upper area of the cartridge is covered with a thin microscope glass slide by applying a sealing layer of Polydimethylsiloxane (PDMS), Figure 3.19. The PDMS is obtained by mixing together 1 g of elastomer and 0.1 g of curing agent to achieve a final 10:1 ratio. Then, it is spread over the upper boundaries of the cartridge and the glass is placed upon it by lightly pressing. As the system is positioned on a hot plate set at 70 $°C$, the PDMS starts to solidify, thus joining together the two components.

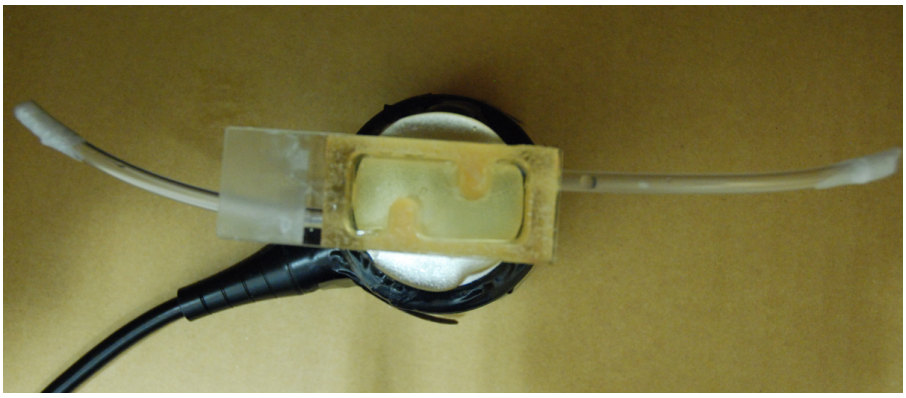

Figure 3.19: First printed cartridge closed with a thin glass slide.

Once having sealed the channel with the glass slide, a second set of experiments using Luminol solution is carried out. In this case, the effects of several parameters are investigated. First of all, different sonication power and time combinations are analysed, specifically the 15%, 20% and 80% for 30 s, 2 min and 1 min respectively, secondly, two

liquid volumes inside the channel are taken into account, in particular the condition when the channel is completely filled with water and the case when it is only half-filled in order to find the impact of the presence of air inside the closed serpentine path. Lastly, the cartridge is placed above the transducer surface area both in a normal position, with the glass lid on the upper area, and also in an upside-down position, with the glass slide in contact with the transducer.
Unfortunately, all the images post-processing give null blue intensity values in the area corresponding to the serpentine path shape. The reason behind these results may depend on a lower acoustic intensity generated inside the chamber, maybe due to its particular shape with respect to the outcomes obtained with the more confined feature of the single well.

3.3 Improved cartridge design and projects

As the first printed cartridge showed an excellent mechanical structure, able to withstand to various different sonication powers and times, such as also to 100% for a time period of 30 s, providing at the same time a certain transparency of the inner channel, the PEGDA material has proven to be a good choice for the development of a biocompatible, sonication chamber. The only factor that remains unknown is the effective production of ROS inside the channel, since the Luminol sonochemilumiscence gives no significant results. This problem will be addressed in conjuction with the COMSOL simulations of the acoustic wave propagation concerning the new cartridge prototypes.
In fact, considering that the major problem of the first printed cartridge prototype is the fluid flow inside the channel, characterized by a certain degree of turbulence, especially close to the inlet area, as well as the presence of stagnant regions close to the corners, new cartridge prototypes with different inlet and outlet configurations are proposed.

3.3.1 Lateral inlet and outlet

CAD project

The first cartridge design re-proposes the original version of the project, consisting on three channels, as shown in Figure 3.20, whose length develops along the longer side of the cartridge (L) to better guide the fluid flow along the serpentine path, thus minimizing the possible turbulence and stagnant areas, and having in-plane lateral inlet and outlet. However, differently from the original project, its dimensions are chosen to fit within the size limitations required by the printing process and therefore, are the same used for the first printed cartridge. Finally, another similarity with the printed cartridge relies on the on the choice to build the inlet and outlet apertures in the area within the cartridge structure, and not external to it, in order to provide the required mechanical robustness both during the printing process and also for the positioning of the tubes preventing structural damages and cracks.

More specifically, in order to fit three channels along the width of the entire cartridge, the thickness of the lateral and internal walls is properly reduced to give space to the presence of the channel. Therefore, even if it has a lower width than the previous considered design, selected to be equal to the size of the Therakos® tubes, $W_{ch} = 4.5\ mm$, its length properly counterbalances the loss of volume due to the thinner serpentine shape of the channel. The overall parameters are resumed in Table 3.3.

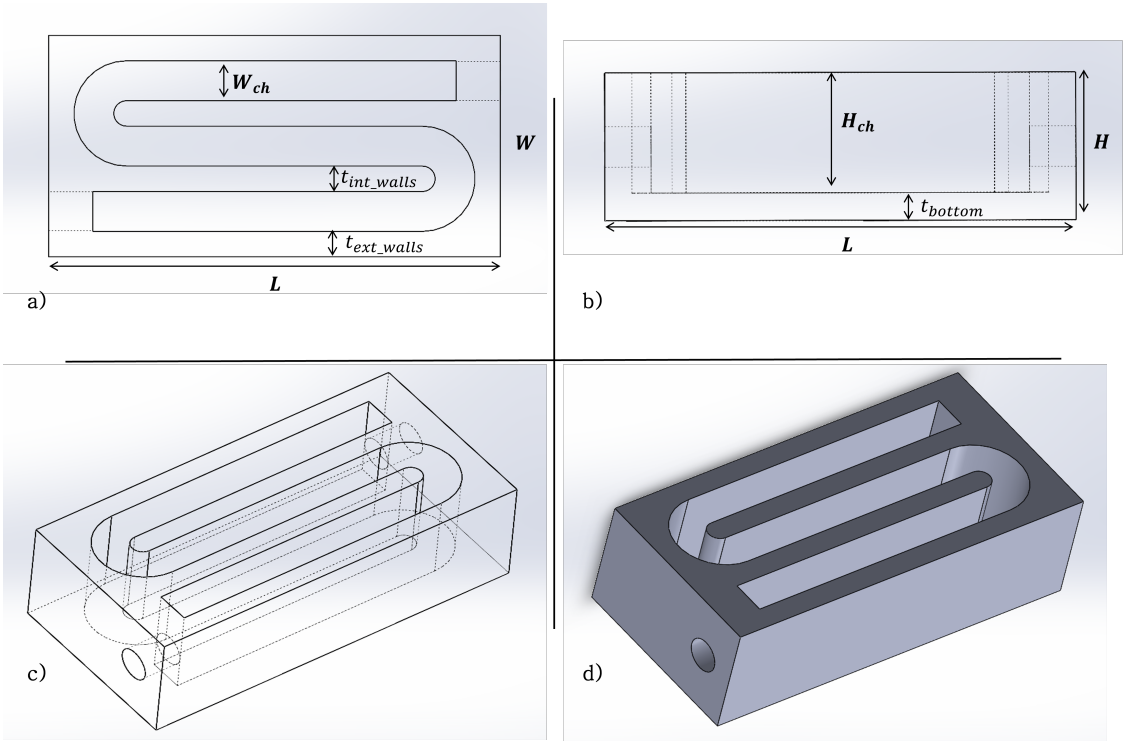

Figure 3.20: CAD project of the first proposed new cartridge: a) top view, b) side view, c) lateral view and d) lateral view of the expected 3D printing process outcome.

Parameters	Values	Description
W	25 mm	Width of the cartridge
L	51 mm	Length of the cartridge
H	16 mm	Height of the cartridge
W_{ch}	4.5 mm	Width of the channel
L_{ch}	126.46 mm	Length of the channel
H_{ch}	13 mm	Height of the channel
t_{bottom}	3 mm	Thickness of the of the basis
t_{walls}	2.88 mm	Thickness of all the walls
Total Volume	7.4 mL	Maximum volume

Table 3.3: Parameters of the first proposed new cartridge project.

COMSOL simulations

At first, as in the previous case, the Reynolds number is calculated to assess the fluid flow regime in order to be simulated using COMSOL. The flow rate is assumed to be the

maximum value achievable by the peristaltic pump, $Q = 17.47\ mL/min$, leading to an average velocity through the channel of $u_{ave} = 4.98\ mm/s$. Since the hydraulic diameter is found to be $D_h = 6.69\ mm$, by substituting these values inside the Reynolds number expression, the latter turns out to be equal to:

$$Re = \frac{\rho\, U D_h}{\eta} = 37.35 \tag{3.19}$$

typical of a laminar flow state.

Then, the CAD project of the entire internal channel of the cartridge, including the inlet and outlet apertures is designed since it corresponds to the COMSOL simulation domain. Its subsequent discretization on fine elements is provided by selecting the physics controlled mesh, as shown in Figure 3.21.

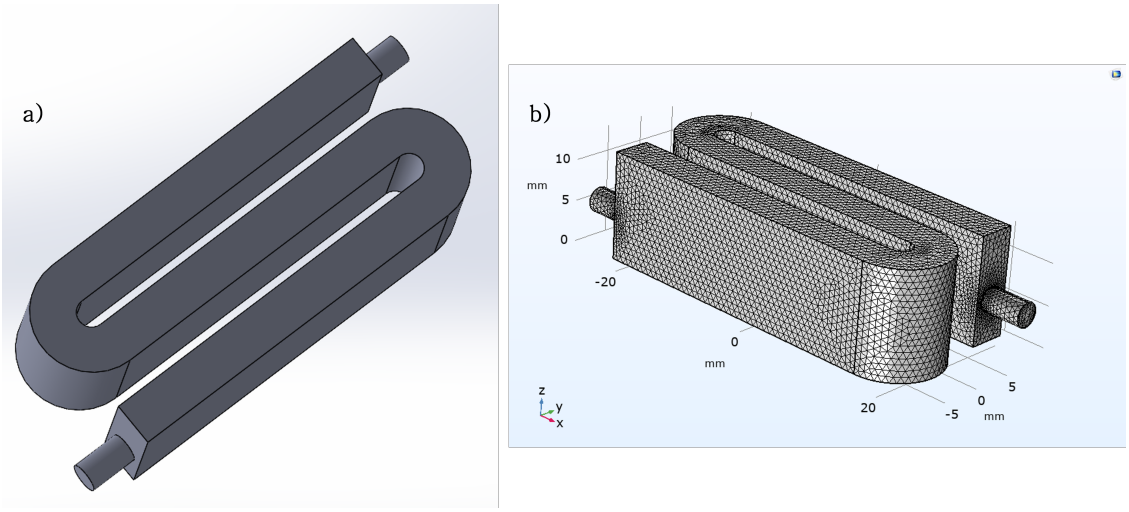

Figure 3.21: a) CAD project for COMSOL simulation representing the implemented domain and b) meshing of the channel CAD design.

However, differently from the previous flow simulations, the flow rate set at the inlet of the channel is modified from its maximum value, $Q = 17.47\ mL/min$, to $Q = 12\ mL/min$ and $Q = 7\ mL/min$. In fact, from both the fluid flow simulations and the experimental results of the first printed cartridge, the maximum flow rate seems to generate a too high velocity inside the channel that may prevent the effective sonication of the solution: the rapid flow of the fluid over the transducer head results in a too short exposure time of the solution volume to the US waves. Hence, in order to increase the time required by the fluid to complete the entire serpentine path, two different lower values of the flow rate are investigated:

1. **Q=12 mL/min**, also written as $Q = 2 \cdot 10^{-7}\ m^3/s$, generates a velocity magnitude distribution whose maximum values occurs in correspondence to the inlet and outlet apertures (Fig. 3.22); however, while at the inlet the velocity starts with the highest value and then gradually decreases when entering deeper inside the channel, at the outlet an higher velocity value exists only at the outlet hole. In the remaining part of the channel, the velocity remains approximately constant with lower values, as highlighted by the blue color of its magnitude distribution, ranging from 0 to 15 mm/s.

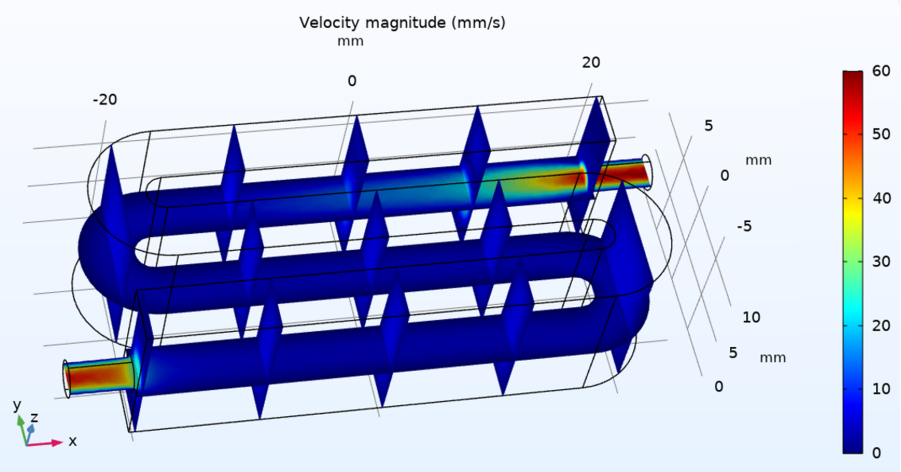

Figure 3.22: Horizontal and vertical planes of the velocity magnitude distribution along the channel: the horizontal plane corresponds to an height equal to $z = 5\ mm$, in-plane with the inlet and outlet apertures for $Q = 12\ mL/min$.

As previously done, since it is of interest to know also the behavior of the velocity vector and not only its magnitude, emphasizing possible turbulent and stagnant areas, the velocity along the channel is described through streamlines plot, presented in Figure 3.23. With this configuration, the fluid is no more blocked as soon as it enters within the channel by the internal wall of the serpentine as in the previous printed cartridge, allowing to propagate directly along the whole length of the chamber. However, a certain turbulence is still present, especially in the region close to the inlet due to the high speed with which the fluid enters in the channel, while in the remaining areas, the flow remains smooth until it reaches the outlet.

Finally, since the optimal fluid flow condition inside the channel required to provide a constant, slow and homogeneous US excitation of the cells is characterized by the most possible uniform velocity distribution throughout its entire length, the velocity profiles along specific vertical cut lines are plot and analysed, as reported in Figure

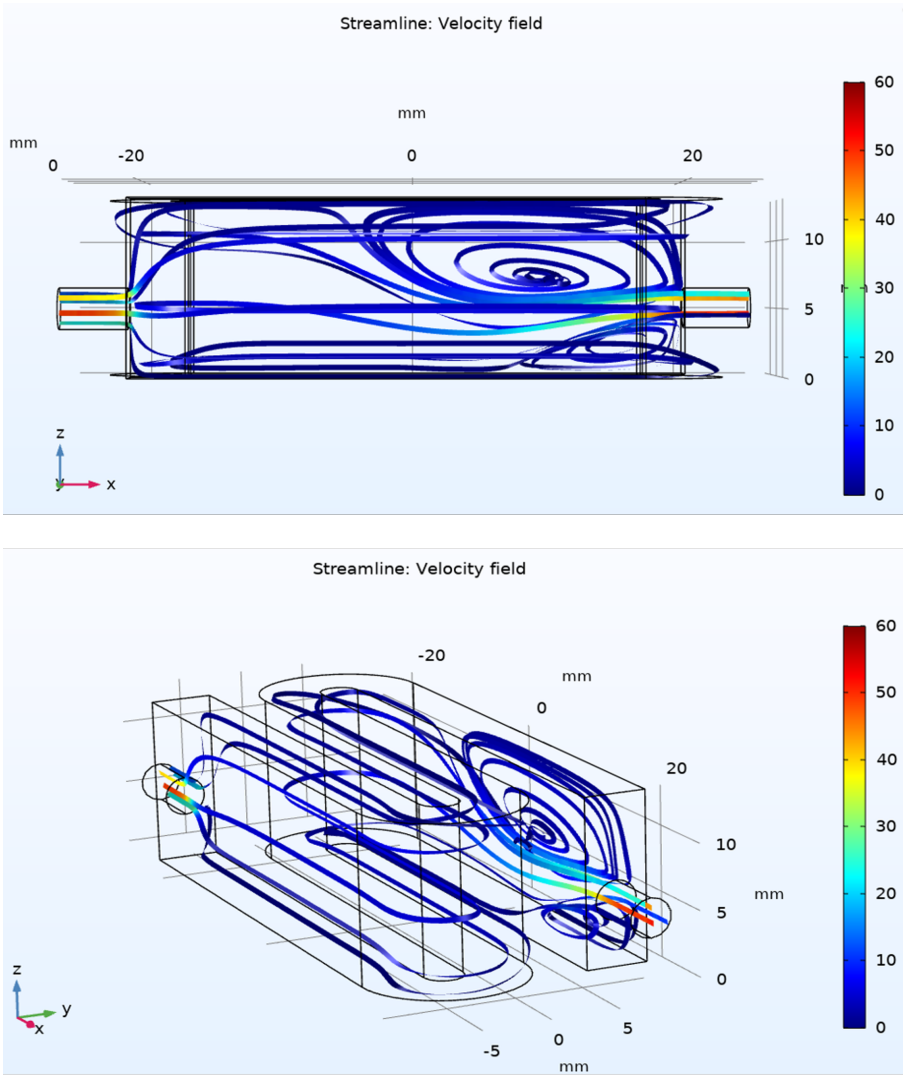

Figure 3.23: Velocity streamlines plot for $Q = 12\ mL/min$.

3.24.

The colors of each velocity curve corresponds to the specific vertical line selected: it is evident that the velocity profile close to the inlet shows the highest maximum value approximately at an height which is in-plane with the inlet aperture, while a second lower velocity peak is associated to the turbulent behavior as shown by the streamlines plot. As the fluid continues to flow throughout the channel, the velocity begins to decrease, achieving the expected laminar profile having a parabolic shape with null

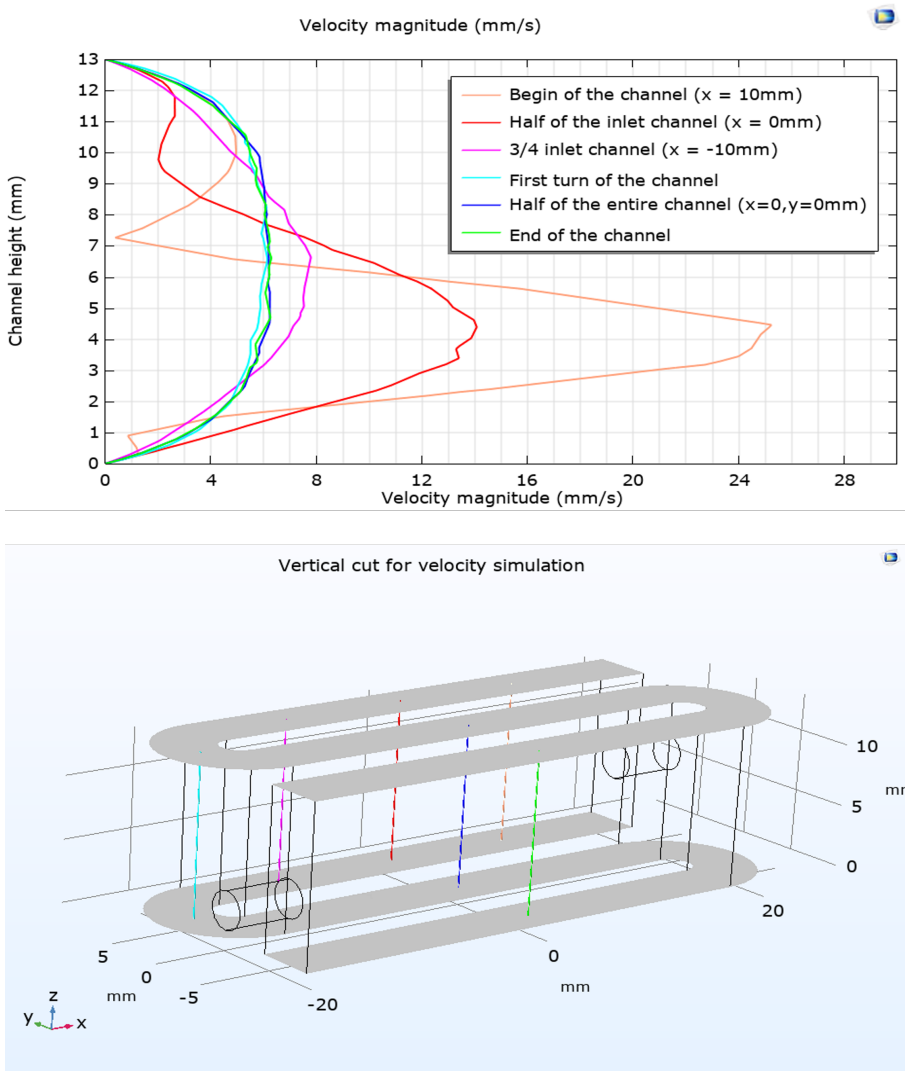

Figure 3.24: Velocity profile (top) and chosen lines cutting vertically the channel (bottom) for $Q = 12\ mL/min$.

velocity at the boundaries (at the top and bottom surface areas) that remains constant until the end of the channel is reached. Since this latter profile corresponds to be the most effective velocity behaviour that remains uniform for most of the channel length, the main purpose of the simulations is to find the most suitable condition to obtain a constant profile already close to the inlet region, minimizing the development or entrance length required for the fluid to reach a steady-state regime.

For this reason, the flow rate along the channel is further decreased to reduce the

entrance length.

2. **Q=7 mL/min**, also equal to $Q = 1.17 \cdot 10^{-7}$, shows an overall decrease of the velocity magnitude (Fig. 3.25), however maintaining a similar behaviour with respect to the distribution obtained with $Q = 12\ mL/min$. In fact, the higher velocity values exist close to the inlet and outlet apertures, while the remaining length of the channel is characterized by a lower speed, as in the previous case.

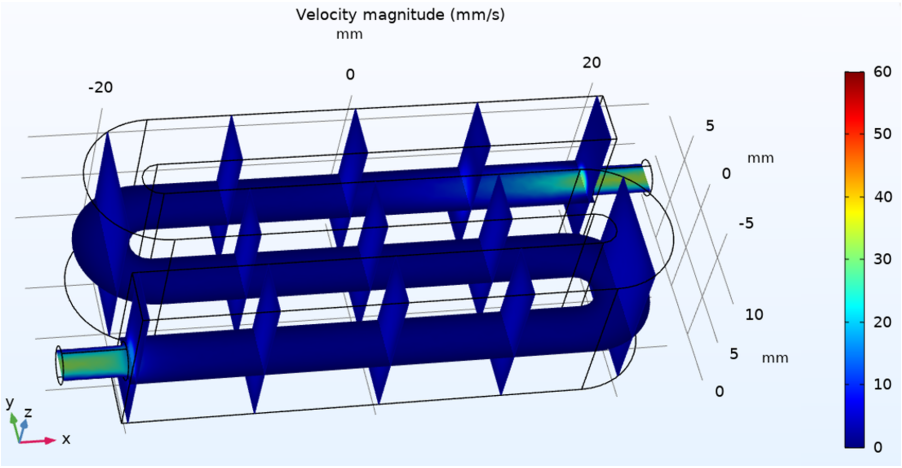

Figure 3.25: Horizontal and vertical planes of the velocity magnitude distribution along the channel: the horizontal plane corresponds to an height equal to $z = 5\ mm$, in-plane with the inlet and outlet apertures for $Q = 7\ mL/min$.

The velocity streamlines plot highlights a very similar behaviour with $Q = 12\ mL/min$, consisting in a quite turbulent region right close to the inlet aperture since it remains the area with the highest velocity, that gradually decreases while the fluid enters deeply within the channel (Fig. 3.26). However, it may be observed that the streamlines emphasizing the turbulence at the inlet are confined in a smaller region than before, thus providing an effective reduction in the development length of the fluid flow.

This phenomenon is also highlighted by the velocity profile (Fig. 3.27), whose vertical lines are selected in the same positions as in the previous case: the velocity curve at the inlet not only has a lower maximum peak, always corresponding to the same height of the inlet aperture (around $z = 5\ mm$), it also has a smaller peak associated to the turbulent area. As the fluid continues its path along the channel, the velocity reaches a steady-state condition already at 3/4 of the inlet channel, while with $Q = 12\ mL/min$

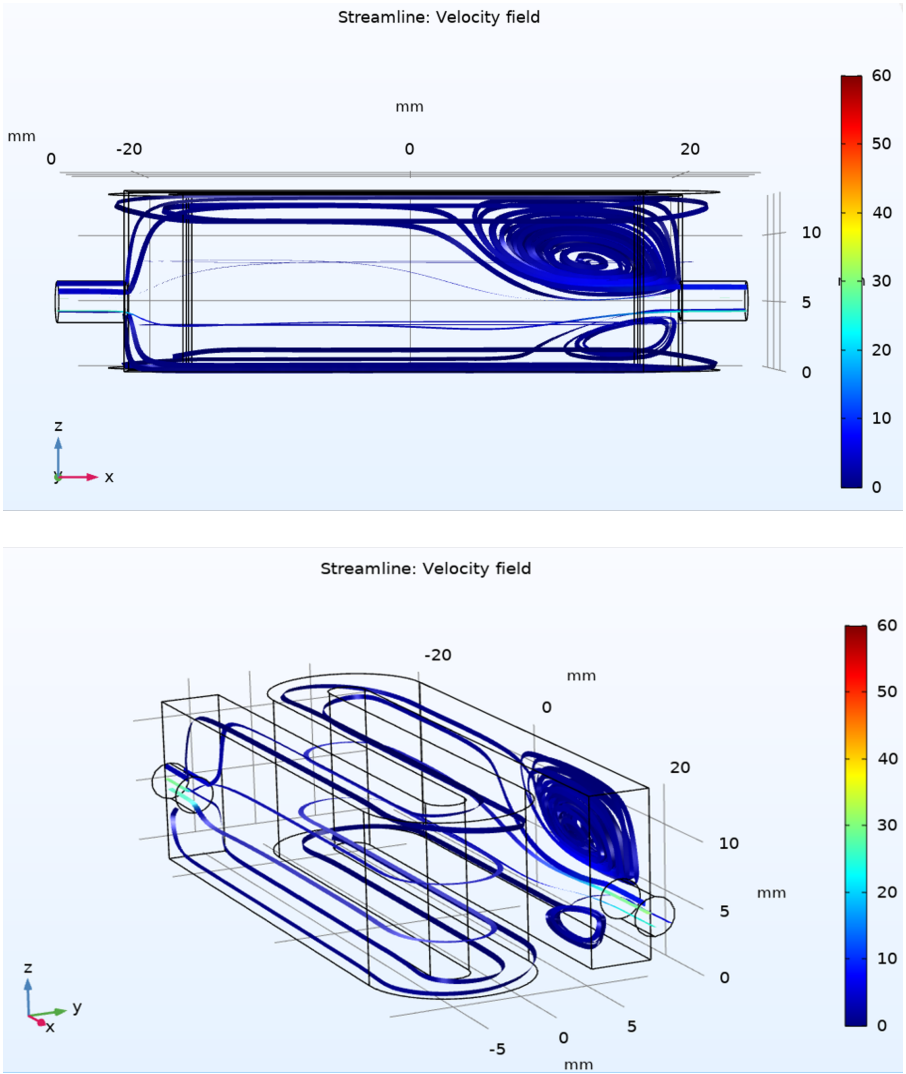

Figure 3.26: Velocity streamlines plot for $Q = 7\ mL/min$.

it occurs in correspondence of the first turn.

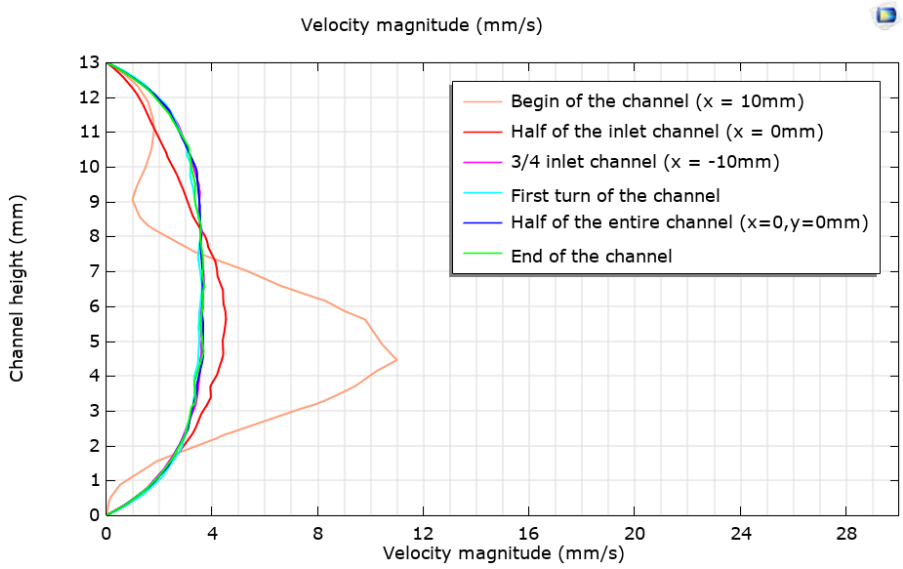

Figure 3.27: Velocity profile for $Q = 7\ mL/min$.

At the end of the description of this new proposed cartridge design, a further comment should be made on the time it takes for the fluid to complete the entire channel serpentine path. For this reason, the mean velocity is extrapolated for each simulation condition, thus providing an estimation of the time period required, reported in Table 3.4.

Q (mL/min)	**Q (m^3/s)**	**Velocity$_{ave}$ (mm/s)**	**Travel time (s)**
$Q_{max} = 17.47$	$Q = 2.9{\cdot}10^{-7}$	$u_{max} = 5.95$	$t_{min} = 22.01$
$Q = 12$	$Q = 2{\cdot}10^{-7}$	$u = 3.93$	$t = 33.33 \simeq 30$
$Q = 7$	$Q = 1.17{\cdot}10^{-7}$	$u = 2.20$	$t = 59.63 \simeq 60$ (1min)
$Q = 5$	$Q = 8.33{\cdot}10^{-8}$	$u = 1.54$	$t = 85.06 \simeq$ 1min, 25s

Table 3.4: Fluid flow simulations values regarding average velocity and time required to complete the serpentine path for different flow rates Q.

The presented average velocity values are slightly higher than the ones calculated manually to obtain the Reynolds number: probably this is due to the increased velocity at the inlet and outlet that tends to enhance its overall mean value, while in the calculations the inlet and outlet regions are not considered since it serves only for the statement of the fluid flow regime and the choice of the simulation parameters.
Furthermore, since the sonication time required to obtain an effective treatment seems to be, from the experimental results, at least of 30 s, the most significant flow rates may be

lower then $Q = 12\ mL/min$.

3.3.2 Bottom inlet and outlet

CAD project

The second new cartridge design proposed as alternative to the first one offers the possibility to have the inlet and outlet apertures from the bottom surface area of the cartridge (Figure 3.28): an expedient to further minimize the inlet higher velocity and obtain a uniform profile along the channel.

As a consequence the two inlet and outlet holes are designed on the lower basis in correspondence to the beginning and ending of the channel in order to avoid stagnant areas for the cells. In this case, the depth of the apertures providing the insertion of the external tubes is reduced from 5 mm to 3 mm, corresponding to the lower basis thickness; this value is maintained to 3 mm since it would be detrimental for the propagation of US to increase the basis thickness to 5 mm trying to provide a better interlocking of the tubes. Thus, the effective propagation of US is a more significant parameter than the tubes joint. An other modification considered is that to further enhance the width of the channel, the thickness of both the lateral and inner walls is reduced, giving an overall larger volume to the serpentine path. Finally, to meet also the requirements coming from the printing process, the height of the channel is reduced from 13 mm to 11 mm and also a thin upper cover is printed in order to prevent the structure to sag and collapse. All the variables describing the CAD project are resumed in Table 3.5.

Parameters	Values	Description
W	25 mm	Width of the cartridge
L	51 mm	Length of the cartridge
H	14 mm	Height of the cartridge
W_{ch}	5.47 mm	Width of the channel
L_{ch}	133.51 mm	Length of the channel
H_{ch}	11 mm	Height of the channel
t_{bottom}	3 mm	Thickness of the of the basis
t_{ext_walls}	2 mm	Thickness of the external walls
t_{int_walls}	2.3 mm	Thickness of the internal walls
Total Volume	8.03 mL	Maximum volume

Table 3.5: Parameters of the second proposed new cartridge project.

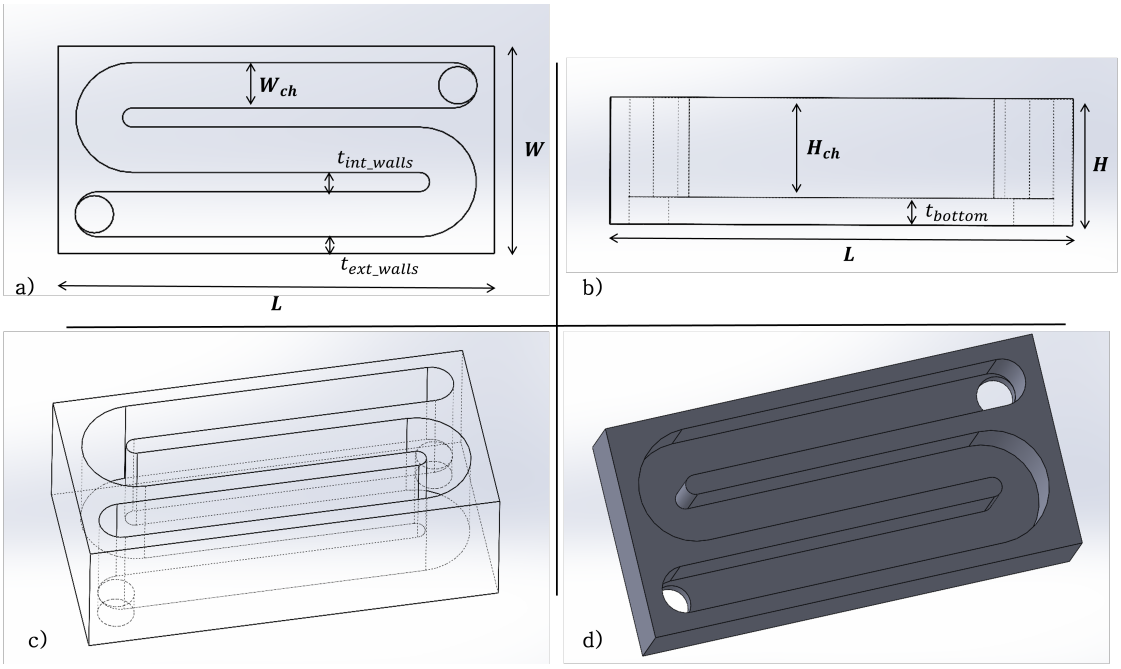

Figure 3.28: CAD project of the second proposed new cartridge: a) top view, b) side view, c) lateral view and d) lateral view of the expected 3D printing process outcome.

COMSOL simulations

The same procedure previously carried out is repeated by first calculating the Reynolds number associated to the maximum available flow rate. The average velocity calculated turns out to be $u_{ave} = 4.84\ mm/s$, while the hydraulic diameter has a value of $D_h = 7.307\ mm$, leading to a value of the Reynolds number equal to $Re = 39.65$, characteristic of a laminar flow regime.
Secondly, the CAD project of the COMSOL domain is designed, implementing also the same mesh used for the systems described before, presented in Figure 3.29.

In order to compare the different configurations and choose the most effective one, the fluid flow behavior is investigated for the two different flow rates previously analysed: $Q = 12\ mL/min$ and $Q = 7\ mL/min$.

1. For the first flow rate, **Q=12 mL/min**, the velocity magnitude distribution obtained (Fig. 3.30) is characterized by higher values in correspondence with the inlet and outlet apertures, as in the previous cartridge; however, in this case, since the fluid moves in a vertical direction with respect to the channel horizontal plane, the velocity starts

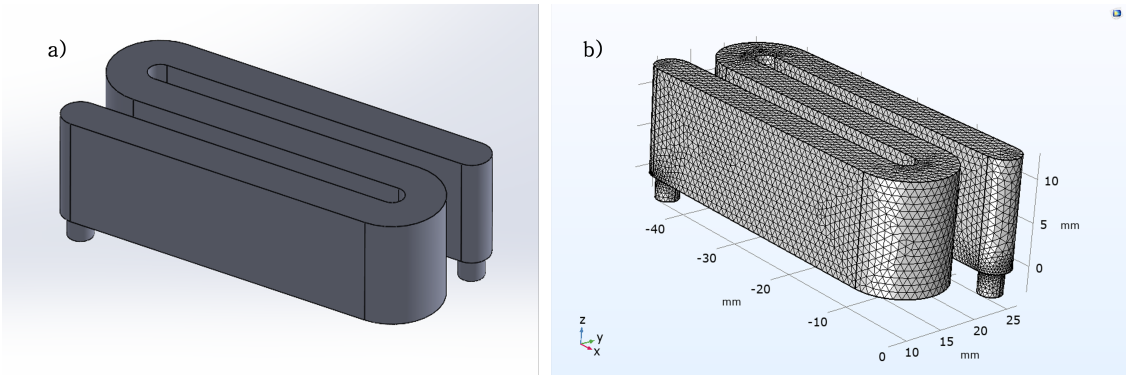

Figure 3.29: a) CAD project for COMSOL simulation representing the implemented domain and b) meshing of the channel CAD design.

from its highest possible value at the beginning of the inlet hole and then gradually decreases moving upwards, towards the upper area of the channel. After this initial region, strictly confined close to the inlet, the velocity magnitude decreases, emphasized by the blue color over the majority of the channel length. As the fluid arrives at the outlet, an increase in the velocity occurs right in the volume above the outlet hole, without affecting importantly the surrounding area.

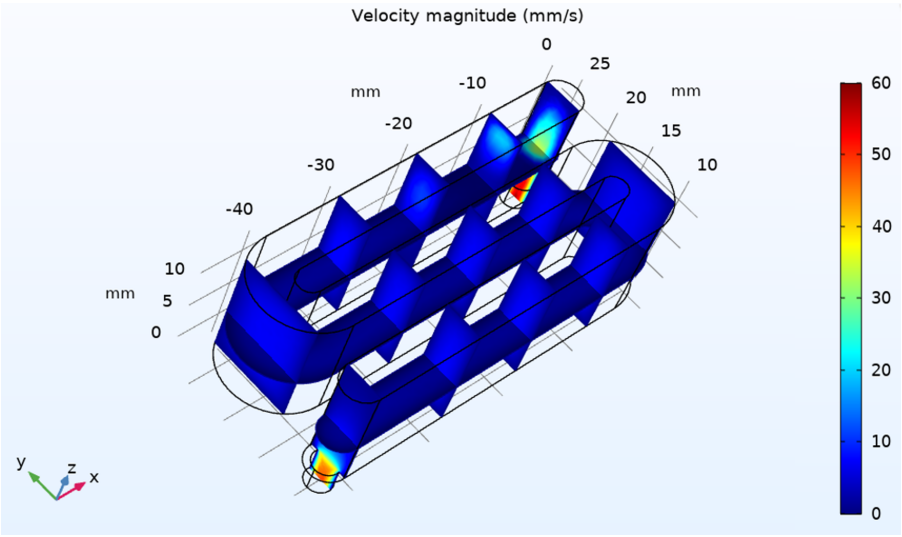

Figure 3.30: Horizontal and vertical planes of the velocity magnitude distribution along the channel: the horizontal plane corresponds to an height equal to $z = 5\ mm$ for $Q = 12\ mL/min$.

Following the same analysis steps, the possible turbulence inside the channel is highlighted by plotting the velocity vector streamlines, shown in Figure 3.31. With this inlet configuration, the solution flowing upwards in a vertical direction tends to curve back on itself and return towards the basis, generating a slight turbulent flow close to the inlet right above the inlet entrance. Then, the fluid flows smoothly through the entire length and when it reaches the outlet, it simply tends to "fall" outside the channel, characterized by a light bending of the velocity vector.

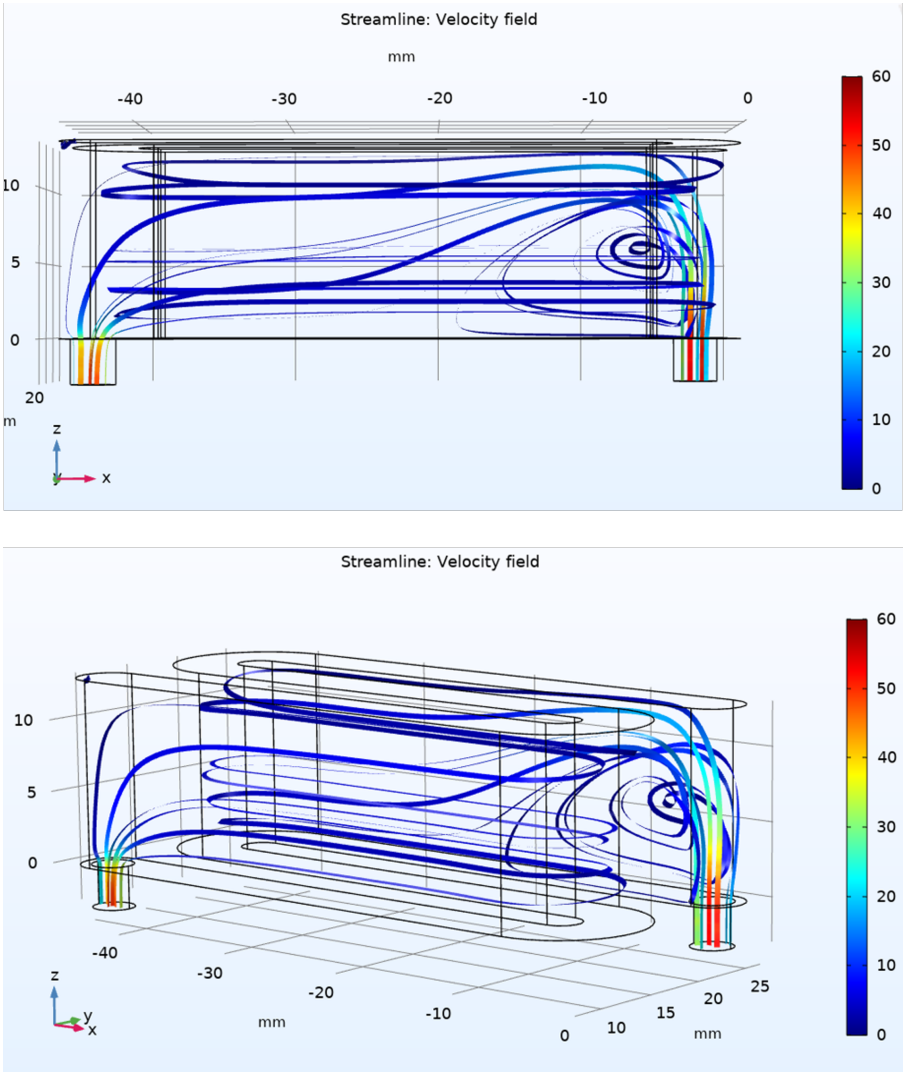

Figure 3.31: Velocity streamlines plot for $Q = 12\ mL/min$.

Finally, the velocity profile plot is presented in order to analyse the trend of the parabolic curve all along the channel (Fig. 3.32).

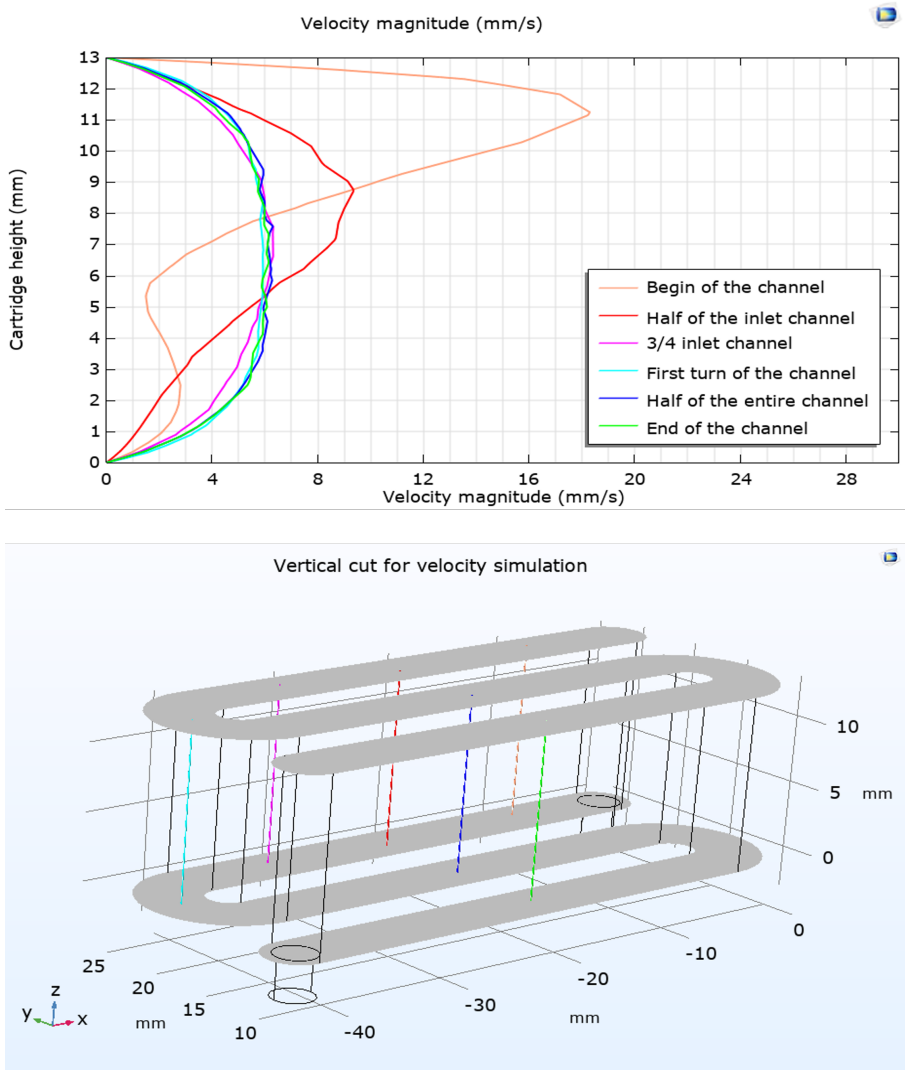

Figure 3.32: Velocity profile (top) and chosen lines cutting vertically the channel (bottom) for $Q = 12\ mL/min$.

Differently from the previous proposed cartridge design, the maximum peak associated to the first cut line of Figure 3.32, the one closer to the inlet, occurs to be in the higher part of the channel, while the second minor peak corresponds to the more turbulent region towards the bottom of the channel itself. Furthermore, this configuration seems to provide a better behaviour of the velocity than the previous one since its profile reaches a constant and uniform trend already at 3/4 of the inlet channel with a flow rate of $Q = 12\ mL/min$ while, with lateral inlet and outlet the steady-state

is achieved at the first turn of the channel, considering the same value of flow rate. This means that the bottom inlet and outlet configuration provides a shorter development length and a more uniform velocity profile along the entire length of the channel.

2. The second value of flow rate, **Q=7 mL/min**, responsible for a longer time required by the fluid to travel the entire path of the channel is also taken into account. As found previously, the velocity magnitude distribution (Fig. 3.33) has the same behaviour as in the case with higher flow rate, but is characterized by overall lower velocity values: this is represented by the green color at the inlet and outlet apertures, associated to a slower speed over that regions. Furthermore, the dimensions of the turbulent area are reduced, as emphasized by the velocity streamlines plot, Fig. 3.34, leading to a further shorter development length at the beginning of the channel.

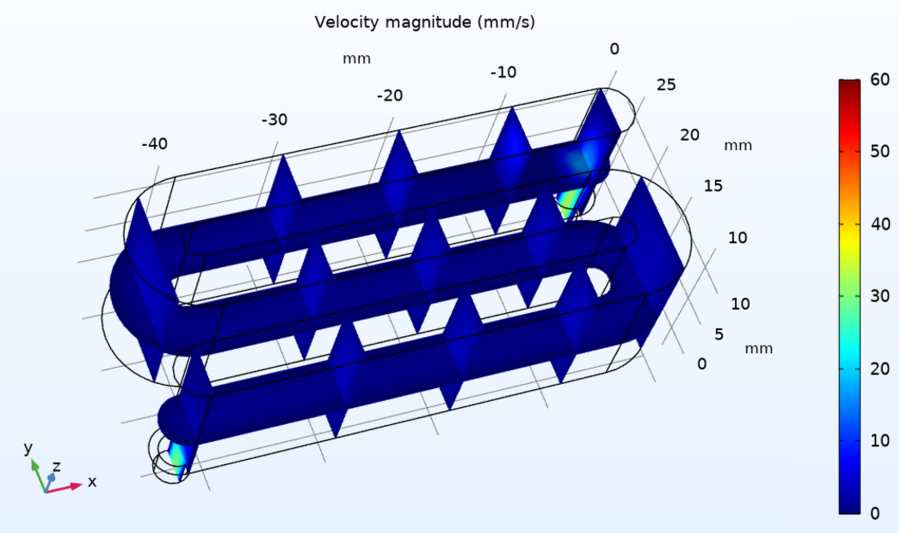

Figure 3.33: Horizontal and vertical planes of the velocity magnitude distribution along the channel: the horizontal plane corresponds to an height equal to $z = 5\ mm$ for $Q = 7\ mL/min$.

Finally, the velocity profile plot, Fig. 3.35 greatly emphasizes the effect of a shorter entrance length with $Q = 7\ mL/min$: the fluid flow is able to reach the steady-state condition already at half of the inlet channel, providing a longer path along the serpentine in which the velocity remains uniform and constant that represents the most desirable behavior.

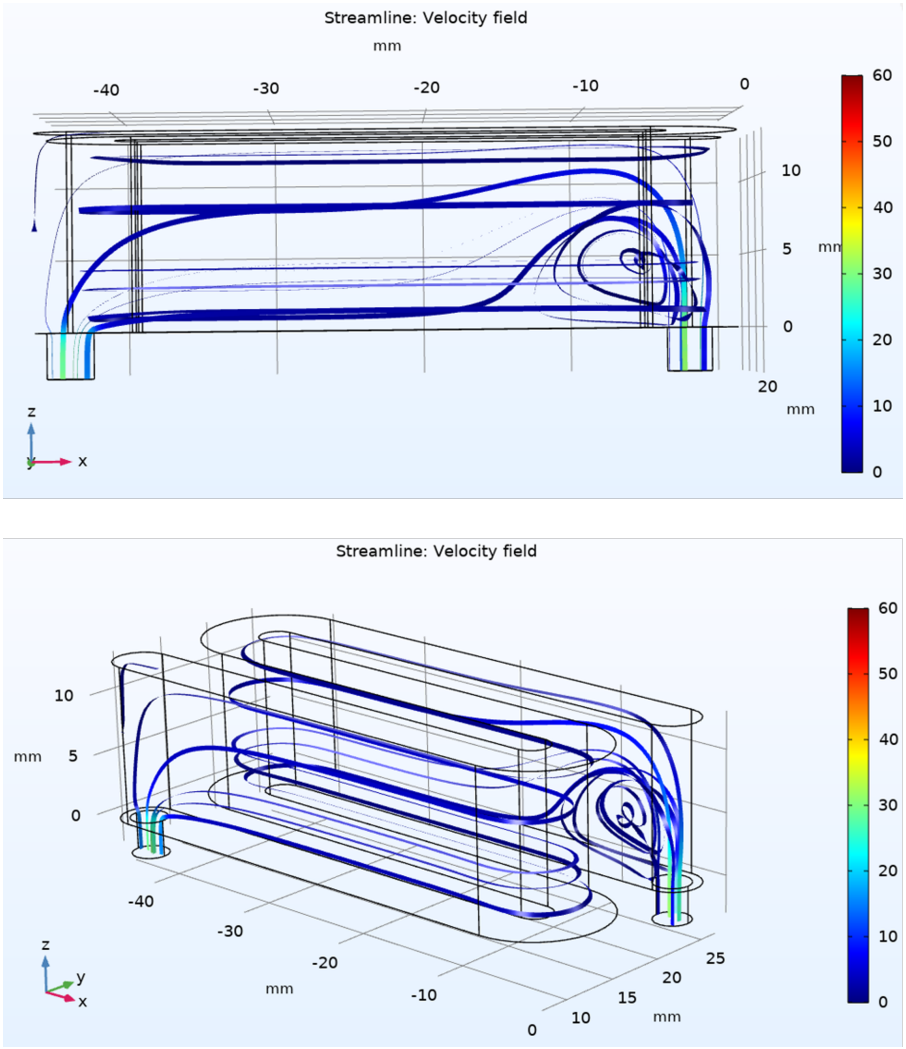

Figure 3.34: Horizontal and vertical planes of the velocity magnitude distribution along the channel: the horizontal plane corresponds to an height equal to $z = 5\ mm$ for $Q = 7\ mL/min$.

As a consequence, as presented in Table 3.6, comparing the mean velocity and time values with the previous new proposed cartridge design, this specific configuration having the inlet and outlet apertures at the bottom of the cartridge allows to obtain a constant velocity profile for a longer path inside the channel for a given flow rate. For this reason, from the simulations, it seems that the fluid flow tend to have a correct behaviour, fulfilling the requirements dictated by both its future operation in the presence of cells and the constraints related to the printing process.

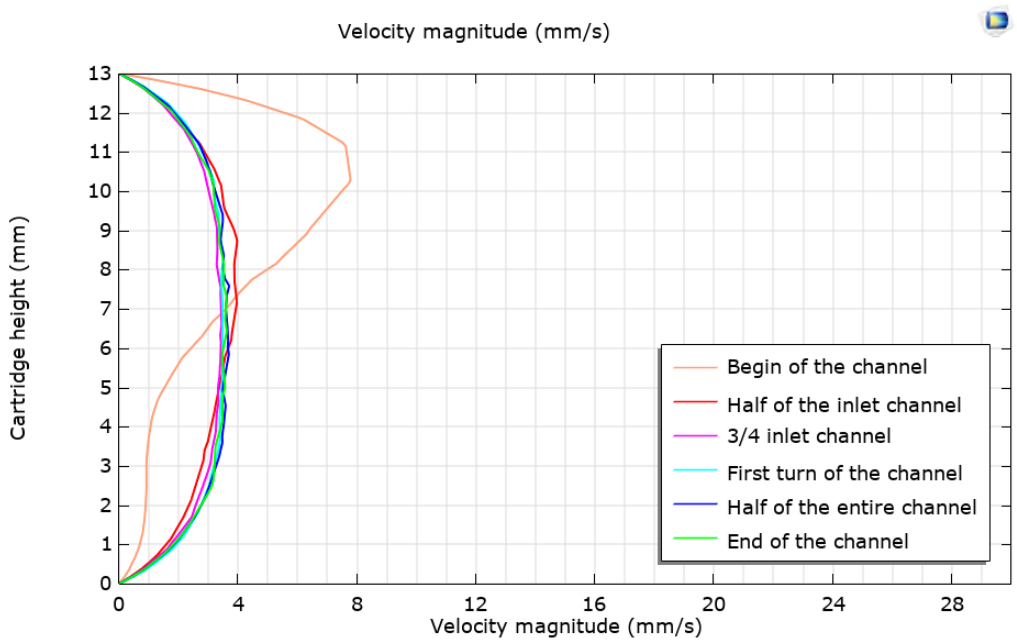

Figure 3.35: Velocity profile for $Q = 7\ mL/min$.

Q (mL/min)	**Q (m^3/s)**	**Velocity$_{ave}$ (mm/s)**	**Travel time (s)**
$Q_{max} = 17.47$	$Q = 2.9{\cdot}10^{-7}$	$u_{max} = 5.76$	$t_{min} = 22.74$
$Q = 12$	$Q = 2{\cdot}10^{-7}$	$u = 3.87$	$t = 33.85 \simeq 30$
$Q = 7$	$Q = 1.17{\cdot}10^{-7}$	$u = 2.19$	$t = 59.82 \simeq 60$ (1min)
$Q = 5$	$Q = 8.33{\cdot}10^{-8}$	$u = 1.53$	$t = 85.47 \simeq$ 1min, 25s

Table 3.6: Fluid flow simulations values regarding average velocity and time required to complete the serpentine path for different flow rates Q.

Therefore, the remaining property to be investigated is its ability to provide an effective sonication of the solution. For this purpose, COMSOL simulations regarding the acoustic wave propagation inside the channel of the cartridge, assuming to be completely filled with water, are carried on by considering different conditions regarding US intensity, basis thickness and medium above the channel serpentine, in particular air and glass.

At first, the US intensity and basis thickness are maintained fixed to analyse the effects arising from the choice of a different medium above the cartridge: for an US power equal to 20% and a basis 1.3 mm thick, the acoustic wave behaviour is examined both in the case of an "open cartridge", without any cover on the top part and thus, the channel is exposed to air, and in the case of a "closed cartridge" with a thin layer of glass upon it (Figure 3.36).

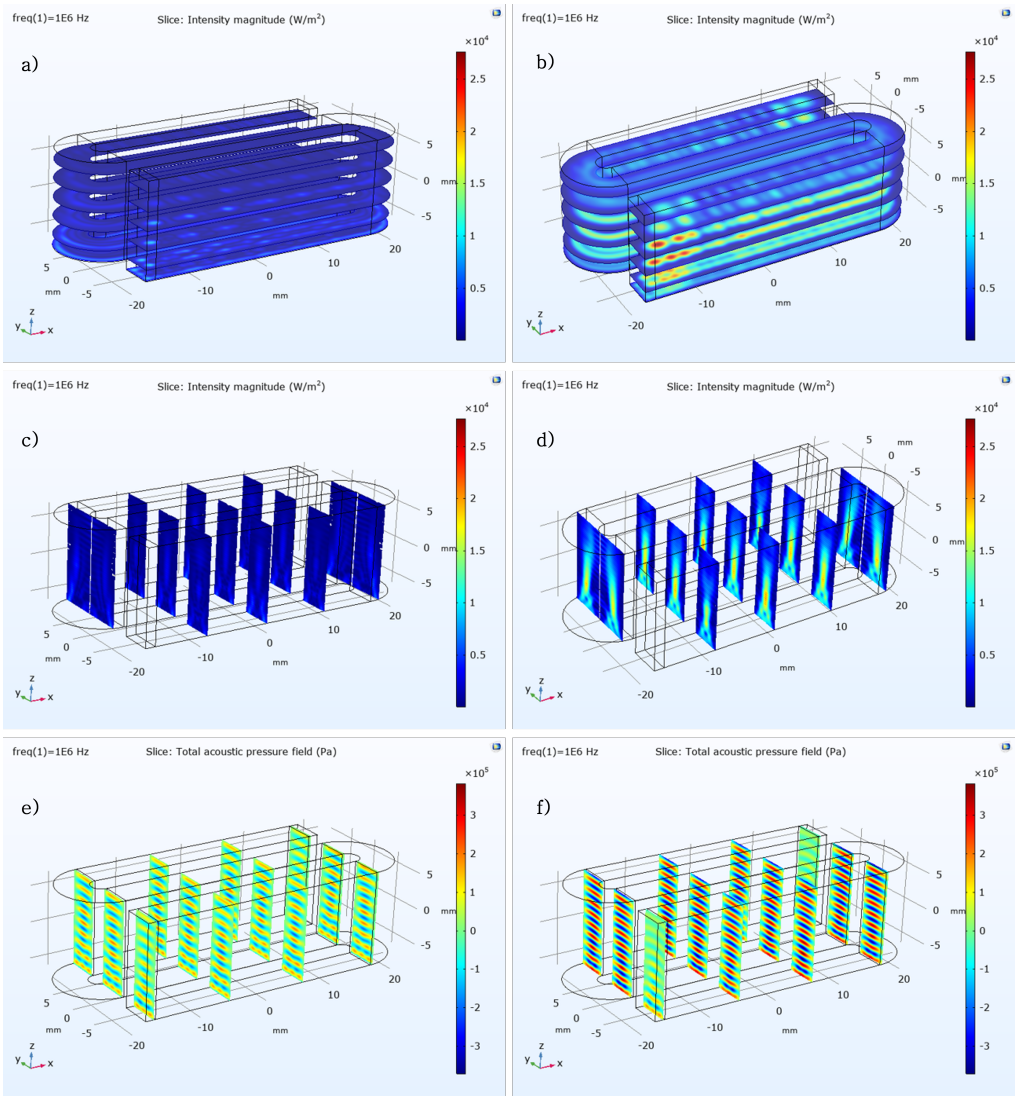

Figure 3.36: Comparison of the acoustic wave distribution inside the channel in the case of an "open cartridge" exposed to air (left column) and of a "closed cartridge" with a glass lid on the top (right column): a) and b) intensity horizontal planes along the channel, c) and d) intensity vertical planes and, finally, e) and f) pressure acoustic vertical planes.

In general, by comparing the US intensity distributions obtained, they are characterized by a similar trend in both the conditions, however showing an enhanced magnitude when the channel is covered by a layer of glass, moving from a value of $I_{max\_air} = 8.87 \cdot 10^3\ W/m^2$ associated with the open air condition to $I_{max\_glass} = 2.76 \cdot 10^4\ W/m^2$ related to the presence of a glass lid. Similar comments may be made for the acoustic pressure behaviour,

which increases from $p_{max\_air} = 2.20 \cdot 10^5 Pa$ when the water solution inside the channel is in contact with air, to $p_{max\_glass} = 3.82 \cdot 10^5 Pa$ in the case of the glass cover. In conclusion, the presence of glass on the top part of the channel provides a more intense sonication of the solution within the channel: this behaviour may be generated by the large difference between the acoustic impedances of water and glass, $Z_{water} = 1.5 \cdot 10^6\ Pa \cdot s/m$ and $Z_{glass} = 14.3 \cdot 10^6\ Pa \cdot s/m$ respectively, which causes the acoustic wave to be reflected back at the water/glass interface, allowing the solution to undergo the effects of the forward propagating wave as well as the backward one.

Material	**Thickness**	**Top**	**Power**	**Max intensity**	**Max pressure**
PEGDA	t = 1.3 mm	Air	15%	$\simeq 6.67{\cdot}10^3$	$\simeq 1.85{\cdot}10^5$
PEGDA	t = 1.3 mm	Air	20%	$\simeq 8.87{\cdot}10^3$	$\simeq 2.20{\cdot}10^5$
PEGDA	t = 1.3 mm	Glass	15%	$\simeq 2.08{\cdot}10^4$	$\simeq 3.31{\cdot}10^5$
PEGDA	t = 1.3 mm	Glass	20%	$\simeq 2.76{\cdot}10^4$	$\simeq 3.82{\cdot}10^5$
PEGDA	t = 1.3 mm	Glass	80%	$\simeq 1.1{\cdot}10^5$	$\simeq 7.65{\cdot}10^5$
PEGDA	t = 3 mm	Air	15%	$\simeq 6.53{\cdot}10^3$	$\simeq 1.89{\cdot}10^5$
PEGDA	t = 3 mm	Glass	15%	$\simeq 2.03{\cdot}10^4$	$\simeq 3.28{\cdot}10^5$
PS-Well	t = 1.3 mm	Air	15%	$\simeq 9{\cdot}10^4$	$\simeq 7.41{\cdot}10^5$

Table 3.7: Acoustic wave intensity and pressure values for different simulation parameters, as US power, top medium above the channel and basis thickness.

The second parameter whose effects are analysed when its value is changed is the bottom thickness of the basis. In fact, all the cartridge projects designed so far are characterized by a 3 mm thick basis and the consequences of a thinner basis are investigated. From the Table 3.7, it can be noticed that, even if both the acoustic intensity and pressure slightly decrease, the bottom thickness does not affect significantly their magnitude since the difference between the $t = 1.3\ mm$ and $t = 3\ mm$ is not so important. As an example, taking into account the simulation results by setting an US excitation power equal to 15%, independently from the medium (air or glass) above the solution, the difference in the acoustic intensity and pressure values between the two thicknesses is minimal. This means that the acoustic wave does not undergo an important attenuation while propagating through the PEGDA basis. For this reason, since the 3 mm basis thickness provides a certain robustness and mechanical resistance to the cartridge structure and, at the same time, its impact in the acoustic wave propagation is negligible, the basis thickness is left to its original value of 3 mm, without reducing it.

The last quantity to be modified is the US power, considering the 15%, 20% and even 80%, trying to make a parallelism also with the previous simulations results obtained with the single well of a 24 well-plate. First of all, from Table 3.7 it is possible to notice that, by increasing the US power, both the acoustic intensity and the pressure reach the highest values inside the channel while maintaining a similar overall behaviour, as shown in Figure 3.37, in which the acoustic wave distribution generating from an 80% US power is presented: the distribution is rather the same as in the case of 20% power but the intensity and pressure values are obviously higher.

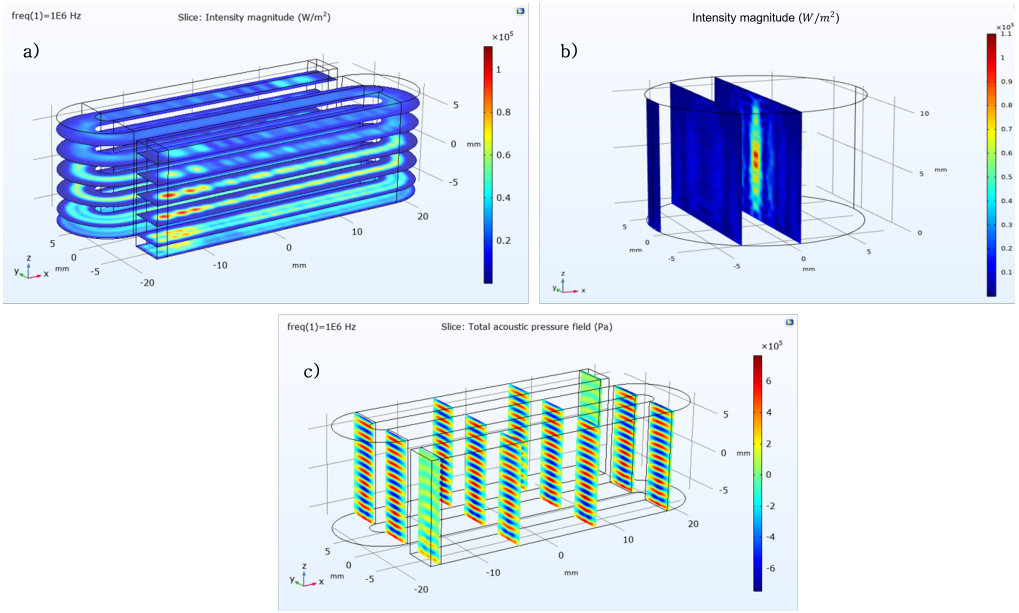

Figure 3.37: Acoustic wave propagation considering a power equal to 80%: a) intensity horizontal planes along the channel, b) intensity vertical planes inside the single well of a 24 well-plate, and c) acoustic pressure vertical planes.

In particular, since for the first printed cartridge no Luminol sonochemiluminescence was detected even at high US intensities during the laboratory experiments, the 80% US power condition is simulated in order to find the possible US power threshold able to provide a sufficient production of ROS. Since the minimum US power allowing for the detection of a blue intensity inside the well corresponds to a power equal to 15%, the 80% US power condition associated to the cartridge is selected since it gives similar intensity and pressure results. However, while the well has a perfectly cylindrical shape, providing also a certain confinement of the ROS production and Luminol reaction, the channel represents a more dispersive system, less confined, characterized by maximum intensity peaks only

close to the inlet and outlet regions and by a lower intensity value on the remaining areas of the channel.

Experimental results

For all its positive aspects, the cartridge with bottom inlet and outlet offers promising results and therefore, it is finally printed through the 3D Digital Light Processing (DLP) method by employing the same material, PEGDA, already used for the first printed cartridge, shown in Figure 3.38. However, a very thin PEGDA cover is added on the top surface of the cartridge in order to prevent and avoid the collapse of the structure during the printing process. Hence, the cartridge in this case is not completely open and the channel has a thin lid separating the solution from the external environment. Nevertheless, the channel always filled up until the 3/4 of its height is reached, due to the formation of trapped air inside the channel both during the filling process and also during the dynamic flow of water.

As previously done, the structural robustness and mechanical resistance of the cartridge is analysed by subjecting it to different sonication powers and time conditions. The structure is able to withstand to all different powers, even up to 100%, and also for various times, as 30 s and also 1 min. For lower power values, such as 15% and 20%, the sonication time is prolonged further to 2 min and 3 min, without affecting the PEGDA structure. However, the thin lid covering the whole structure is found to be the most delicate component since, after some experiments and manipulation, it easily crackles and breaks.

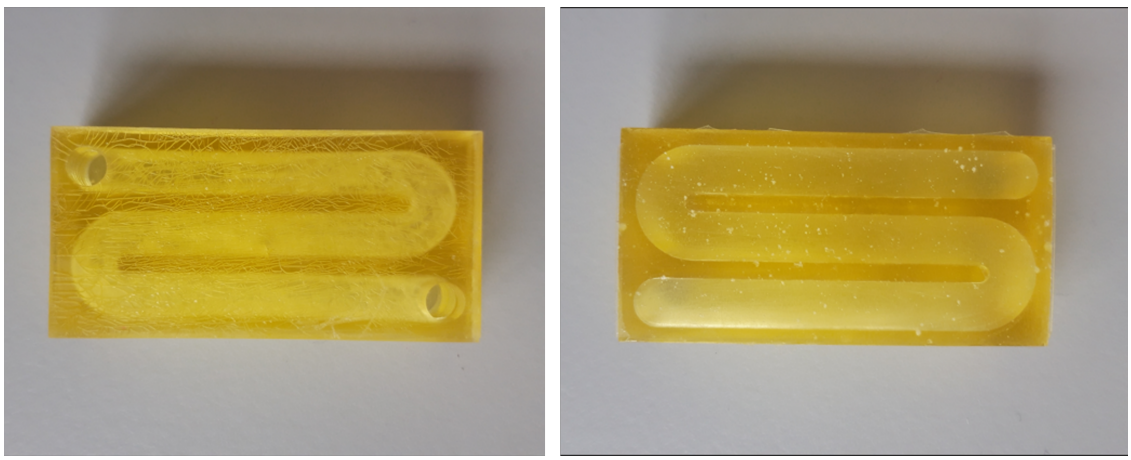

Figure 3.38: View from the cartridge basis (left) and top view (right).

After that, the fluid flow behaviour is analysed by positioning the cartridge over the

transducer head, connecting it to the Therakos® tubes and in turn, to the tubes of the peristaltic pump. Exactly as it is done for the first printed cartridge, double-distilled water is mixed with few drops of ink to emphasize the flow behaviour. With this configuration, thanks to the COMSOL simulations, a more laminar and smooth flow is expected to occur within the channel with respect to the results obtained from the first printed cartridge. However, differently from the previous case, since the maximum flow rate ($Q = 17.47\ mL/min$) seems to generate a too high velocity preventing an effective sonication of the solution, lower values of flow rate are considered, specifically the same used in the simulations in order to allow for a direct comparison.

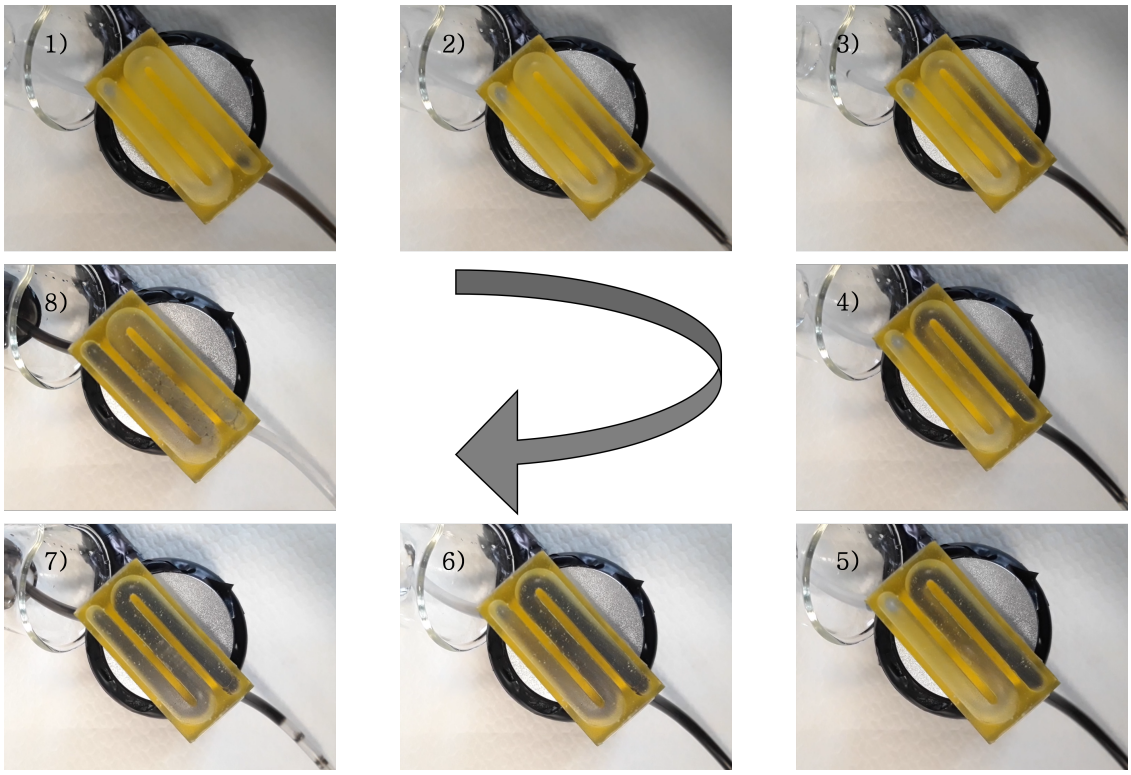

Figure 3.39: Sequence of images acquired during the flow of water and ink in the cartridge with bottom inlet and outlet already filled with water, setting $Q = 12\ mL/min$.

Figure 3.39 presents the time sequence of images acquired during the flow inside the cartridge generated by a $Q = 12\ mL/min$ flow rate. As previously discussed, the new channel configuration provides an efficient smooth and laminar behaviour during the flow of water and ink, effectively minimizing the stagnant areas. This is achieved thanks to the longer longitudinal parts and the semi-circular turns of the channels that are able to guide the fluid during its flow along the serpentine shape. Furthermore, as soon as the ink

enters within the channel, it requires a very short period of time to start propagating along the first longitudinal part of the serpentine: this slight delay may be related to the inlet turbulence found from the simulation results.
Also the fluid flow generated by $Q = 7\ mL/min$ is analysed, resulting in an overall behaviour which is practically the same as the condition using a flow rate equal to $Q = 12\ mL/min$. The only observed difference between the two cases is the decreased velocity associated to the lower flow rate value. Consequently, the time required to complete the serpentine path is longer, approximately equal to 14s for the lower flow rate compared to 11s associated to the higher one.

Finally, also the ability of the cartridge to produce an effective cavitation phenomenon inside the solution in a static condition, responsible for the production of ROS is examined. For this purpose, the Therakos® tubes are interlocked at the inlet and outlet apertures and closed by wrapping their final part with parafilm. The laboratory measurements are carried out with the same procedure already employed: the Luminol solution prepared has unvaried concentrations, the transducer head is positioned inside a box providing the required dark environment, the cartridge is placed upon it with a thin layer of coupling gel and the lens of the digital camera is focused over the top of the cartridge. However, since in this configuration the inlet and outlet are on the bottom part, the positioning of the cartridge over the transducer surface results to be slightly more difficult, but once the proper arrangement is found, the cartridge remains in its position with the majority of the channel area over the transducer surface and thus, exposed to US excitation.

The parameters and quantities set for the experiments are equal to the previous case in order to provide a comparison, since no significant results were obtained for the first printed cartridge. Thus, the US powers whose effects are investigated are the same as before: 15%, 20% and 80% for 30 s, 2 min and 1 min of sonication time, respectively. All the conditions are measured with the cartridge being almost completely filled with the solution, since it is difficult to entirely fill the channel due to air bubbles which remain trapped inside it, as well as only partially filled with the solution.
Unfortunately, as in the previous Luminol experiments with the first printed cartridge, no blue intensity is detected in correspondence of the channel from the acquired images. For this reason, also an exposure to 90% of US power for a time period of 1 min is tested; however, also in this case, no results are obtained.
This behaviour may be explained by the lower US intensity and pressures generated inside the solution with respect to the results obtained with the well, as demonstrated previously from the acoustic wave simulations. Furthermore, it should be noticed that the simulated 80% power value which generated an US intensity similar to the one reached inside the

single well, occurs when the channel is covered by a thin layer of glass, while in the laboratory experiments, the cartridge is already composed of a PEGDA thin lid. From the Table 3.7, it can be highlighted that, in general, the difference between the intensity values corresponding to the condition of the solution exposed to air and the one with the solution covered by glass, is quite large; therefore, the intensity inside the channel associated to the laboratory experiment could be rather lower than the results obtained from the simulation.

Due to the unsuccessful measurements through Luminol sonochemiluminescence, maybe caused by a low US intensity and pressure formed inside the solution, the Electron Paramagnetic Resonance (EPR) Spectroscopy, the same already employed for the ROS generation quantification inside the single well, is exploited.

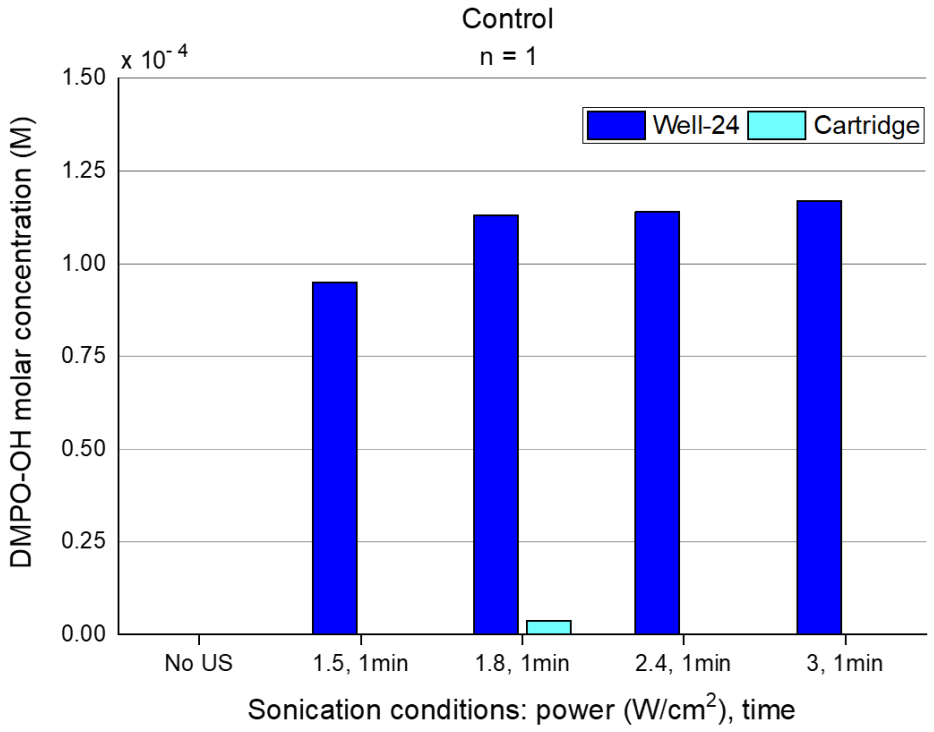

Figure 3.40: EPR results comparing the molar concentration obtained within a single well of a 24-well plate and within the cartridge (without any upper cover, providing the solution to be in direct contact with air.

The solution prepared for these experiments consists on double-distilled water and on the particular spin-trap used for hydroxyl radicals, DMPO, having a concentration of 100 $\mu L/mL$, which is the same used previously for the well. The US powers under test

are 1.5, 1.8, 2.4 and 3 W/cm^2 (corresponding respectively to 50%, 60%, 80% and 100% of the Lipozero maximum achievable power) for a sonication time equal to 1 *min*, as shown in Figure 3.40. The results obtained are presented using the same scale of the single well in order to allow for a direct comparison: the molar concentration of radicals appears to be greatly lower in the cartridge than in the single well, where only the US condition with 60%, 1 *min* gives a detectable concentration, even if it is quite low, around 3.76×10^{-6}. This final examination demonstrates that the cavitation phenomenon occurs only slightly for very high powers condition and in any case, the ROS concentration found is extremely lower than the one generated inside the well. This is the possible reason behind the null blue intensity values when the Luminol sonochemiluminescence is analysed.

3.3.3 Bottom inlet and lateral outlet

CAD project

The last proposed cartridge configuration can be considered as an hybrid design, combining the characteristics of the two previously proposed CAD projects: the inlet aperture is positioned at the bottom of the cartridge, while the outlet is in-plane with the channel (Fig. 3.41).

All its dimensions are the same as in the bottom inlet and outlet cartridge design, reported in Table 3.8, having equal height, length and width of the channel, and thus providing the same volume capacity. These quantities were already chosen for the previous design since they seem to properly meet the printing process, the fluid flow and the sonication requirements.

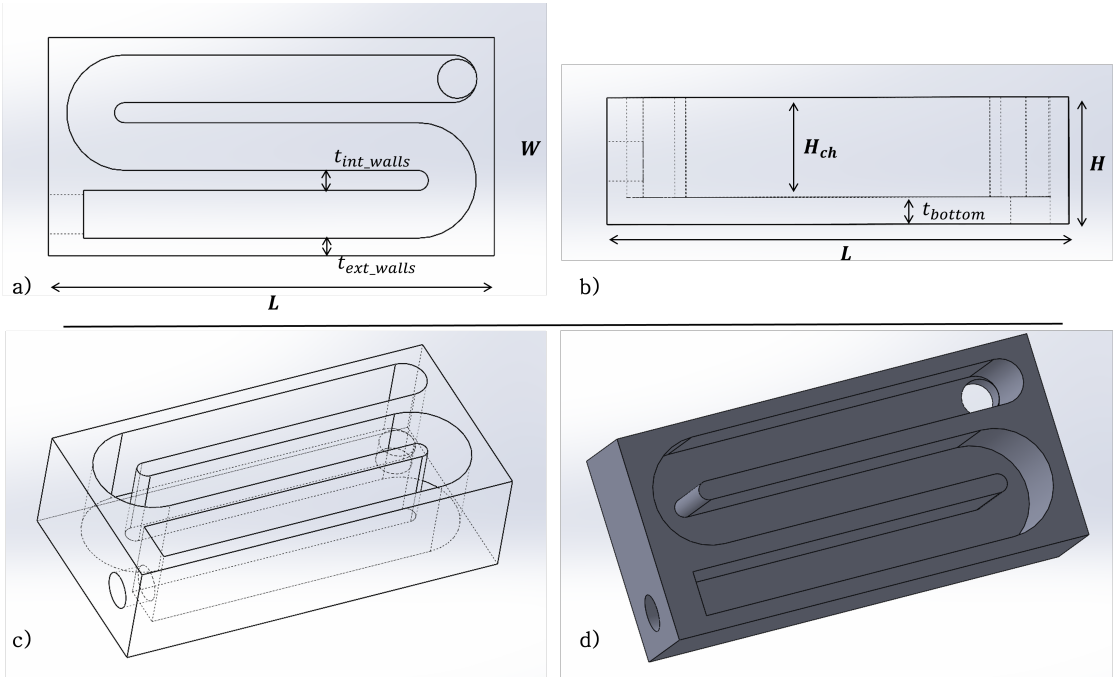

Figure 3.41: CAD project of the third proposed new cartridge: a) top view, b) side view, c) lateral view and d) lateral view of the expected 3D printing process outcome.

COMSOL simulations

Since the channel parameters and dimensions are equal to the previous analysed cartridge design, also the Reynolds number remains the same, $Re = 39.65$.

Parameters	Values	Description
W	25 mm	Width of the cartridge
L	51 mm	Length of the cartridge
H	14 mm	Height of the cartridge
W_{ch}	5.47 mm	Width of the channel
L_{ch}	133.51 mm	Length of the channel
H_{ch}	11 mm	Height of the channel
t_{bottom}	3 mm	Thickness of the of the basis
t_{ext_walls}	2 mm	Thickness of the external walls
t_{int_walls}	2.3 mm	Thickness of the internal walls
Total Volume	8.03 mL	Maximum volume

Table 3.8: Parameters of the third proposed new cartridge project.

Considering that, from this point onward the analysis is carried out following exactly the same discussion and method used in the previous two cartridge designs, the description of this cartridge will be focused more on the results obtained, bypassing the procedure employed.

The CAD project employed in the COMSOL simulations as well as the discretization of the the domain are presented in Figure 3.42.

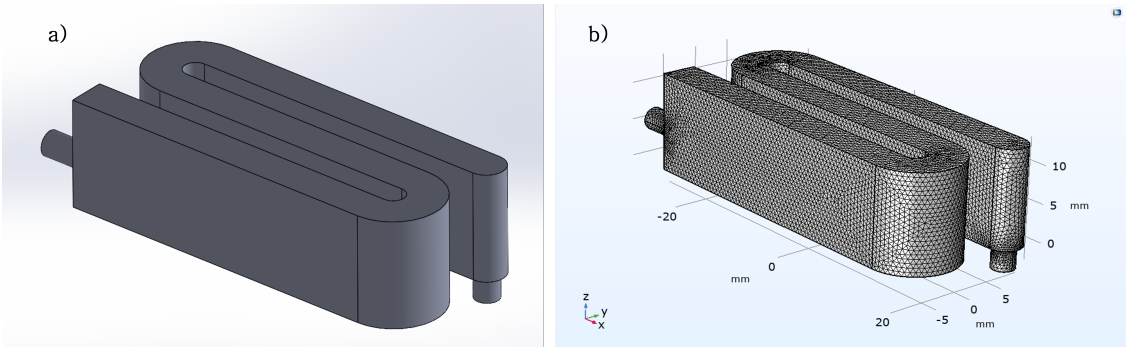

Figure 3.42: a) CAD project for COMSOL simulation representing the implemented domain and b) meshing of the channel CAD design.

Then, the fluid flow simulations regarding the two different conditions of flow rate, $Q = 12\ mL/min$ and $Q = 7\ mL/min$ are discussed:

1. For **Q=12 mL/min**, the velocity magnitude distribution, shown in Figure 3.43, is

characterized by higher values both in correspondence to the inlet aperture, gradually decreasing while moving upwards inside the channel in a vertical direction, and also close to the outlet region, without affecting significantly the channel since the velocity enhancement remains confined in the outlet tube. On the other hand, along the entire length of the serpentine path, the velocity has a lower value emphasized by the shades of blue color, giving an overall average velocity equal to $u_{ave} = 3.87\ mm/s$.

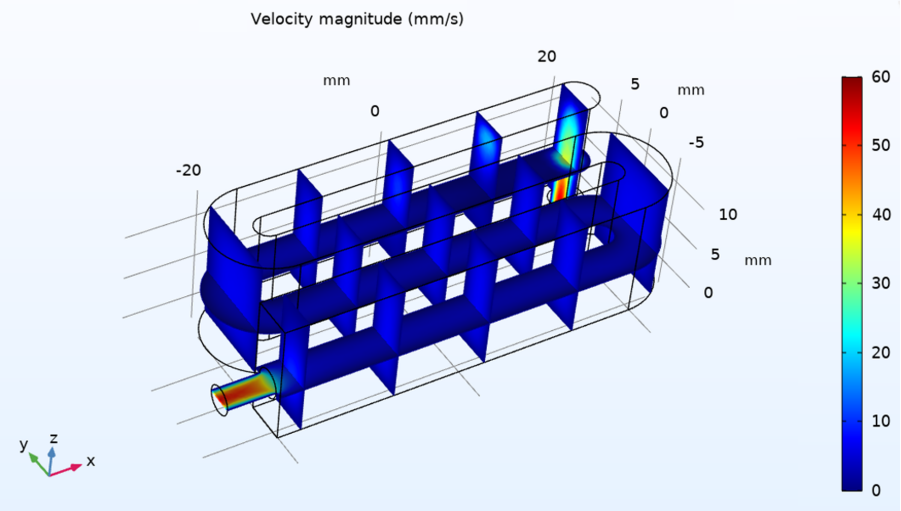

Figure 3.43: Horizontal and vertical planes of the velocity magnitude distribution along the channel: the horizontal plane corresponds to an height equal to $z = 5\ mm$ for $Q = 12\ mL/min$.

However, as also discussed before, the velocity distribution plot is not able to give sufficient information about the behaviour of the velocity vector itself, concerning the possible turbulence of the fluid flow. Therefore, the velocity streamlines are simulated and analysed (Fig. 3.44). As represented in the plot, the streamlines underline the effects of the combination of the two previous cartridge designs: the velocity turbulence at the inlet resembles the behaviour of the "bottom inlet and outlet" cartridge; in fact, as soon as the water enters within the channel and it is pushed upwards due to the constant flow rate setting, it is subjected to a vortex by "falling" downwards. Differently, the velocity trend at the outlet is rather similar to the one of the "lateral inlet and outlet" project, with no significant turbulence.

Finally, the velocity profile (Fig. 3.45) shows a very similar behaviour with respect to the "bottom inlet and outlet" configuration, consisting in a maximum velocity peak on the upper channel area when considering the first vertical cut positioned close to the

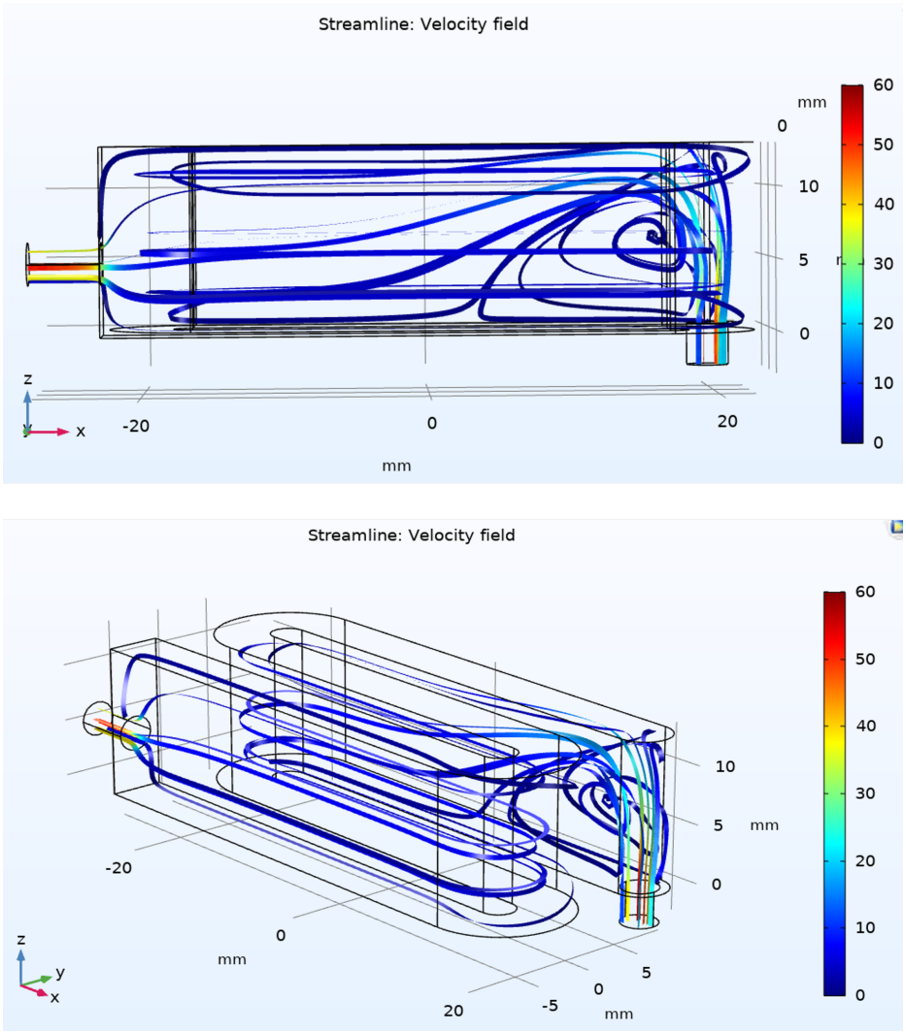

Figure 3.44: Velocity streamlines plot for $Q = 12\ mL/min$.

inlet, while the second peak associated to the downward turbulent region seems to be slightly lower. Then, the velocity continues to decrease until a steady-state condition with a constant velocity profile is reached in correspondence of the 3/4 of the inlet channel.

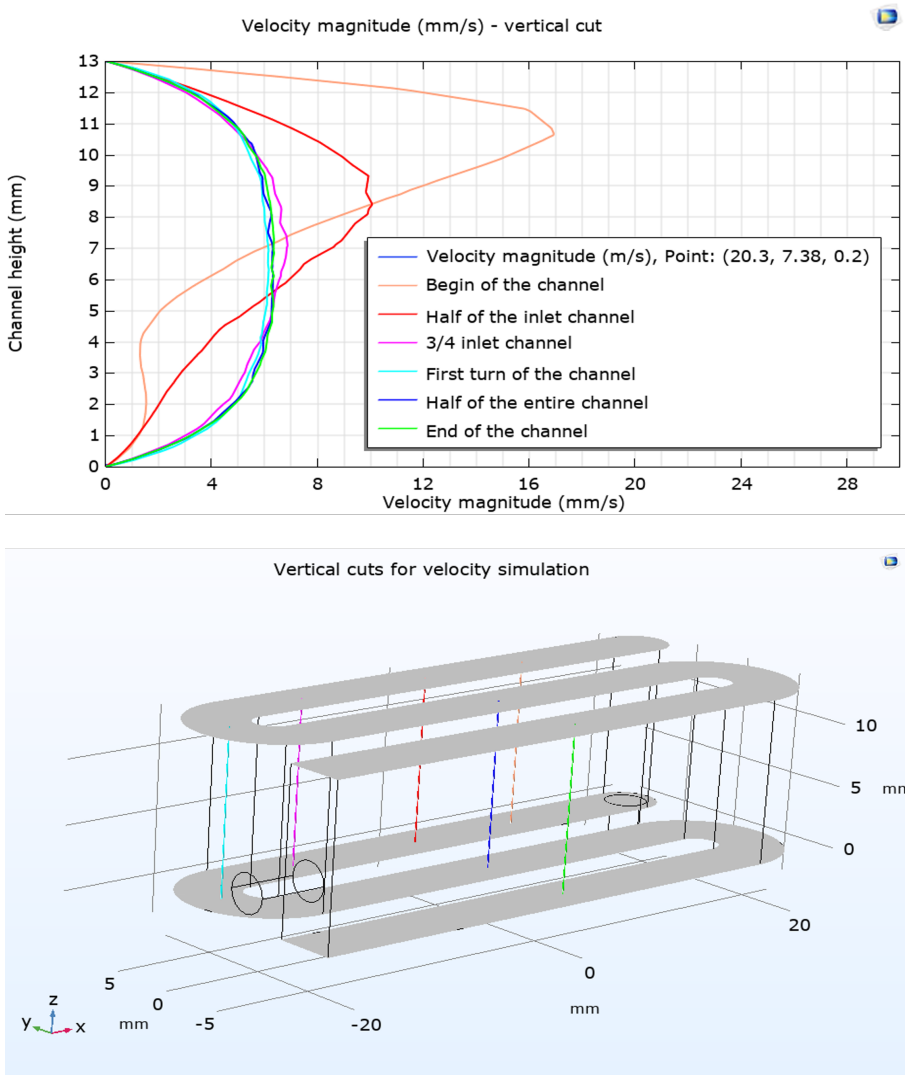

Figure 3.45: Velocity profile (top) and chosen lines cutting vertically the channel (bottom) for $Q = 12\ mL/min$.

2. On the other hand, for the condition with **Q=7 mL/min**, as it happened for the previous cartridge designs, the velocity distribution (Fig. 3.46) shows an overall trend which is the same obtained for $Q = 12\ mL/min$, however with decreased velocity values, highlighted by the green color associated to the inlet and outlet apertures.

   The reduction of the velocity allows to obtain a smaller turbulent region providing, in turn, a shorter development length of the flow at the entrance of the channel, as demonstrated by the streamlines plot, Figure 3.47.

At the end, this behaviour facilitates the formation of the steady-state condition, occurring already at half the length of the inlet channel, as shown in the velocity profile plot (Fig. 3.48).

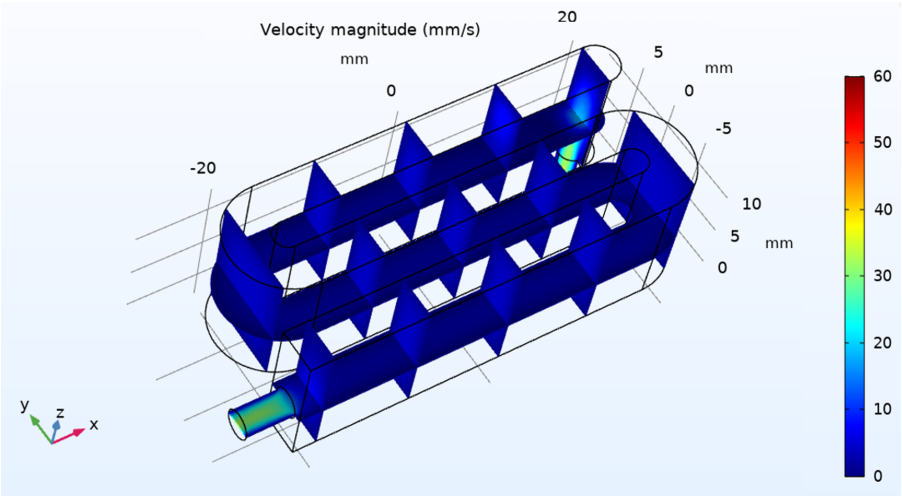

Figure 3.46: Horizontal and vertical planes of the velocity magnitude distribution along the channel: the horizontal plane corresponds to an height equal to $z = 5\ mm$ for $Q = 7\ mL/min$.

Finally, since the channel characteristic dimensions are rather alike to the previous cartridge design, also the mean velocity values as well as the time required by the water to travel the entire serpentine path are approximately the same, presented in Table 3.9. Thanks to these similarities with the "bottom inlet and outlet" configuration, the acoustic wave propagation inside the channel results to be exactly the same and its discussion is referred to the previous section reported in Figure 3.36.

As a consequence, since it shows very promising fluid flow behaviour and it is designed to meet all the printing requirements, also the "bottom inlet and lateral outlet" configuration is printed.

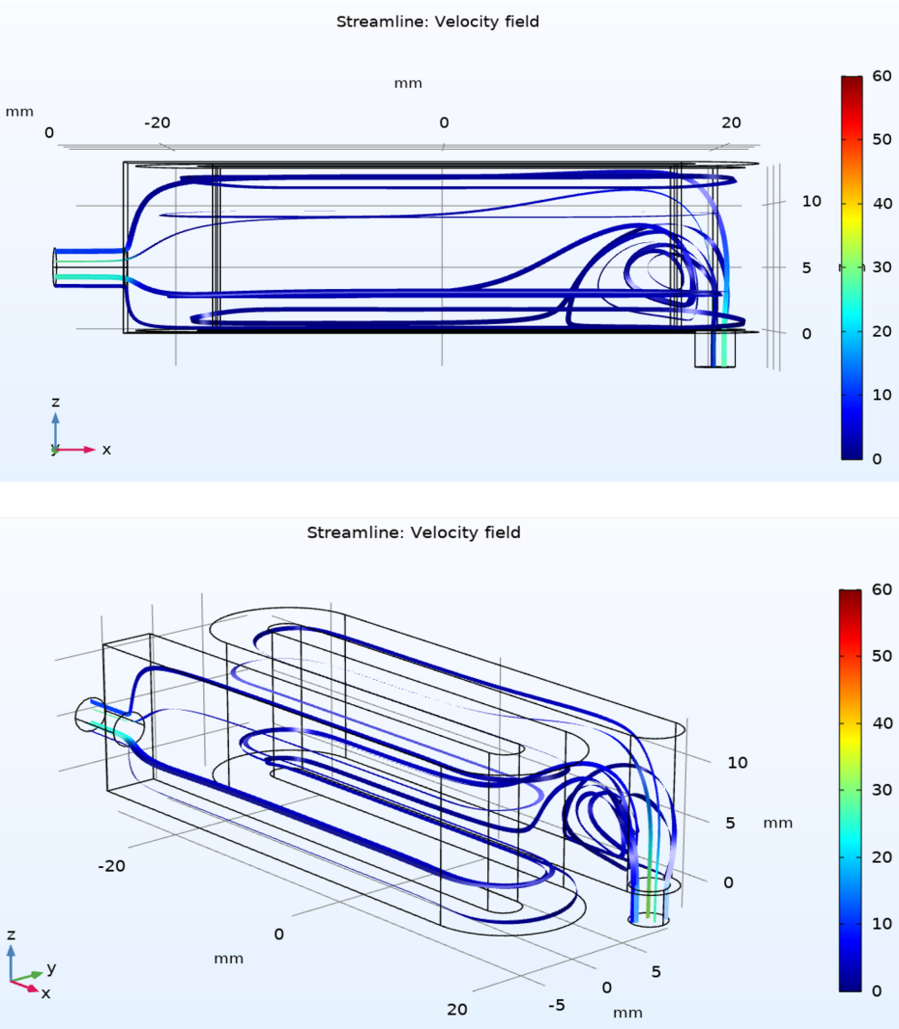

Figure 3.47: Horizontal and vertical planes of the velocity magnitude distribution along the channel: the horizontal plane corresponds to an height equal to $z = 5\ mm$ for $Q = 7\ mL/min$.

Q (mL/min)	**Q (m^3/s)**	**Velocity$_{ave}$ (mm/s)**	**Travel time (s)**
$Q_{max} = 17.47$	$Q = 2.9 \cdot 10^{-7}$	$u_{max} = 5.76$	$t_{min} = 22.73$
$Q = 12$	$Q = 2 \cdot 10^{-7}$	$u = 3.87$	$t = 33.82 \simeq 30$
$Q = 7$	$Q = 1.17 \cdot 10^{-7}$	$u = 2.22$	$t = 58.89 \simeq 60$ (1min)
$Q = 5$	$Q = 8.33 \cdot 10^{-8}$	$u = 1.55$	$t = 84.52 \simeq$ 1min, 25s

Table 3.9: Fluid flow simulations values regarding average velocity and time required to complete the serpentine path for different flow rates Q.

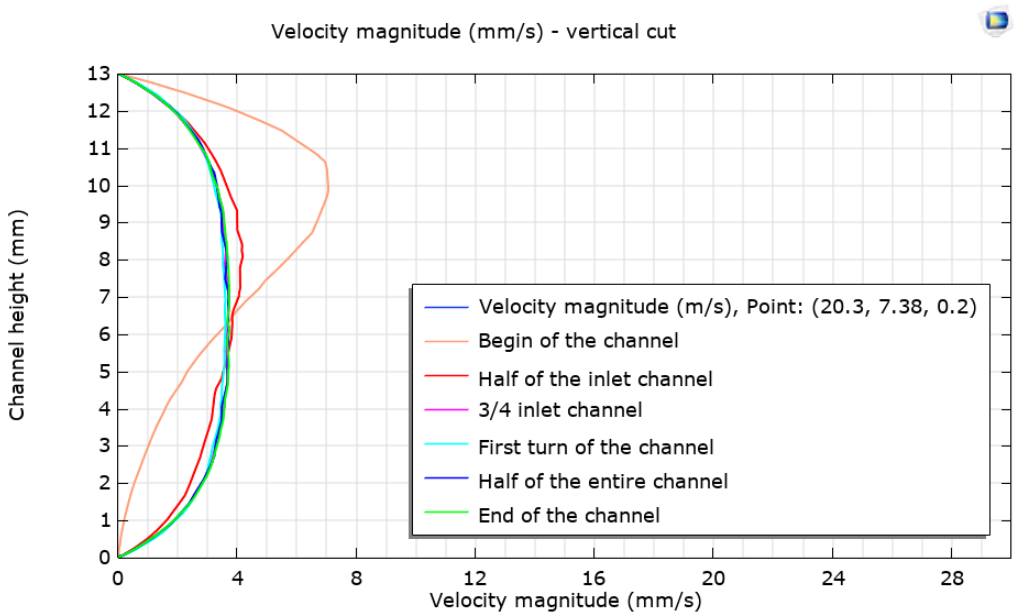

Figure 3.48: Velocity profile for $Q = 7\ mL/min$.

Experimental results

Since this "bottom inlet and lateral outlet" configuration is printed contemporary and with the same DLP technique of the "bottom inlet and outlet" cartridge, the whole set of mechanical resistance tests as well as all the fluid flow experiments and acoustic cavitation measurements are carried out at the same time with equal procedure, characteristics and parameters.

In order to not repeat the same comments already discussed for the previous cartridge, only the most important features and major results are reported in this section.

First of all, to prevent the collapse of the cartridge structure during the printing process, a thin PEGDA lid is added on top, thus realizing a "close cartridge", shown in Figure 3.49. Furthermore, the liquid volume inside the channel can reach, at most, only the 3/4 of the channel height during the fluid flow; in addition, it is also difficult to completely fill it with water in static conditions due to the presence of trapped air inside the channel.

Then, since the cartridge structure is practically the same as the previous one, its robustness and mechanical strength show an effective ability to withstand various US power conditions, such as high powers, even at 100% with sonication times of 30 s, 1 min and low powers, 15% and 20% applied for longer periods of time as 2 min or 3 min. The most

delicate component of the cartridge is surely the very thin lid at the top.

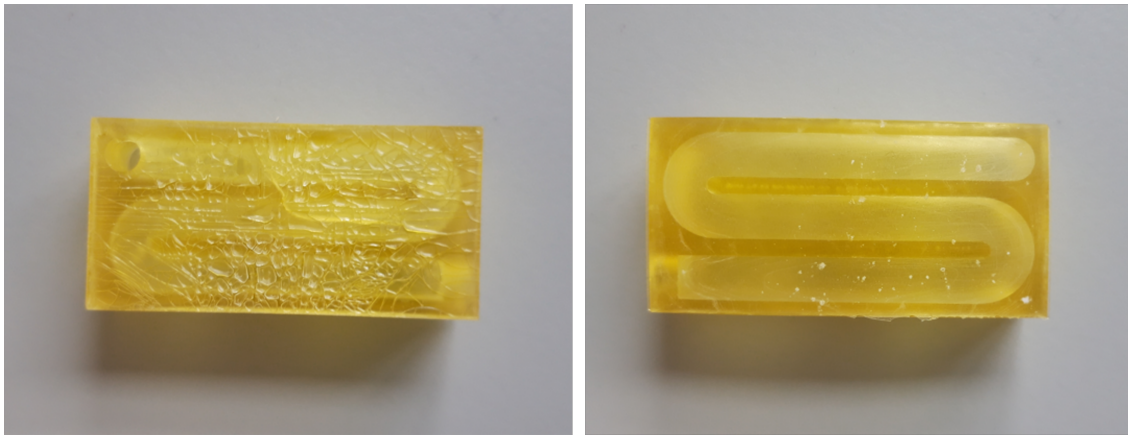

Figure 3.49: View from the cartridge basis (left) and top view (right).

After that, the fluid flow behaviour is analysed by connecting the cartridge to the peristaltic pump, exactly with the same procedure done before. The only difference that happened with these experiments is that a very light crack on top of the channel occurred and thus, a layer of grease is spread over the thin PEGDA lid to avoid any water leakage. Once that the thin crack is sealed with grease, the fluid flow is determined for both the flow rate values. In particular, Figure 3.50 refers to a flow rate equal to $Q = 12\ mL/min$, showing a very similar behaviour to the previous case. The major difference relies on the outlet configuration which is in-plane with respect to the channel: the main issue arising from this condition is that, if the outlet tube is not sufficiently inclined, some drops of water may remain inside it causing the air to be trapped within the exit tube. As a consequence, the water contained in the channel should reach a certain pressure to push the air and water bubbles inside the tube and be able to exit; however, if the pressure is too high, it can damage the thin PEGDA lid on the top of the structure. Thankfully, this phenomenon does not happen if the outlet tube is positioned with the right curvature.
On the other hand, for the value of flow rate equal to $Q = 7\ mL/min$, the water behaviour inside the channel remains the same, but characterized by a slightly lower velocity.

Furthermore, the flow obtained in both cases shows a rather smooth and laminar trend, in accordance with the results expected from the COMSOL simulations and thus, together with the "bottom inlet and outlet" configuration, also this project represents a promising choice for the design of the final sonication chamber.

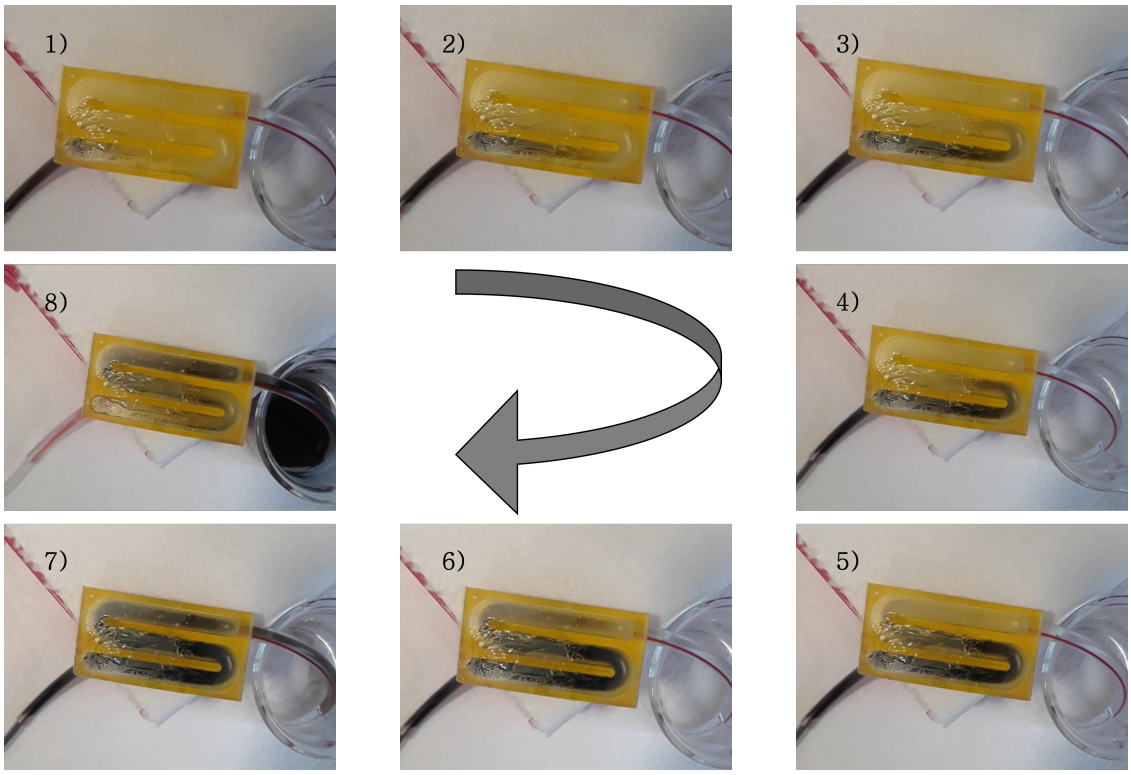

Figure 3.50: Sequence of images acquired during the flow of water and ink in the cartridge with bottom inlet and lateral outlet already filled with water, setting $Q = 12\ mL/min$.

Ultimately, the US cavitation phenomenon occurring inside the solution is measured through the Luminol sonochemiluminescence. However, the results are exactly the same obtained for the previous cartridge, with null blue intensity values in correspondence to the channel shape, that may be compared with the EPR measurements carried out for the "bottom inlet and outlet" cartridge, since they have the same dimensions and characteristics. In this way, the absence of blue intensity is in accordance with the EPR results, which highlights a low production of ROS inside the solution even at high powers.

3.3.4 A different type of cartridge: PLA instead of PEGDA

Different material and structure adjustments

The reason behind the almost null generation of ROS detected through EPR and Luminol SCL measurements on the previous cartridge prototypes could be related to various aspects: a too thick bottom basis that can cause a too large decay of the US wave, thus preventing its transmission to the solution, the PEGDA material itself that can absorb

a non-negligible fraction of US, or also the shape of the channel. In fact, the higher US intensity values together with a non-negligible concentration of ROS were obtained in a single well of a 24-well plate, having a radius much longer than the width of the serpentine channel: this particular design can, actually, impede an effective sonication of the solution.

Therefore some structure modifications and adjustments are made to enhance the ROS production inside the solution. As a first step, the cartridge channel should be enlarged, letting a wider channel area to be directly in contact with the transducer head and increasing the sonicated solution volume. However, the 3D printing technique already employed for the previous cartridge prototypes does not allow for the printing of larger structures in any of the three directions (nor for the height, width and length). For this reason, a different type of printing technique is needed, able to produce wider 3D structures: the previous Digital Light Processing (DLP) method is replaced by the Fused Deposition Modeling (FDM), which works with polymers.

In the FDM 3D printing technique, a thermoplastic filament, rolled up on a spool, is fed into an extrusion assembly, where it is heated to a semi-liquid state [66]. Then, the material is extruded through a metal nozzle which moves following a programmed path and as soon as the filament is deposited, it quickly solidifies before being stacked by another layer. At the end, the resulting 3D plastic structure is obtained through a layer-by-layer deposition technique.

Since the FDM works with various types of plastics, the choice fell on another biocompatible and semi-transparent material to replace the previously employed PEGDA, which is PLA.

CAD project

The CAD project, in Figure 3.51 recalls the same characteristics of the "Bottom inlet and outlet" cartridge design, with the difference that the overall 3D structure is enlarged, allowing to obtain a wider serpentine channel and a larger maximum volume of solution, around 16 mL (Table 3.10).

The final structure results to have a more pronounced squared shape, while its height is maintained equal to the previous project.

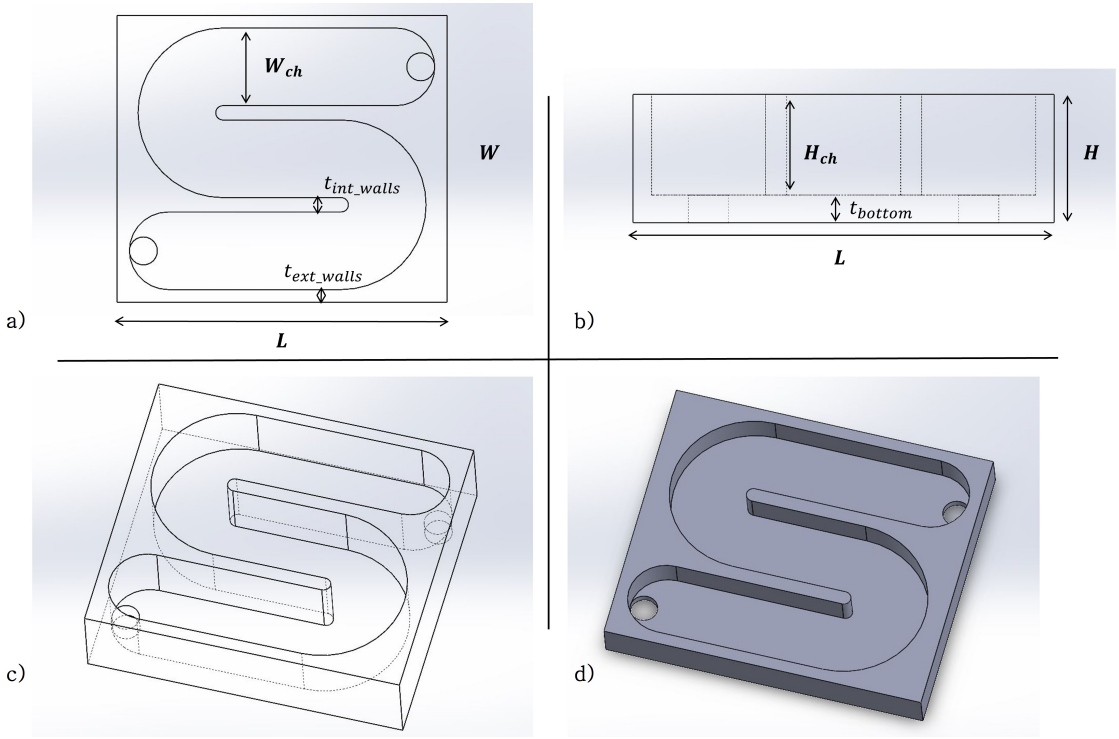

Figure 3.51: CAD project with the adjustments made to the "Bottom inlet and outlet" previous cartridge: a) top view, b) side view, c) lateral view and d) lateral view of the expected 3D printing process outcome.

Parameters	Values	Description
W	46 mm	Width of the cartridge
L	53 mm	Length of the cartridge
H	14 mm	Height of the cartridge
W_{ch}	12.46 mm	Width of the channel
L_{ch}	160.04 mm	Length of the channel
H_{ch}	11 mm	Height of the channel
t_{bottom}	3 mm	Thickness of the of the basis
t_{ext_walls}	2 mm	Thickness of the external walls
t_{int_walls}	2.3 mm	Thickness of the internal walls
Total Volume	15.8 mL	Maximum volume

Table 3.10: Parameters of the new cartridge project.

Experimental measurements of the fluid flow

Since the general behaviour of the fluid flow inside the serpentine-like channel was already known from the COMSOL simulations of the previous cartridge prototypes, in this case

the flow is directly analysed in laboratory experiments, Figure 3.52, by mixing ink and water.
As expected, the flow shows a quite similar behaviour to the previous conditions; however, since the width of the channel is larger, the velocity of the flow is reduced. In fact, the time required to complete the entire serpentine path exceeds 1 min. This flow characteristic is aligned with the need of a sufficiently long permanence time of the solution above the transducer head, thus allowing for an effective sonication.

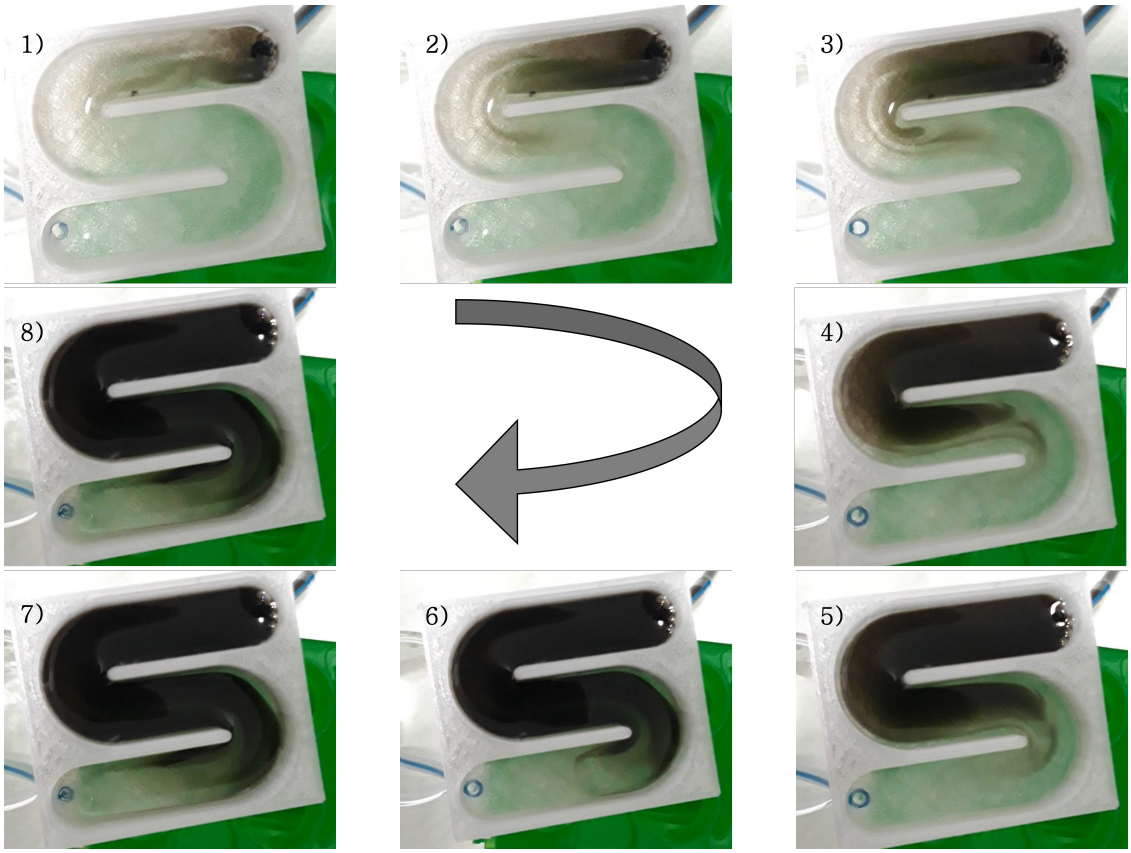

Figure 3.52: Sequence of images acquired during the flow of water and ink in the cartridge with bottom inlet and lateral outlet already filled with water, setting $Q = 12\ mL/min$.

Experimental measurements of the acoustic behaviour

Since the acoustic impedances of the PLA and PEGDA materials have approximately a similar value, 1.6 $MRayl$ and 1.7 $MRayl$ respectively, also the transmission of the US wave to the solution is expected to be almost the same. However, due to the almost null ROS generation obtained with the previous cartridge prototypes, the US behaviour on this PLA

cartridge is directly analysed by means of cells.

3.4 Cells experiments in static conditions

Since the EPR measurements on the previous printed cartridge highlighted an almost null production of ROS inside the solution, also the direct effect of US on cells is analysed, comparing the results obtained for the PLA with the "Bottom inlet and lateral outlet" cartridge prototypes.

The cells considered belong to the Peripheral Blood Mononuclear Cells (PBMC), consisting in peripheral blood cells (cellular components of blood) having a round nucleus, as lymphocytes and monocytes.

As a first step of the experimental procedure, the stock concentration of 1.8×10^6 $cells/mL$ is verified by introducing the cells in the Trypan blue dye. If the cells are alive, their membrane impede the absorption of trypan, so that the cells are not coloured; differently, in dead cells, the damaged membrane let it pass through, colouring the cells.
In a first attempt, the cells and Trypan are mixed in a 1:100 ratio; however, since this concentration turned out to be too diluted and only few cells were visible under the microscope, a ratio of 1:20 is considered. Thus, 10 µL of cells are withdrawn from the stock and introduced in an Eppendorf together with 190 µL of Trypan dye. After that, a small amount of sample is analysed under the microscope. In this case, 28 cells are scored and the following expression gives, actually, the same concentration of the stock:

$$\frac{28\ cells}{3} \cdot 20 \cdot 10 \cdot 10^4 = 1.86 \times 10^6\ cells \tag{3.20}$$

where 3 is the number of squares of the microscope grid, 20 is the Trypan dilution value, 10 is the entire volume and 10^4 is a conversion term from mm^3 to mL.

Then, the concentration of cells to be introduced inside the cartridge prototypes is selected as the same already employed in a single well of a 24-well plate: 1.5×10^6 $cells$ in 2mL. Therefore, the calculations can be resumed as follows:

1. **PLA cartrdige** - Total volume = 10 mL:

$$Number\ of\ cells\ =\ \frac{1.5\ million \cdot 10\ mL}{2\ mL} = 7.5\ million \tag{3.21}$$

$$Volume\ to\ take\ from\ the\ stock\ =\ \frac{7.5\ million \cdot 10^6\ mL}{1.8 million} = 4.2\ mL \tag{3.22}$$

2. **"Bottom inlet and lateral outlet" cartridge** - Total volume = 6 mL:

$$Number\ of\ cells\ =\ \frac{1.5\ million \cdot 6\ mL}{2\ mL} = 4.5\ million \tag{3.23}$$

$$Volume\ to\ take\ from\ the\ stock\ =\ \frac{4.5\ million \cdot 10^6\ mL}{1.8 million} =\ 2.5\ mL \tag{3.24}$$

These two quantities are withdrawn from the stock and inserted in two different Falcon. Then, they are centrifuged at 500 RFC for 10 min to replace the culture medium with a fresh one. Once that the cells are prepared, they are introduced in one cartridge at a time for the US treatment: the cartridge is positioned on the transducer's head, analysing the condition at 10% of US input power ($0.3\ W/cm^2$) and 1 min of sonication time. After the treatment, the cells are collected in a treated culture flask and incubated at $37°C$, 5% of CO_2 for 24h. Finally, an other culture flask is prepared containing the untreated cells, in order to compare the treated cell viability with a control one.
At the end of the experiment procedure, the two cartridge prototypes are cleaned by using hypochlorite and washed with water.

After 24h of incubation, the cells are introduced inside three Falcon, associated to the control, PLA and "Bottom inlet and lateral outlet" cartridges. The associated volumes are checked, obtaining an overall reduction compared to the initial volumes considered:

1. Control: 9.7 mL (vs an initial one of 10 mL)
2. PLA Cartridge: 8.9 mL (vs an initial one of 10 mL)
3. "Bottom inlet and lateral outlet" Cartridge: 5.4 mL (vs an initial one of 6 mL)

The reason behind this decrease can be caused by a partial evaporation as well as by a residual left inside the cartridge during the collection of the treated culture medium.

Then, the cells are scored by introducing them in the trypan dye (Figure 3.53): the living cells are surrounded by a dark color while the cells debris are completely coloured by the dye. The trypan, in this case, is employed with a ratio 1:10, meaning that 10 μL of cells are mixed with 90 μL of trypan inside three Eppendorf. For any case, a small sample volume is analysed under the microscope, giving the results:

1. **Control** - scored number of living cells: 20

$$\frac{20}{3} \cdot 10 \cdot 9.7 \cdot 10^4 = 6.5 \times 10^6\ (6.5\ millions) \tag{3.25}$$

2. **PLA Cartridge** - scored number of living cells: 15
   By using the same expression: $4.45 \times\ 10^6$ ($4.45\ millions$)

3. **"Bottom inlet and lateral outlet Cartridge** - scored number of living cells: 26
   By using the same expression: 4.68×10^6 (4.68 *millions*)

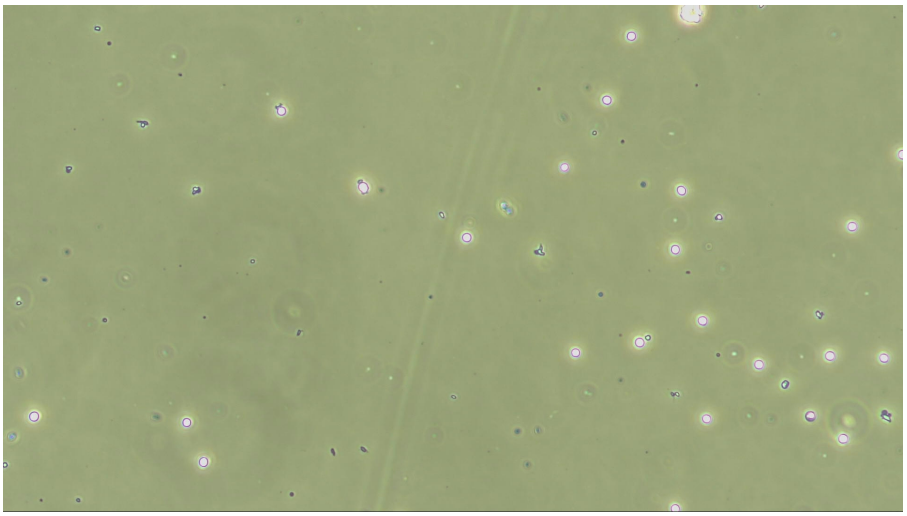

Figure 3.53: Lymphocytes observed under the microscope.

From this first results, it is possible to notice that the PLA cartridge is responsible for an higher fraction of cells death: 4.5 millions of cells found, compared to 6.5 millions cells of the control and 7.5 millions of cells initially introduced. On the other hand, the number of cells of the second cartridge implies that there has been a slight increment of cells: 4.68 millions of cells obtained, compared to 4.5 millions of initial cells. This different behaviour between the two cartridges could be associated to the stronger heating effect of the PLA cartridge during the US treatment than the second cartridge. In fact, when cells are subjected to an heating environment above $38° - 39°C$, they enter in a condition of a mild, followed by a moderate, hyperthermia, responsible for a slight cytotoxic effect.

The same procedure is repeated after 48h and 72h, giving the results in Figure 3.54, where the label "Cartridge - 1" refers to the PLA cartridge and "Cartridge - 2", to the "Bottom inlet and lateral outlet" cartridge.

As discussed previously, it is possible to notice an important decrease of the cell viability for the PLA cartridge after 24h of incubation which increases after 48h and 72h. On the other hand, the cell viability related to the second cartridge is characterized by a significant increase after 24h and then, it tends to decrease for longer incubation time.

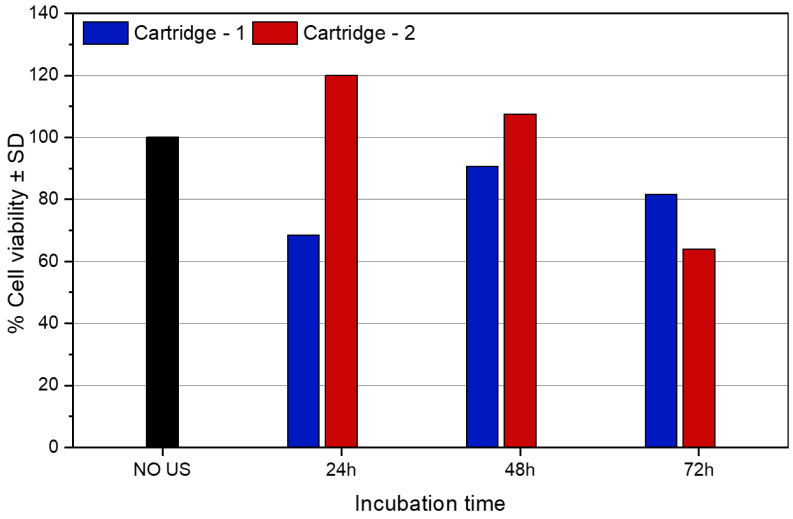

Figure 3.54: Cell viability obtained for the sonication condition: power of 0.3 W/cm^2 and time equal to 1 min.

Chapter 4

Conclusions and future perspectives

The most significant outcomes arising from the two main topics analysed in this Master Thesis, search for the best US sonication condition and design of the cartridge, are further underlined in this Chapter.

The main purpose of the first part relies on the extensive research of the combination of US power and treatment time able to ensure a cytotoxic effect only when used in conjunction with a specific concentration of NPs. In fact, the desired sonication condition and NPs concentration, when employed separately in laboratory measurements, should not be harmful to cells.

As a consequence, the control measurements (without NPs) are carried on to select the combinations of US power and treatment time which do not produce a great damage to KB cells. Since at the 20% of US power, corresponding to 0.6 W/cm^2, the cell viability is greatly affected by the US excitation for any analysed treatment time, this power value shows a too strong harmful behaviour to KB cells. In fact, the 0.6 W/cm^2 of input power corresponds to the cavitation threshold, responsible for an enhanced production of ROS inside the solution, greatly affecting the cells. From the COMSOL simulations, this phenomenon is demonstrated to occur when an acoustic pressure amplitude of 0.311 MPa is propagating inside the central volume of the solution.
On the other hand, the input US power providing the generation of an amount of ROS which is not high enough to damage the KB cells, but that can lead to a cytotoxic effect when used in combination with NPs, is more probable to be 0.45 W/cm^2; however, since this power is below the cavitation threshold, for short treatment times the amount

of produced ROS can be too low, whereas this phenomenon is more probable to happen for longer sonication times, such as 2 or 3 min.
Furthermore, the consistency of the SCL control results with the cell viability demonstrates that the SCL can be a useful and fast method for a qualitative evaluation of ROS production and, therefore, on the effects that ROS can have on living cancer cells.
Since also the US power equal to 10%, 0.3 W/cm^2, does not induce a consistent cells death, both 15% and 10% are further analysed by introducing 10 $\mu g/mL$ of NPs.
Thus, the synergistic action of US excitation and NPs is analysed, comparing the cell viability, SCL and EPR measurements. However, the amount of ROS detected by the EPR equipment is not high enough to generate an effective cytotoxic effect, as the cell viability remains quite high (100%) for any sonication condition, meaning that the majority of cells is still alive. This behaviour is consistent with the SCL measurements, whose average blue intensity is approximately null for any combination of US power and treament time.

Finally, concerning the second part of the dissertation, since the resulting cartridge should meet specific requirements, a careful attention should be paid on its fluidic, acoustic and mechanical properties.

After some preliminary designs, a first cartridge prototype was printed, whose simulations and experimental measurements allowed for an analysis on the channel characteristics and paved the way to improved cartridge projects. The major observations found were numerous: firstly, in order to avoid turbulent or stagnant areas within the channel, whose presence would be detrimental for cells, the channel should provide a laminar flow of the solution. Consequently, a serpentine-like shape was found to be the most suitable for this purpose. Furthermore, unlike the UV-chamber employed in the Therakos® CELLEX® photopheresis system, in this case the height of the channel is not subjected to any limitation thanks to the ability of US to penetrate deeply into tissues, thus avoiding the cells self-shielding problem. Then, in order to obtain an effective sonication of the sample, the cartridge material should allow the transmission of the acoustic wave inside the channel. For this reason, the cartridge was fabricated through a 3D light-based printing technique, known as Digital Light Processing (DLP), by using the material PEGDA. At the end, to avoid the collapse of the structure during the printing procedure as well as to achieve a sufficient final mechanical strength, its lateral and inner walls were thickened, giving to the cartridge the ability to withstand the US excitation, heating and manipulation.

The simulations of the improved cartridge designs highlighted a lower turbulence and a more constant velocity profile behaviour along the entire serpentine path in two configurations: when the inlet hole is positioned through the cartridge bottom basis, and the

outlet is positioned in the lateral wall, and when both the inlet and outlet are placed at the bottom of the structure. Consequently, these two different configurations were printed to analyse their behaviour through laboratory experiments.
For both configurations, the fluid flow resulted to be consistent with the COMSOL simulations, providing a laminar flow with low turbulence through the channel. On the other hand, the time needed for the solution to complete the entire serpentine path is strictly dependent on the flow rate employed, since higher flow rates correspond to shorter travel times. During the experiments, as the effective time was found to be a little shorter than the time resulting from the simulations, the flow rate should be further decreased to provide a sufficient longer time for an effective sonication of the solution.
The main concerns regard the acoustic properties of the PEGDA material, since, from the experimental measurements through EPR, a minimum or null amount of ROS was detected even for high input US powers, compared to the ROS obtained in a single well of a 24-well plate. However, this result reveals a contradiction between the experimental and simulation outcomes. In fact, from the simulations, it was found that the acoustic intensity inside the cartridge, sealed with a thin glass lid and subjected to an 80% input power, reached a value comparable to the acoustic intensity obtained inside a single well of a 24-well plate subjected to a 15% of input power. As this condition inside the well corresponds to the first US power able to produce a detectable amount of ROS, it was expected that also inside the cartridge a sufficient amount of ROS was generated; however, the ROS produced inside the cartridge resulted to be almost null. The possible reasons behind this result could be associated to a too thick bottom basis of the structure that can effectively prevent the transmission of the US excitation to the solution, to the PEGDA material that can absorb a non-negligible fraction of the US wave or also to the particular shape of the channel. In fact, the higher values of US intensity distribution were reached inside the single well of a 24-well plate, characterized by a concentric pattern, as demonstrated by the COMSOL simulations: the serpentine channel having a width smaller than the single well radius can impede an effective sonication.

To improve ROS production inside the cartridge, other biocompatible and transparent materials could be considered. An example is PLA, whose 3D-printing method allows to obtain larger structures, allowing to enlarge the serpentine-like channel. As a larger fraction of solution would be sonicated, the production of ROS could be enhanced. At the same time, if the channel width is enlarged, the time required for the solution to complete the whole serpentine path increases, thus it supports the need of a longer travel time for an effective sonication of the solution. An other possibility is to reduce further the thickness of the bottom basis to ensure a lower absorption of US waves.

In conclusion, this Master Thesis work behaves as a connection between the preliminary study of the whole project and the first applications involving cancer cells. In fact, once that the cartridge material and design are established, the following step of the research would be the analysis of cells viability in a static condition, analysing the behaviour of cells when introduced inside the sonication chamber and treated with US; these experiments would pave the way for the dynamic measurements, performed by treating directly the blood while it is flowing inside the serpentine channel of the cartridge.

Acknowledgements

I would like to thank everyone who supported and helped me for the realization of this project. In particular, my gratitude goes to my supervisor, Prof. Valentina Cauda, for introducing me to a topic that I found really interesting and the possibility to work with her research group. I'm grateful also to all the members of the TNH Lab, for their advices and time spent to help me to perform the experiments (Marco, Veronica, Luisa, Marzia, Giada, Nicolò, Federica, Rocio, Maria Cristina) as well as also to all the DISAT team. I would like to thank my thesis colleague and friend Michele for the support given to me even after his graduation.
I'm deeply grateful to all my friends and my family, who always supported and encouraged me, both during good times but also during tough ones. Thank you.

Bibliography

[1] H. Sung et al. "Global Cancer Statistics 2020." In: *CA Cancer J Clin.* 71(3):209-249 (2021).

[2] *World Health Organization.* URL: https://www.who.int/health-topics/cancer#tab=tab_1.

[3] D. A. Corley et al. "Cancer Screening During the Coronavirus Disease-2019 Pandemic." In: *The National Cancer Institute's PROSPR Consortium.* (2020).

[4] H. Dillekås et al. "Are 90% of deaths from cancer caused by metastases?" In: *Cancer medicine.* 8(12): 5574–5576 (2019).

[5] S. Valastyan and R. Weinberg. "Tumor Metastasis: Molecular Insights and Evolving Paradigms." In: *Cell.* 147(2), 275–292 (2011).

[6] R. Anderson et al. "A framework for the development of effective anti-metastatic agents." In: *Nature Reviews Clinical Oncology.* 16(3):185-204 (2018).

[7] A. Kowalik et al. "Current approaches for avoiding the limitations of circulating tumor cells detection methods—implications for diagnosis and treatment of patients with solid tumors." In: *Translational Research.* 185, 58–84.e15 (2017).

[8] I. J. Fidler et al. "Cancer biology is the foundation for therapy." In: *Cancer Biology & Therapy.* 4(9), 1036–1039 (2005).

[9] B. Psaila and D. Lyden. "The metastatic niche: adapting the foreign soil." In: *Nature Reviews Cancer.* 9(4), 285–293 (2009).

[10] A. Chambers et al. "Dissemination and growth of cancer cells in metastatic sites." In: *Nature Reviews Cancer.* 2(8), 563–572 (2002).

[11] I. J. Fidler. "The pathogenesis of cancer metastasis: the "seed and soil" hypothesis revisited." In: *Nature Reviews Cancer.* 3(6), 453–458 (2003).

[12] Y. Hüsemann et al. "Systemic Spread Is an Early Step in Breast Cancer." In: *Cancer Cell.* 13(1), 58–68 (2008).

[13] Z. Zhang and M. R. King. "Nanomaterials for the Capture and Therapeutic Targeting of Circulating Tumor Cells." In: *Cellular and Molecular Bioengineering.* 10(4), 275–294 (2017).

[14] J. H. Myung et al. "Dendrimer-Mediated Multivalent Binding for the Enhanced Capture of Tumor Cells." In: *Angewandte Chemie International Edition.* 50(49), 11769–11772 (2011).

[15] E. Lianidou and D. Hoon. "Circulating Tumor Cells and Circulating Tumor DNA." In: *Principles and Applications of Molecular Diagnostics.* 9:235–281 (2018).

[16] E. I. Galanzha et al. "In vivo magnetic enrichment and multiplex photoacoustic detection of circulating tumour cells." In: *Nature Nanotechnology.* 4(12), 855–860 (2009).

[17] E. I. Galanzha et al. "In vivo, Noninvasive, Label-Free Detection and Eradication of Circulating Metastatic Melanoma Cells Using Two-Color Photoacoustic Flow Cytometry with a Diode Laser." In: *Cancer research.* 69(20):7926-34 (2009).

[18] H. J. Lee et al. "Simultaneous capture and in situ analysis of circulating tumor cells using multiple hybrid nanoparticles." In: *Biosensors and bioelectronics.* 47:508-14 (2013).

[19] B. P. Viraka Nellore et al. "Aptamer-Conjugated Graphene Oxide Membranes for Highly Efficient Capture and Accurate Identification of Multiple Types of Circulating Tumor Cells." In: *Bioconjugate Chemistry.* 26(2), 235–242 (2015).

[20] G. Calixto et al. "Nanotechnology-Based Drug Delivery Systems for Photodynamic Therapy of Cancer: A Review." In: *Molecules.* 21(3), 342 (2016).

[21] J. M. Dąbrowski. "Inorganic Reaction Mechanisms Volume 70 || Reactive Oxygen Species in Photodynamic Therapy: Mechanisms of Their Generation and Potentiation." In: *Advances in Inorganic Chemistry.* 70:343–394 (2017).

[22] P. A. Vieyra-Garcia and P. Wolf. "Extracorporeal Photopheresis: A Case of Immunotherapy Ahead of Its Time." In: *Transfusion Medicine and Hemotherapy.* 47(3), 226–235 (2020).

[23] R. Edelson et al. "Treatment of Cutaneous T-Cell Lymphoma by Extracorporeal Photochemotherapy." In: *New England Journal of Medicine.* 316(6), 297–303 (1987).

[24] A. C. da Silva Almeida et al. "The mutational landscape of cutaneous T cell lymphoma and Sézary syndrome." In: *Nature Genetics.* 47(12):1465-70 (2015).

[25] E. K. Yoo et al. "Apoptosis Induction by Ultraviolet Light and Photochemotherapy in Cutaneous T-cell Lymphoma: Relevance to Mechanism of Therapeutic Action." In: *The journal of investigative dermatology.* 107(2):235-42 (1996).

[26] R. Knobler et al. "Guidelines on the use of extracorporeal photopheresis." In: *Journal of the European Academy of Dermatology and Venereology.* 28 Suppl 1(Suppl 1):1-37 (2014).

[27] D. E. Heck et al. "Production of hydrogen peroxide by cutaneous T-cell lymphoma following photopheresis with psoralens and ultraviolet light." In: *Cancer Chemotherapy and Pharmacology.* 28(5), 344–350 (1991).

[28] F. Lansigan and F. M. Foss. "Current and Emerging Treatment Strategies for Cutaneous T-cell Lymphoma." In: *Drugs.* 70(3), 273–286 (2010).

[29] THERAKOS®CELLEX®Photopheresis System. "An integrated, closed photopheresis system designed for a strategic immune response." In: *Therakos, Inc.* (2018).

[30] S. Liang et al. "Recent Advances in Nanomaterial-Assisted Combinational Sonodynamic Cancer Therapy." In: *Advanced Materials.* 32(47), 2003214 (2020).

[31] G. Canavese et al. "Nanoparticle-assisted ultrasound: A special focus on sonodynamic therapy against cancer." In: *Chemical Engineering Journal.* 340, 155-172 (2018).

[32] *Part 3 - Reflection and Transmission of ultrasonic waves.* URL: http://www.fast.u-psud.fr/~martin/acoustique/support/r%5C%C3%5C%A9flection-r%5C%C3%5C%A9fraction.pdf.

[33] N. Vyas et al. "Which Parameters Affect Biofilm Removal with Acoustic Cavitation? A Review." In: *Ultrasound in Medicine & Biology.* 45(5):1044-1055 (2019).

[34] Y. T. Didenko et al. "Molecular emission from single-bubble sonoluminescence." In: *Nature.* 407, 877–879 (2000).

[35] V. MIŠÍK and P. RIESZ. "Free Radical Intermediates in Sonodynamic Therapy." In: *Annals of the New York Academy of Sciences.* 899(1), 335–348 (2006).

[36] G. Bisht and S. Rayamajhi. "ZnO Nanoparticles: A Promising Anticancer Agent." In: *Nanobiomedicine.* 3, 9 (2016).

[37] E. Ho. "Zinc deficiency, DNA damage and cancer risk." In: *The Journal of Nutritional Biochemistry.* 15(10), 572-578 (2004).

[38] P. P. Fu et al. "Mechanisms of nanotoxicity: Generation of reactive oxygen species." In: *Journal of Food and Drug Analysis.* 22(1), 64–75 (2014).

[39] R. S. Hotchkiss et al. "Cell Death." In: *New England Journal of Medicine.* 361(16), 1570–1583 (2009).

[40] G. Wan et al. "Recent advances of sonodynamic therapy in cancer treatment." In: *Cancer Biology & Medicine.* 13(3), 325–338 (2016).

[41] H. Montaseri et al. "Review: Organic nanoparticle based active targeting for photodynamic therapy treatment of breast cancer cells." In: *Oncotarget.* 11(22):2120-2136 (2020).

[42] N. Garino et al. "A Microwave-Assisted Synthesis of Zinc Oxide Nanocrystals Finely Tuned for Biological Applications." In: *Nanomaterials.* 9(2), 212. (2019).

[43] N. Garino et al. "Zinc oxide nanocrystals as a nanoantibiotic and osteoinductive agent." In: *RSC Advances.* 9(20), 11312–11321. (2019).

[44] V. Vighetto et al. "The Synergistic Effect of Nanocrystals Combined With Ultrasound in the Generation of Reactive Oxygen Species for Biomedical Applications." In: *Frontiers in Bioengineering and Biotechnology.* 7:374 (2019).

[45] T. J. Tiong et al. "Comparison of sonochemiluminescence images using image analysis techniques and identification of acoustic pressure fields via simulation." In: *Ultrasonics Sonochemistry.* 36, 78–87 (2017).

[46] L. Yue and Y. Liu. "Mechanistic Insight into pH-Dependent Luminol Chemiluminescence in Aqueous Solution." In: *The Journal of Physical Chemistry B.* 124, 35, 7682–7693 (2020).

[47] H. N. McMurray and B. P. Wilson. "Mechanistic and Spatial Study of Ultrasonically Induced Luminol Chemiluminescence." In: *The Journal of Physical Chemistry A.* 103(20), 3955–3962 (1999).

[48] Michael J. Davies. "Detection and characterisation of radicals using electron paramagnetic resonance (EPR) spin trapping and related methods." In: *Methods.* 109:21-30 (2016).

[49] C. L. Hawkins and M. J. Davies. "Detection and characterisation of radicals in biological materials using EPR methodology." In: *Biochimica et Biophysica Acta (BBA) - General Subjects.* 1840(2), 708–721 (2014).

[50] R. T. Weber. "EMX User's manual." In: *Bruker Instruments, Inc.* (1998).

[51] Keisuke M. et al. "A mini review: Fundamental aspects of spin trapping with DMPO." In: 37(5-6), 657–665 (1991).

[52] J. P. Klare. *Spin Trapping: EPR Line Patterns from Hyperfine Interactions.* URL: https://www.researchgate.net/post/Why-we-are-getting-pattern-1221-for-DMPO-hydroxy-radical-in-electron-spin-resonance-Reason.

[53] *EPR SOFTWARE, Xenon Software.* URL: https://www.bruker.com/pt/products-and-solutions/mr/epr-instruments/epr-software/xenon.html.

[54] L. Racca et al. "Zinc Oxide Nanocrystals and High-Energy Shock Waves: A New Synergy for the Treatment of Cancer Cells." In: *Frontiers in Bioengineering and Biotechnology.* 8:577 (2020).

[55] COMSOL. "Acoustics Module User's Guide." In: *Scientific Reports.* (2018).

[56] L. Spigarelli et al. "Numerical study of the effect of channel aspect ratio on particle focusing in acoustophoretic devices." In: *Scientific Reports.* 10, 19447 (2020).

[57] N. A. H. Hadi et al. "Modelling pressure distribution in sonicated ethanol solution using COMSOL simulation." In: *E3S Web of Conferences.* 90, 02003 (2019).

[58] Z. Wei and L. K. Weavers. "Combining COMSOL Modeling with Acoustic Pressure Maps to Design Sono-reactors." In: *Ultrasonics Sonochemistry.* 31:490-498 (2016).

[59] K. H. Lee et al. "Irradiation chamber for photoactivation patient treatment system." In: *United States Patent.* 4,737,140 (1988).

[60] S. Gara. "Irradiation chamber." In: *United States Patent Application Pubblication.* US 2004/0143208A1 (2004).

[61] S. Acharya. "Analysis and FEM Simulation of Flow of Fluids in Pipes, Fluid Flow COMSOL Analysis." In: *Yrkeshögskolan Arcada.* (2016).

[62] "CFD Module User's guide." In: *COMSOL* (2018).

[63] G. González et al. "Materials Testing for the Development of Biocompatible Devices through Vat-Polymerization 3D Printing." In: *Nanomaterials.* 10(9), 1788 (2020).

[64] H. Kadry et al. "Digital light processing (DLP) 3D-printing technology and photoreactive polymers in fabrication of modified-release tablets." In: *European Journal of Pharmaceutical Sciences.* 135, 60–67 (2019).

[65] A. Urrios et al. "3D-PRINTING OF TRANSPARENT BIO-MICROFLUIDIC DEVICES IN PEG-DA." In: *Lab Chip.* 16, 2287-2294 (2016).

[66] R. Singh S. Singh and M.S.J. Hashmi. "Implant Materials and Their Processing Technologies." In: *Reference Module in Materials Science and Materials Engineering.* (2016).